THE UNIVERSITY *of* EDINBURGH

Investigation of the Interactions between Fluorescent Base Analogues and the Natural DNA Bases

Kyle Paterson

Submitted in total fulfilment of the requirements of the degree of Doctor of Philosophy

The University of Edinburgh

2020

Produced on archival quality paper

Abstract

DNA and RNA are integral to all life on Earth, and yet their physical properties and behaviour in their native environment are still only imperfectly understood. Using fluorescent analogues of natural DNA bases (FBAs) as a probe of local inter-base interactions is a widely employed solution-phase technique to obtain information about DNA conformation and its response to enzyme activity. Work presented in this thesis aims to show that free FBAs in solution with the natural DNA bases is a useful model of the inter-base interactions of FBAs in oligonucleotides, and that the effect of substituting DNA bases with fluorescent analogues on DNA conformation can be predicted computationally. Some results from fluorescence spectroscopy to gain further insights into the effect of conformation on electronic energy transfer will also be discussed.

2-aminopurine (2AP) is a responsive fluorescent base analogue that is widely used as a probe of the local molecular environment in DNA. However, the mechanism of this inter-base quenching remains imperfectly understood. Two previous studies of collisional quenching of 2AP by the natural nucleotides presented conflicting results. A comprehensive investigation of inter-base quenching of 2AP by the natural bases in solution is presented here, reproducing the buffer conditions used in the previous studies. Time-resolved fluorescence measurements are used to provide insight into both dynamic and static quenching, showing consistent trends across both buffer systems, and the results support a charge transfer mechanism. Time-resolved fluorescence data also provide evidence for formation of 2AP-nucleotide ground-state complexes in solution, the fluorescence lifetimes of which are comparable to that seen in 2AP-containing oligonucleotides.

Collisional quenching studies were extended to a recently reported FBA, pentacyclic adenine (pA), which has red-shifted emission relative to 2AP, as well as increased brightness. However, rapid photobleaching of pA makes it difficult to use steady-state fluorescence measurements to calculate quenching efficiencies; in consequence time-resolved fluorescence data was obtained to quantify the effect of the natural monophosphate nucleotides on the fluorescence of pA. It was found that collisional interaction of pA with the purine bases increased its fluorescence lifetime (the inverse of a quenching effect), while interaction with the pyrimidine bases

shortened the lifetime. These observations were consistent with previous studies of the effect of the base sequence surrounding pA in oligonucleotides. The results of these collisional quenching experiments for 2AP and pA show that measuring the fluorescence of free FBAs in solution in the presence of the natural bases is a valid technique for predicting the behaviour of FBAs in oligonucleotide strands.

In order to complement the spectroscopic studies, computational techniques were employed to examine the structural impact of substituting a natural base with a base analogue in oligonucleotide sequences. Geometry optimisations of dinucleotides containing pA were carried out, using the DFT functional M06-2X, which accounts for dispersion, to model the effect of this novel FBA on inter-base stacking in DNA. DNA base-step and backbone structural parameters were extracted from the optimised structures and used to show that the substituted dinucleotides adopt conformations similar to that associated with B-form DNA.

Previous studies have shown that, in 2AP-containing dinucleotides, electronic energy transfer occurs from the natural base to 2AP, on excitation of the natural base at 260 nm. It was found that there was a substantial increase in energy transfer efficiency in frozen solution at 77 K compared to room temperature. In the present study, the energy transfer process was investigated as a function of temperature over the range 5-25 °C, to examine the effect of reducing temperature while maintaining fluid conditions. A trend of decreasing quenching efficiency with increasing temperature was found, which is consistent with the previous findings. The results of this work also show that energy transfer is conformationally selective over this temperature range, as can be inferred from decay parameters obtained using time-resolved fluorescence measurements.

In summary, this thesis yields deeper understanding of the effect of interactions with natural DNA bases on the photophysics of two FBAs, pA and 2AP, and presents a method for predicting the behaviour of novel FBAs without *a priori* preparing substituted dinucleotides.

Lay Summary

Life as we know it is dependent on several types of molecule, such as DNA, which will be the focus of this thesis. Despite the structure of DNA being discovered more than half a century ago, scientists are still actively studying the properties of DNA and new discoveries being made on a regular basis. At the most basic level, DNA consists of DNA bases (adenine, guanine, thymine and cytosine), the letters representing all genetic information in the order in which they are grouped together, and a backbone connecting the DNA bases comprised of deoxyriboside sugars linked together by phosphate groups. Many of the assumptions about the way in which DNA interacts with other biological molecules, including proteins, enzymes and RNA, are regularly challenged, and the effect these other molecules have on DNA is often poorly understood. The idea that DNA acts merely as a passive store of genetic information to be read out in the form of green eyes or black hair is now widely discredited. Of course, DNA does perform this function, but it is commonly accepted that information does not just flow in one direction. A whole host of molecules form complexes with DNA (and sometimes each other simultaneously) to carry out functions such as protein/enzyme production, DNA repair, DNA replication, modifications of DNA bases to 'silence' or 'enhance' expression of specific genes.

There are a variety of techniques used to study DNA, but the method utilised for the majority of this thesis is fluorescence spectroscopy. Fluorescence is the process where UV or visible light is absorbed by a molecule as electronic energy, and subsequently emitted again as UV or visible light, albeit usually at a different wavelength and colour due to losses as heat energy. Fluorescence has the advantage that it is compatible with molecules dissolved in water, which is the natural environment of most biological molecules, including DNA. Although definitive structural information cannot be obtained *via* fluorescence measurements, it is highly sensitive to its environment and can therefore be used to highlight changes in the local environment of a fluorescent molecule. Unfortunately, DNA bases are non-fluorescent, which is useful to limit harmful mutations and cancer, but makes fluorescence spectroscopy very difficult. For this reason, analogues of DNA bases such as 2-aminopurine (2AP) and pentacyclic adenine (pA) are used to overcome this problem. In the absence of any natural DNA bases, both these fluorescent analogues

have a relatively high fluorescence emission intensity. However, when 2AP or pA starts interacting with nearby natural DNA bases, the electronic energy gained when 2AP or pA absorbs light can be converted to another form of energy (besides light) more easily due to the interaction with the natural DNA base. This electronic energy can only be 'spent' in one way, whether that is fluorescence or another process that doesn't emit light. For this reason, adding another non-fluorescent process for the extra electronic energy competes with fluorescence and reduces the emission intensity or shortens the lifetime of the higher energy state. This can be measured and used as an indicator of the proximity of DNA bases to 2AP or pA. Where either 2AP or pA, separately, is in solution with a natural DNA base, fluorescence measurements presented in this thesis showed that changes in fluorescence emission increased as the concentration of natural DNA base increased.

It is also possible for electronic energy to be passed from one molecule to another, even if the first molecule is not fluorescent, like the natural DNA bases. This can be seen in energy transfer from a natural DNA base to 2AP. Transfers of electronic energy such as this require certain conditions to be satisfied before they take place. First, the donor molecule must have sufficient energy to closely match the energy the acceptor molecule would normally absorb directly from incident light. Second, the donor and acceptor molecules must have the right relative orientation and should be fairly close to each other. These criteria mean that using a light source with a wavelength that is only absorbed by natural DNA bases and measuring the fluorescence emission of 2AP will yield information about the relative positions of 2AP and any adjacent natural bases in a DNA structure. Measurements of energy transfer using fluorescence measurements of 2AP-containing dinucleotides showed a decrease in energy transfer as temperature increased, suggesting that DNA conformations less favourable to energy transfer become more important at higher temperatures.

Finally, all of the above is of limited use if substituting adenine with 2AP or pA in DNA results in a highly distorted structure that is in no way representative of natural DNA. It has been shown previously using both theoretical and experimental studies that 2AP has only minimal effects on DNA structure. Here, theoretical calculations are used to demonstrate the same is generally true for pA, depending on the identity of the adjacent natural bases.

I hereby declare the work presented in this thesis is my own work unless otherwise stated and indicated with a reference.

Work from Chapter 4 is published in the paper entitled "Dynamic and static quenching of 2-aminopurine fluorescence by the natural DNA nucleotides in solution" (K. A. Paterson, J. Arlt and A. C. Jones, *Methods Appl. Fluoresc.*, 2020, **8,** 025002, DOI: 10.1088/2050-6120/ab71c3).

No part of this thesis has been submitted for any other degree or professional qualification.

Acknowledgements

Without the support and advice of many people, I would not have made it to this point, and it is here that I intend to express my gratitude.

First, I should give my thanks to Professor Anita Jones, who not only gave me the opportunity to pursue this PhD project, but also consistently provided mentorship throughout the last few years. This was invaluable while navigating the tumultuous and initially perplexing results documented in these pages. I could not have asked for a more supportive and experienced supervisor.

I also need to thank Dr. Jochen Arlt, who inducted me into the arcane fields of femtosecond mode-locked lasers and non-linear optics. His support during the replacement of the pump laser, and subsequent replacement of the replacement, was critical to the success of my research, as were the many hours of his time selfishly monopolised to help link issues with the optical setup to specific components. I hope that nightmares of hearing a knock on his office door at any hour of the day have faded with time.

It would be inappropriate to not mention the support of fellow travellers on the PhD journey. From the start, Rachel Fisher helped me to navigate the day-to-day reality of PhD life and reminders of the benefits of collaboration and cooperation in a group of people carrying out similar work. Critical advice and support was provided by Grant McKenzie at times to successfully optimise the optical setup of the lasers in COSMIC, particularly when setting up the third harmonic in the harmonic generator. I should also thank Alif Sussardi and Ahmad Alsaleh for their companionship throughout my PhD, as well as Sergio Adan Bermudez for reminding me of the importance of a good work-life balance (sometimes by borrowing crucial pieces of optical equipment at inconvenient times). Their friendship was much appreciated.

Finally, but very importantly, I should thank family members, especially my mother, Susan, stepfather, Sean, and brother, Shayne, who provided encouragement and support throughout. I would not even have found this opportunity, or been able to take advantage of it, without their advice and encouragement to look further afield.

Contents

Chapter 1 Introduction

1.1 Thesis purpose and context

The behaviour of DNA in its native environment continues to be a thriving avenue of research, with implications for traditional areas of study such as cancer research,[1, 2] as well as more novel, proof-of-concept applications such as computing[3] and data storage.[4] A variety of methods have been employed to determine the structure of DNA, in particular X-ray diffraction has classically been used to obtain crystal structures of many different DNA sequences with atomic precision. Other solid-state techniques are used, such as electron microscopy and atomic force microscopy, which are capable of similar precision to X-ray diffraction, but are still limited by the fact that biological processes take place in the solution phase. A suitable solution phase technique capable of giving structural information is NMR, but this has severe problems with sensitivity, requiring very high concentrations, although some ways to increase the sensitivity have been developed.[5] It is also a technique which produces an average over the ensemble of conformations that may exist within a particular sample, due to the slow relaxation of excited nuclear spins. Molecular motion typically occurs on the order of picoseconds to nanoseconds, depending on the molecule's size, which is far faster than the timescale of nuclear spin precession.

Another commonly used method, which will be the focus of this thesis, is the use of fluorescence spectroscopy. Like NMR spectroscopy, fluorescence spectroscopy is typically done in the solution phase, although solid state measurements are also possible. In contrast to NMR, fluorescence emission is highly sensitive with concentrations on the order of 10^{-6} M typically used. This high degree of sensitivity can even be extended to measurements of single molecules, using molecules of sufficient brightness. Fluorescence simply involves the absorption of light energy by a molecule, entering an excited electronic state, before returning to the ground state with the emission of light. It is what happens in the excited state that forms the majority of the content of this thesis. The observed fluorescence emission for a given fluorescent molecule (fluorophore) is often highly sensitive to aspects of its local environment, which forms the basis for the use of fluorophores as fluorescent probes for specific properties of their environment. This is often used for the detection of

various chemical species, from metal ions and protons to neutral molecules such as sugars.[6-9]

In the context of DNA, there is a further factor to consider. DNA bases all absorb light at 260 nm, but due to very efficient non-radiative decay mechanisms, have extremely low fluorescence emission intensity. For this reason, fluorescent dyes are added to DNA strands in order for meaningful data from fluorescence spectroscopy to be obtained. This takes place in two main ways, intercalation of fluorescent dyes into the major or minor grooves of solvated DNA, known as extrinsic probes, or the substitution of a natural DNA base with a fluorescent analogue of that DNA base. These are known as semi-intrinsic probes, due to their inclusion within the DNA structure itself, and will form the focus of the work within this thesis. Examples of such probes include 2-aminopurine (2AP),[10] pyrrolocytosine,[11, 12] pentacyclic adenine (pA),[13, 14] 6MI/3MI,[15-19] 6MAP/DMAP,[19-23] and the azauridines,[24-28] among many others.[29, 30] The field of using fluorescent base analogues in DNA is a well-established one, with a large body of work produced since the first report on 2AP by Ward *et al*[31] in 1969. In many ways, 2AP can be considered the classical fluorescent base analogue (FBA), as well as the first reported example of an FBA. For an ideal fluorescent base analogue, two key requirements are that incorporation of the analogue into a strand of DNA must not perturb the natural DNA structure, and the analogue should have sufficient fluorescence emission intensity, certainly more than the natural bases. Furthermore, if the analogue is to function as a probe of DNA conformation, which will be assumed in this thesis, the emission output should be modulated in a detectable and quantifiable way in the presence of natural DNA bases.

It has already been mentioned that 2AP has many desirable properties for a fluorescent base analogue, including those already specified such as not significantly perturbing the natural structure of DNA. However, 2AP has some disadvantages, with short excitation/emission wavelengths in the UV region, hindering its use in fluorescence microscopy techniques. Despite having a relatively high quantum yield (0.68 in water), it also has insufficient fluorescence brightness for single molecule fluorescence, a growing field of study. These drawbacks are one reason for the large body of published work concerning alternative fluorescent base analogues alluded to earlier, as well as the considerable amount of ongoing work.

All of the FBAs mentioned previously were originally conceived to address some of the shortcomings of one or more existing FBAs. Given that the search continues for FBAs with improved properties or tailored to specific applications, whether two-photon absorption, single molecule fluorescence or microscopy, an easier way than DNA incorporation to initially test the photophysical behaviour of novel FBAs is needed. The purpose of this thesis is to examine whether solution phase fluorescence measurements of a free FBA and natural bases in solution can provide a reasonable approximation of the fluorescence behaviour of the same FBA incorporated into DNA. A similar process will be used for 2AP, which is an extremely well-studied system, and pA, which was discovered much more recently and consequently is less well-known. Theoretical calculations will also be used to estimate the degree of perturbation caused by incorporation of pA into dinucleotides, as a model for DNA. In addition, the effect of temperature on energy transfer between the natural bases and 2AP in dinucleotides will be examined, which is highly dependent on the relative positioning and orientation of the adjacent base and analogue. As a consequence, some insight into the effect of temperature, *via* changes in conformation and dynamics, on excited state processes of 2AP in dinucleotides may be gained.

1.2 Structure of thesis

The content of this thesis will be presented as described in this section. In Chapter 2, the theoretical background of work detailed in later chapters will be discussed. This will include sections on DNA structure, theoretical structural calculations (particularly DFT), and the principles of fluorescence. Although a general background will be provided, the focus will be on aspects most relevant to work described in subsequent chapters. Further information specific to a given chapter will be set out in that chapter.

Details of experimental techniques employed will be shown in Chapter 3, along with the general methods, applicable throughout this thesis, used to convert the data obtained into the results presented in later chapters. Experimental conditions unique to each chapter will be presented concisely in the relevant chapter.

Chapters 4-7 will form the results chapters where the work undertaken during this PhD is presented and discussed. Chapter 4 and Chapter 6 will look at the fluorescence emission of free 2AP and pA riboside (pAr), respectively, in aqueous

solution with the natural DNA bases. Comparisons are made between the effect of free DNA bases on the fluorescence emission of the relevant FBA and previously reported fluorescence emission of the same FBA incorporated into dinucleotides or oligonucleotides. For both 2AP and pAr, insights into the interactions between the excited state FBA and the natural bases are gained.

Chapter 5 concerns the transfer of electronic energy from natural bases to 2AP in 2AP-containing dinucleotides. The efficiency of this process is calculated for a range of temperatures from 5 to 25 °C, the trend of which is considered to infer key features of the effect of temperature on the interactions between the natural bases and 2AP in the excited state.

Chapter 7 describes the extension of a previously reported computational method[32] to pA-containing dinucleotides. Optimised structures from DFT calculations are compared to 'ideal' DNA structure by structural parameters quantifying the relative orientation of adjacent bases and dihedral angles in the sugar-phosphate backbone.

This thesis will be brought to a close in Chapter 8 by a summary of the findings presented in the main results chapters. Some thoughts on possible directions of future study will also be included in this chapter.

1.3 References

1. A. Torgovnick and B. Schumacher, *Frontiers in Genetics*, 2015, **6**.
2. M. O. Turgeon, N. J. S. Perry and G. Poulogiannis, *Frontiers in oncology*, 2018, **8**, 15-15.
3. A. Eshra, S. Shah, T. Song and J. Reif, *IEEE Transactions on Nanotechnology*, 2019, **18**, 252-259.
4. S. L. Shipman, J. Nivala, J. D. Macklis and G. M. Church, *Nature*, 2017, **547**, 345.
5. S. J. Meier, P.R.; Karlsson, M.; Lerche, M.H., *Sensors*, 2014, **14**, 1576-1597.
6. N. V. Marinova, N. I. Georgiev and V. B. Bojinov, *Journal of Photochemistry and Photobiology A: Chemistry*, 2013, **254**, 54-61.
7. A. P. de Silva, H. Q. N. Gunaratne, J.-L. Habib-Jiwan, C. P. McCoy, T. E. Rice and J.-P. Soumillion, *Angewandte Chemie International Edition in English*, 1995, **34**, 1728-1731.
8. H. He, M. A. Mortellaro, M. J. P. Leiner, S. T. Young, R. J. Fraatz and J. K. Tusa, *Analytical Chemistry*, 2003, **75**, 549-555.
9. X. Wu, Z. Li, X.-X. Chen, J. S. Fossey, T. D. James and Y.-B. Jiang, *Chemical Society Reviews*, 2013, **42**, 8032-8048.
10. A. C. Jones and R. K. Neely, *Q Rev Biophys*, 2015, **48**, 244-279.
11. K. C. Thompson and N. Miyake, *The Journal of Physical Chemistry B*, 2005, **109**, 6012-6019.
12. Q. L. Nguyen, V. A. Spata and S. Matsika, *Physical Chemistry Chemical Physics*, 2016, **18**, 20189-20198.
13. M. Bood, A. F. Fuchtbauer, M. S. Wranne, J. J. Ro, S. Sarangamath, A. H. El-Sagheer, D. L. M. Rupert, R. S. Fisher, S. W. Magennis, A. C. Jones, F. Hook, T. Brown, B. H. Kim, A. Dahlen, L. M. Wilhelmsson and M. Grøtli, *Chemical Science*, 2018, **9**, 3494-3502.
14. R. S. Fisher, D. Nobis, A. F. Füchtbauer, M. Bood, M. Grøtli, L. M. Wilhelmsson, A. C. Jones and S. W. Magennis, *Physical Chemistry Chemical Physics*, 2018, **20**, 28487-28498.
15. K. Wojtuszewski Poulin, A. V. Smirnov, M. E. Hawkins, F. M. Balis and J. R. Knutson, *Biochemistry*, 2009, **48**, 8861-8868.
16. A. M. Moser, M. Patel, H. Yoo, F. M. Balis and M. E. Hawkins, *Analytical Biochemistry*, 2000, **281**, 216-222.
17. S. L. Driscoll, M. E. Hawkins, F. M. Balis, W. Pfleiderer and W. R. Laws, *Biophysical Journal*, 1997, **73**, 3277-3286.
18. M. E. Hawkins, W. Pfleiderer, F. M. Balis, D. Porter and J. R. Knutson, *Analytical Biochemistry*, 1997, **244**, 86-95.
19. M. E. Hawkins, *Cell Biochem Biophys*, 2001, **34**, 257-281.
20. M. E. Hawkins, W. Pfleiderer, O. Jungmann and F. M. Balis, *Anal Biochem*, 2001, **298**, 231-240.
21. K. E. Augustyn, K. Wojtuszewski, M. E. Hawkins, J. R. Knutson and I. Mukerji, *Biochemistry*, 2006, **45**, 5039-5047.

22. K. Yang, S. Matsika and R. J. Stanley, *The Journal of Physical Chemistry B*, 2007, **111**, 10615-10625.

23. M. Narayanan, G. Kodali, Y. Xing, M. E. Hawkins and R. J. Stanley, *The Journal of Physical Chemistry B*, 2010, **114**, 5953-5963.

24. S. G. Srivatsan and Y. Tor, *Tetrahedron*, 2007, **63**, 3601-3607.

25. R. W. Sinkeldam, N. J. Greco and Y. Tor, *ChemBioChem*, 2008, **9**, 706-709.

26. T. Kobayashi, H. Kuramochi, T. Suzuki and T. Ichimura, *Physical Chemistry Chemical Physics*, 2010, **12**, 5140-5148.

27. R. W. Sinkeldam, P. A. Hopkins and Y. Tor, *ChemPhysChem*, 2012, **13**, 3350-3356.

28. P. A. Hopkins, R. W. Sinkeldam and Y. Tor, *Org Lett*, 2014, **16**, 5290-5293.

29. M. Wilhelmsson and Y. Tor, *Fluorescent analogs of biomolecular building blocks : design and applications*, Hoboken, NJ : Wiley, Hoboken, NJ, 2016.

30. R. W. Sinkeldam, N. J. Greco and Y. Tor, *Chem Rev*, 2010, **110**, 2579-2619.

31. D. C. Ward, E. Reich and L. Stryer, *Journal of Biological Chemistry*, 1969, **244**, 1228-1237.

32. D. A. Smith, L. F. Holroyd, T. van Mourik and A. C. Jones, *Phys Chem Chem Phys*, 2016, **18**, 14691-14700.

Chapter 2 Theory

The work presented in this thesis relies on a number of theoretical principles, which will be outlined in this chapter. Experimental data were obtained using electronic spectroscopy, while theoretical work was performed with structural calculations on short DNA strands using DFT functionals. A basic knowledge of DNA structure is also necessary for the reader to get the most benefit from this thesis. Much of the discussion in this chapter is based on material from Principles of Fluorescence Spectroscopy (J. R. Lakowicz),[1] Introduction to Molecular Spectroscopy (G. M. Barrow),[2] Photochemistry and Spectroscopy (J. P. Simons),[3] Modern Spectroscopy (J. M. Hollas),[4] and Photophysics of Aromatic Molecules (J. B. Birks).[5]

2.1 Electronic Spectroscopy

Spectroscopy is the study of the interaction of electromagnetic radiation with matter. Electromagnetic radiation consists of oscillating electric and magnetic fields at right angles to each other, and to their common direction of travel. These oscillating fields have a frequency and wavelength which can be used to predict how the radiation will behave under given conditions. Since electromagnetic radiation travels at a constant speed *c* (the speed of light, 3×10^8 m s^{-1}), wavelength **λ** and frequency **ν** are inversely proportional (equation 2.1), and either can be used as the defining property of a particular beam of monochromatic light. Energy transmitted *via* electromagnetic radiation is quantised, delivering fixed quantities of energy in virtual particles or photons. The energy of each photon is proportional to the frequency, shown in equation 2.2, where *h* is Planck's constant (6.636×10^{-34} kg m^2 s^{-1}).

$$\nu = \frac{c}{\lambda} \qquad 2.1$$

$$E = h \cdot \nu \qquad 2.2$$

From equation 2.2, the difference in energy between two electronic states (on the order of 10^{-17} J) typically corresponds to frequencies in the UV-visible part of the spectrum. Electronic spectroscopy therefore involves measurement of the interaction of light in the UV-visible part of the electromagnetic spectrum, which stretches from a wavelength of 10 nm at the far end of the UV spectrum to around 700 nm at the interface between visible and near-infrared light. However, most UV light at

wavelengths shorter than 200 nm is strongly absorbed by atmospheric gases (or almost anything else, in fact), therefore this is often referred to as vacuum UV and is not typically used in electronic spectroscopy. In this work, any results presented will be based on measurements using light within the range 200-700 nm. Spectroscopic measurements in this wavelength range are often used to obtain information about the electronic state of the molecule and the local molecular environment, a concept which will form the basis of this thesis.

2.1.1 Absorption

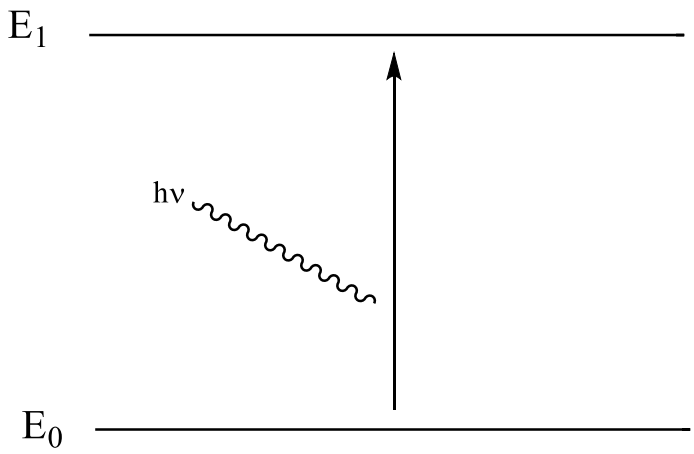

Figure 2.1: Absorption of a photon (hν).

Interaction of electromagnetic radiation with a given wavelength incident on an atom or molecule can result in the transition to a higher electronic state. The oscillating electric field of the incident light imparts a force on an electron in the absorbing molecule, which results in a charge separation defined by a vector quantity, the transition dipole moment μ. In this process electronic energy equivalent to one photon *hv* at the wavelength of the incident radiation is absorbed by the molecule, illustrated in Figure 2.1, exciting the molecule from the ground state E_0 to a higher electronic state E_1. The transition dipole moment μ is related to the integral of the time-independent wavefunctions ψ of the initial and final state, and the dipole moment operator $\hat{\mu}$ in equation 2.3.[3]

$$\mu_{01} = \int_{-\infty}^{\infty} \psi_1^* \hat{\mu} \psi_0 d\tau \qquad 2.3$$

Where $d\tau$ indicates the integral is over all space. From the Born-Oppenheimer approximation, the integral can be split into separate electronic and nuclear integrals

with the appropriate electronic and nuclear wavefunctions. The electronic part can further be split into spatial and spin integrals to give equation 2.4, assuming no interaction between electronic spin and spatial wavefunctions (such as spin-orbit coupling), which is the basis of the selection rules that determine whether electronic transitions can occur.

$$\mu_{01} = \int_{-\infty}^{\infty} \psi_{e,1}^{*} \hat{\mu}_e \psi_{e,0} d\tau \int_{-\infty}^{\infty} \psi_{s,1}^{*} \psi_{s,0} d\tau \int_{-\infty}^{\infty} \psi_{n,1}^{*} \psi_{n,0} d\tau \qquad 2.4$$

Where the subscripts *e*, *s*, *n* refer to the electronic spatial distribution, spin and nuclear parts of the integral, respectively. Since the square of the magnitude of the transition dipole moment indicates the strength of the interaction between the electrons and the incident radiation, a value of zero implies the transition is forbidden. From this, it is obvious that each of the integrals above must be non-zero for an electronic transition to occur, which leads to three selection rules for electronic transitions in atoms and linear or diatomic molecules that must be obeyed for the transition to occur. However, it must be borne in mind that this relies on the assumptions made earlier holding.

For polyatomic molecules, whether a transition is allowed or forbidden depends on the symmetry of the molecule. From the Born interpretation, where the electronic transition $R_e = \int_{-\infty}^{\infty} \psi_{e,1}^{*} \hat{\mu}_e \psi_{e,0} d\tau$, the electronic transition probability (in other words, the transition intensity) is proportional to $|R_e|^2$. The electronic transition moment R_e can be expressed as separate x, y, and z components, such that the transition intensity $|R_e|^2$ is equal to the sum of squares of the x, y and z components of the transition moment. Since the transition dipole moment has the symmetry of a translation in the direction of the corresponding axis for each component, the product of the symmetry of the two electronic wavefunctions and translation along the corresponding axis has to be the same as the totally symmetric species of the molecule's point group. For a closed shell molecule, given that two symmetric species must have the same symmetry if their product is totally symmetric, the symmetry selection rule can be simplified so that the symmetry of the lower state wavefunction must be equal to (or contain, in the case of non-degenerate states) the symmetry of translation along the x-, y- or z-axis. This logic can also be applied to vibronic transitions described by the third integral in equation 2.4 earlier. In non-linear

polyatomic molecules, degradation of quantum numbers proceeds to the extent that only the total electronic spin remains. Therefore the spin selection rule states that transitions involving a change in multiplicity are forbidden. However, molecules that contain an atom with a heavy nucleus can overcome this barrier, due to spin-orbit coupling.

At room temperature, these transitions usually occur from the lowest energy vibrational state within the electronic ground state (E_0) to any appropriate vibrational energy level within the higher energy electronic state (E_1). The absorption of a photon prompts a vertical transition to E_1, a phrase which can be better understood from the transitions shown in Figure 2.2, where the upward transition occurs to a point on vibrational level v' = 2 in the higher energy state (the Frank-Condon state) with the same nuclear coordinates. In other words, the transition is instantaneous and occurs without any change in the structure of the molecule; this is known as the Frank-Condon (FC) principle. Alternatively, this can be rationalised in terms of the Born-Oppenheimer (BO) approximation, which states that electronic and nuclear motion can be considered separately due to the nucleus being heavier and slower than electrons. Therefore, electronic transitions occur much faster than nuclear motion.

The prevalence of a specific transition from one vibrational level in the ground state to another in the excited state is determined by the Frank-Condon factor, which is the vibrational overlap integral at the same nuclear coordinates. This is shown graphically in Figure 2.2, where a larger transition dipole moment for a given vertical transition increases the probability of that transition. For example, the transition from v'' = 0 in the ground state E_0 to v' = 2 in the excited state E_1 (the 0-2 transition) occurs between peaks of the wavefunctions of the initial and final states, giving this transition a high probability of occurring.

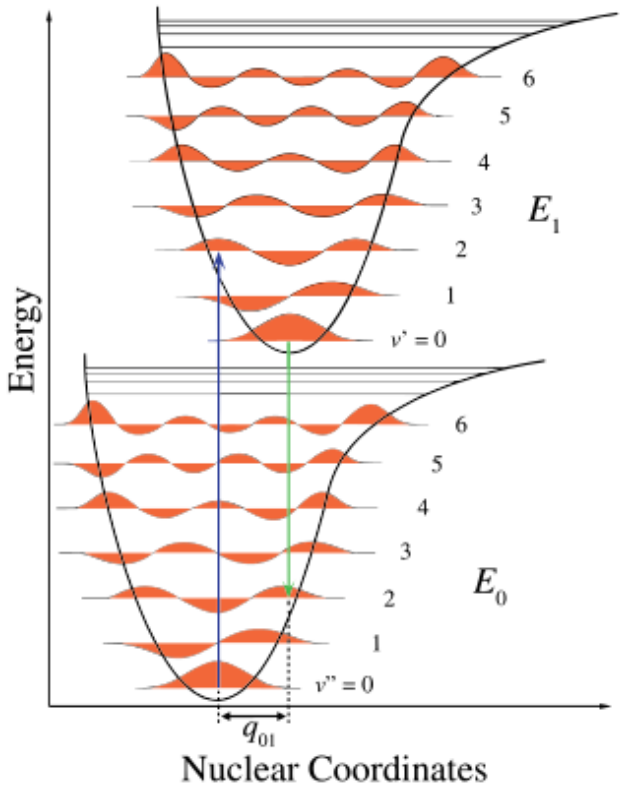

Figure 2.2: Vertical transition illustrating the Frank Condon principle (taken from Wikimedia Commons).

2.1.2 Non-Radiative Decay

Upon excitation following the absorption of a photon as set out earlier, the molecule is now in a higher energy state, and it will naturally seek to return to the lower energy ground electronic state. There are two processes, internal conversion (IC) and inter-system crossing (ISC) (both shown in Figure 2.3), by which it can do so without the emission of a photon. It is these non-radiative pathways that will be investigated first, appropriately as the majority of molecules are not fluorescent and by definition decay non-radiatively to the ground state, in an intrinsic process. However, often the first process to occur, due to collisions with other species including solvent, is relaxation to the lowest vibrational level in the excited electronic state. This may either be concurrent with, or followed soon after by, solvent cage reorganisation to stabilise the new electronic state. In some cases the initial FC state is higher in energy than other lower-lying excited electronic states and there is rapid internal conversion to the lower energy state (S_1 in Figure 2.3). In this case, following the internal conversion there will be more vibrational relaxation and possibly small changes to the solvent shell. These changes can also be visualised using the potential energy surface of the molecule's electronic states, such as the one shown in Figure 2.2.

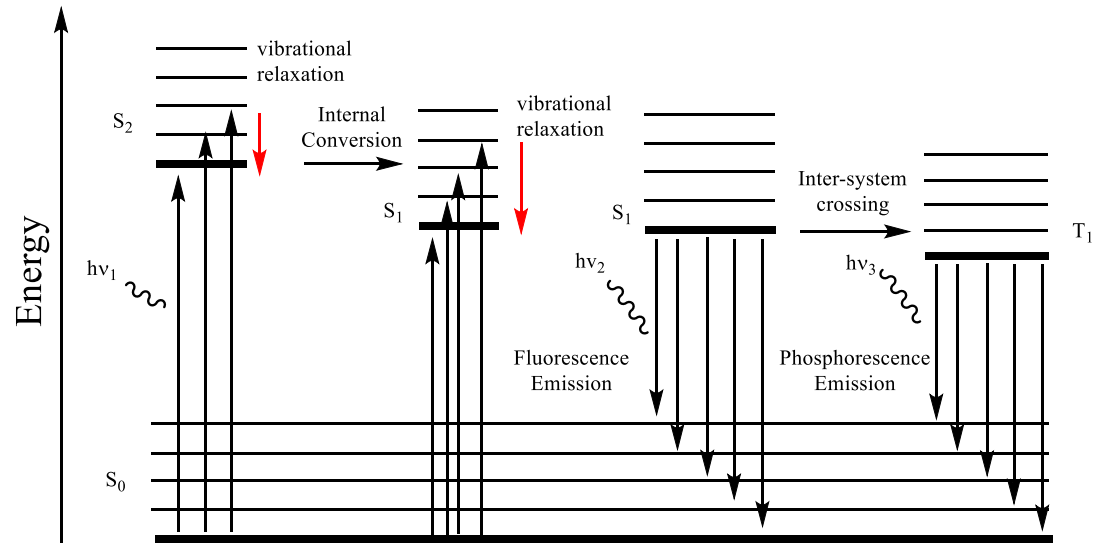

Figure 2.3: Jablonski diagram of electronic transitions involving ground and excited states.

Once in the lowest energy excited state, what happens next is determined by the magnitude of the energy difference between the ground and excited state, in most cases the first singlet state S_1. If the energy gap is relatively small, it is possible for internal conversion between the lowest vibrational level of the excited electronic state and a higher vibrational level in the ground electronic state, followed by vibrational relaxation. However, an intermediate step involving the triplet state is also possible, via inter-system crossing to the T_1 state. The triplet state is always lower in energy than the singlet state, due to greater separation of electrons with the same spin, which stabilises the molecule.

Although ISC seems to contradict the selection rules above, the reader's attention is drawn back to the assumptions made in the derivation of said rules. In particular, the separation of electronic spatial and angular momentum which led to the spin selection rule. Spin-forbidden transitions are an example of the conservation of angular momentum, however the orbitals that electrons occupy themselves have an angular momentum property. The assumption made above is that there is no interaction between orbital angular momentum and electronic spin, but this is not necessarily the case; this is referred to as spin-orbit coupling. Spin-orbit coupling applies particularly to systems with larger numbers of electrons, commonly those containing heavy atoms such as iodine and bromine. In short, spin-forbidden processes such as inter-system crossing can occur in some systems, albeit slowly, and can even be the dominant process.

2.1.3 Radiative Decay

Excitation of a molecule into an excited electronic state with the same spin multiplicity due to absorption of a photon, followed by spontaneous emission of a photon during the decay to the ground electronic state is referred to as fluorescence. Due to IC generally being an extremely rapid process, emission almost always occurs from the lowest-lying electronically excited state (Kasha's rule). Typically, this manifests as a change in wavelength between the absorption and emission peaks, referred to as the Stokes shift. This is practically useful for fluorescence spectroscopy, as this means molecules can be excited at one wavelength and the emission recorded at a second, longer wavelength. The other emissive process illustrated is phosphorescence, which is a spin-forbidden process and occurs as described in the previous section. Phosphorescence is consequently a slow process, with a long-lived excited state which makes quenching by other solvated species much more likely and therefore is not usually observed in solution. Quenching will be dealt with in more detail later, but phosphorescence is not relevant to the work presented in subsequent chapters and will not be discussed further.

$$R_F = -\frac{d[X^*]}{dt} = k_F[X^*] \qquad 2.5$$

Decay of the molecule from the excited state follows first order kinetics, as this process only involves a single species. Hence the rate of decay R_F is equal to the product of the radiative rate constant k_F and the concentration of the excited state species [X*] (equation 2.5). Since the emission intensity is proportional to [X*], the emission intensity decays first order with respect to [X*]. The lifetime of the excited state τ_n is therefore the inverse of the radiative rate constant k_F, however the observed fluorescence lifetime is a combination of both the radiative and non-radiative decay rates. The fluorescence lifetime τ is therefore, as shown in equation 2.6, the inverse of the sum of the radiative rate constant k_F and non-radiative rate constant k_{NR}. In practical terms, the fluorescence lifetime is the time taken for fluorescence intensity to decay exponentially to 1/e of the maximum intensity immediately after excitation.

$$\tau = \frac{1}{k_F + k_{NR}} \qquad 2.6$$

Emission intensity I(t), at time t after excitation, from the first-order kinetics of fluorescence decay shown in equation 2.5, can be seen to decay exponentially from an initial intensity I_0 as a function of time t and fluorescence lifetime τ in equation 2.7 below.

$$I(t) = I_0 e^{t/\tau} \tag{2.7}$$

When fitting to time-resolved fluorescence decay data, however, equation 2.8 is typically used, where α_i and τ_i are the a-factor and fluorescence lifetime respectively. The sum of the A-factors are normalised to 1 and α_i represents the population of the i^{th} species as a fraction of the total emitting population.

$$I(t) = \sum \alpha_i e^{t/\tau_i} \tag{2.8}$$

The efficiency of a molecule's fluorescence emission can be determined from its quantum yield ϕ_F, which is the ratio of photons absorbed and photons emitted. Put another way, it is the proportion of excited state molecules which decay radiatively and can therefore be expressed in terms of the radiative and non-radiative rate constants (equation 2.9). Fluorescence quantum yield can therefore also be related by equation 2.10 (from the combination of equations 2.6 and 2.9) to the fluorescence lifetime.

$$\phi_F = \frac{k_F}{k_F + k_{NR}} \tag{2.9}$$

$$\phi_F = k_F \tau \tag{2.10}$$

2.1.4 Fluorescence Quenching

Fluorescence emission of a fluorophore can be affected by other species in the same solution. A commonly observed effect is quenching, which results in reduced emission intensity and shorter fluorescence lifetimes. Once in the excited state, the fluorophore can interact with other molecules and undergo NR decay. Quenching of fluorescence can occur via a number of mechanisms, but all have some common features, such as some form of energy or charge transfer. Quenching can be described by the Stern-Volmer equation (2.11), where ϕ_0 and ϕ are the emission intensity in the absence and presence of quencher respectively, K_{SV} is the Stern-Volmer quenching constant, and [Q] is the concentration of quencher.

$$\frac{\phi_0}{\phi} = 1 + K_{SV}[Q] \qquad 2.11$$

For systems where only dynamic quenching occurs, which often proceeds *via* a collisional interaction between quencher Q and fluorophore M, K_{SV} is equal to the dynamic quenching constant K_D. In turn, K_D is defined as $k_q\tau_0$, where k_q is the quenching rate constant and τ_0 is the unquenched fluorescence lifetime. Equation 2.11 can be reformulated as below using the fluorescence lifetime ratio τ_0/τ in place of ϕ_0/ϕ, due to the proportional relationship between fluorescence quantum yield and lifetime.

However, if only static quenching is observed, due to the formation of a dimer MQ in the ground state that has a smaller quantum yield than the free fluorophore, then an average quantum yield is observed. This can be defined as:

$$\langle\phi\rangle = \alpha\phi_0 + (1 - \alpha)\phi_{MQ} \qquad 2.12$$

where $\langle\phi\rangle$ is the average quantum yield observed in the presence of quencher and ϕ_{MQ} is the quantum yield of the dimer. The proportion of free M is α, defined as:

$$\alpha = \left(\frac{1}{1 + K_S[Q]}\right) \qquad 2.13$$

where K_S is the equilibrium constant of dimer (MQ) formation. The assumption that the dimer MQ is essentially non-fluorescent, with respect to equation 2.12, can be expressed as $\phi_0 \gg \phi_{MQ}$. Equations 2.12 and 2.13 in combination are then reduced to:

$$\frac{\phi_0}{\langle\phi\rangle} = 1 + K_S[Q] \qquad 2.14$$

In steady-state fluorescence emission measurements, the assumption is often made that the fluorescence intensity ratio I_0/I is equal to the related quantum yield ratio ϕ_0/ϕ. Equation 2.14 then becomes:

$$\frac{I_0}{I} = 1 + K_S[Q] \qquad 2.15$$

Combined static and dynamic quenching can be defined in terms of quantum yield as follows in equation 2.16:

$$\langle\phi\rangle = \frac{\alpha\phi_0}{1 + K_D[Q]} + (1 - \alpha)\phi_{MQ} \quad 2.16$$

As before, if $\phi_0 \gg \phi_{MQ}$, static and dynamic quenching can be defined in terms of the quantum yield:

$$\frac{\phi_0}{\langle\phi\rangle} = 1 + (K_D + K_S)[Q] + K_D K_S[Q]^2 \quad 2.17$$

Making the assumption, once again, that the quantum yield ratio in equation 2.17 is equal to the corresponding intensity ratio allows static and dynamic quenching to be defined in terms of the intensity. This assumption only remains valid if the intensity of excitation light absorbed by the fluorophore remains constant throughout each set of measurements.

$$\frac{I_0}{I} = 1 + (K_D + K_S)[Q] + K_D K_S[Q]^2 \quad 2.18$$

Following similar logic, equation 2.17 (and by extension, equations 2.11 and 2.14) can also be described in terms of fluorescence lifetime. Since fluorescence lifetime is proportional to the quantum yield, the quantum yield ratios described earlier are equal to the fluorescence lifetime ratio τ_0/τ.

2.1.5 Electronic Energy Transfer

Among the various NR decay mechanisms, many involve the transfer of charge or energy from the excited state molecule (the fluorophore) to another ground-state molecule (the quencher) nearby. These transfer mechanisms are largely divided into two categories: electron transfer and energy transfer. Electron transfer is self-explanatory and usually occurs either as photo-induced electron transfer (PET) or charge transfer (CT). While these may seem like different names for the same process, they are distinct processes. CT is generally an intramolecular process and characteristically results in a wavelength shift of the fluorescence emission/excitation. PET can be an inter- or intra-molecular process, *via* electron transfer between a moiety which is electronically distinct from the fluorophore (e.g. not part of the π-electron system of an organic fluorophore) and the fluorophore. The unique characteristic of PET, compared to CT, is a constant emission wavelength.

Energy transfer is also simply defined as the transfer of energy from an excited state species to a ground state species. This category can be further divided into two types, resonance energy transfer (RET) and Dexter energy transfer. RET is distinct in that it involves simultaneously a downward electronic transition of the donor and an upward transition of the acceptor, from interactions between their transition dipole moments. As a result, in addition to the usual selection rules, both transitions require matching energies for this process to be significant, which in practical terms means the wavelength of the absorption peak of the acceptor must be consistent with the energy of the donor's downward transition. It also exhibits an inverse sixth power dependence on the distance between the fluorophore and quencher. For this reason, it is often called the 'molecular ruler', and is also not usually seen unless both donor and acceptor are components within a larger molecule, a conformation of which holds the two at a separation distance of 100's Å or less.

Dexter energy transfer, although overall there is no charge transfer, actually does involve two electron transfers. One electron moves from the highest singly occupied molecular orbital (SOMO) of the excited state fluorophore into the LUMO of the quencher, and a second electron from the HOMO of the quencher to the lowest SOMO of the fluorophore. These transfers can be simultaneous or stepwise.

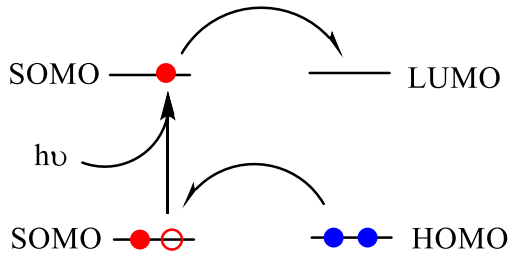

Figure 2.4: Electron transfer diagram of Dexter energy transfer

2.2 DNA

All life on earth, as we know it, passes on genetic information *via* the sequence of bases in DNA strands. Such strands are formed of two main parts: the sugar-phosphate backbone, and the aromatic bases which stack together with adjacent bases on the same strand. Bases on opposite strands form co-planar base pairs, in most cases adenine pairs with thymine (A-T) and cytosine with guanine (C-G). A-T and C-G pairs are usually referred to as Watson-Crick base pairs, shown in Figure 2.5 below.

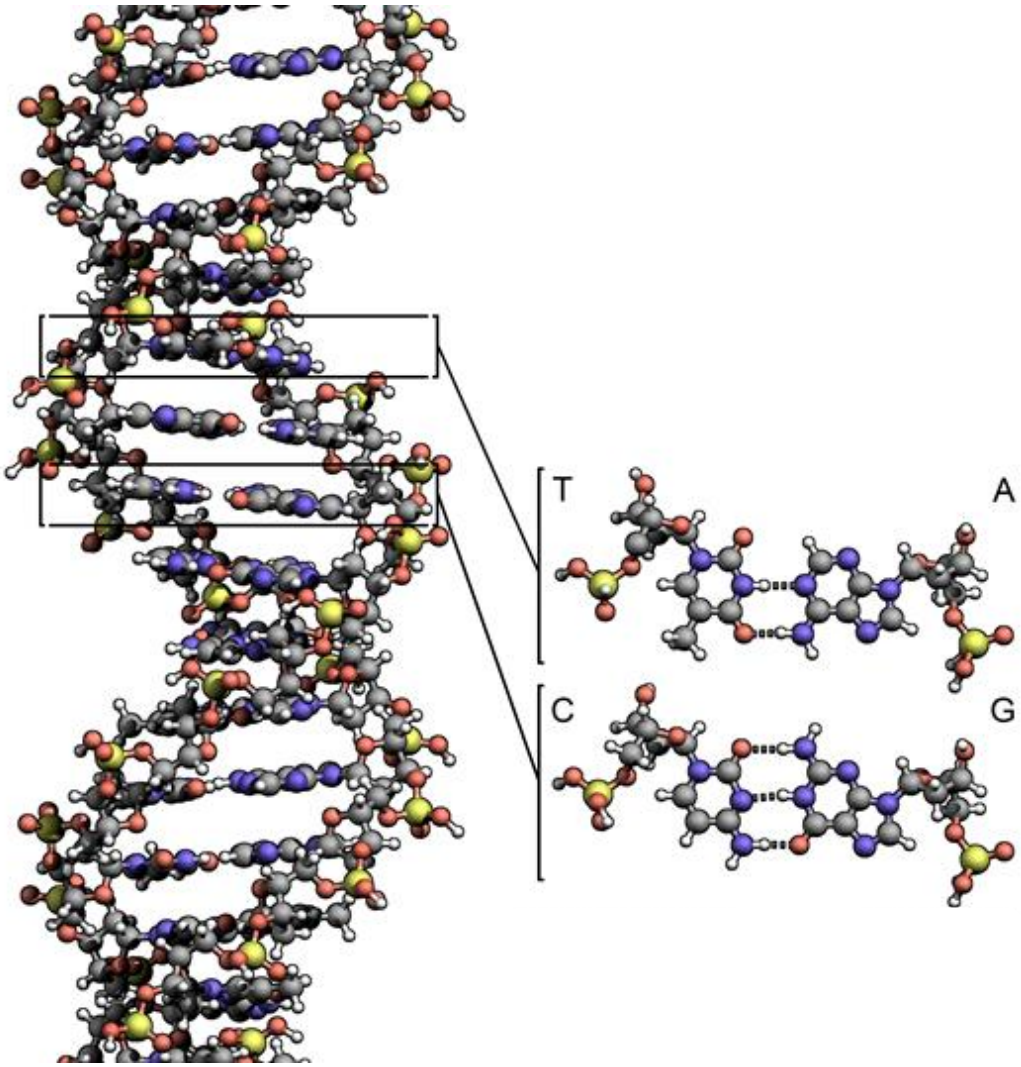

Figure 2.5: Illustration of DNA base pairing and molecular structure.

Purine Based (R)

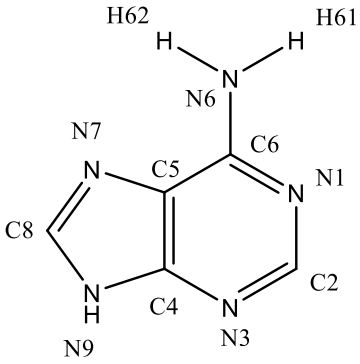

Adenine (A)

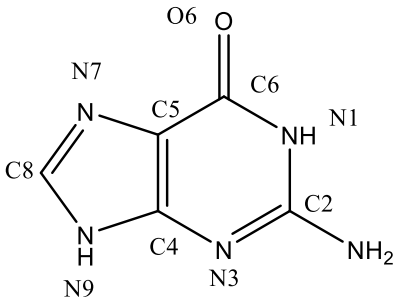

Guanine (G)

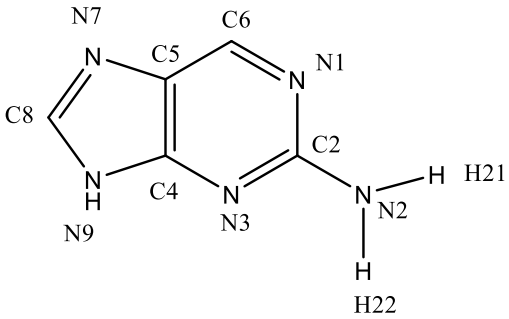

2-aminopurine (2AP)

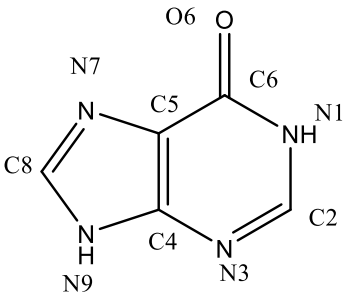

Hypoxanthine/Inosine (I)

Pyrimidine Based (Y)

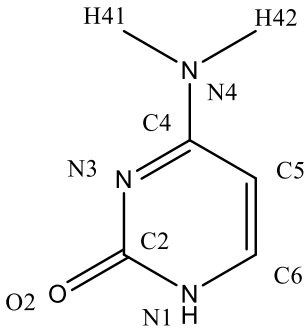

Cytosine

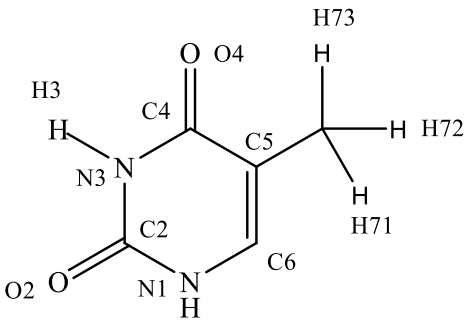

Thymine

Figure 2.6: Structures of natural bases and the fluorescent base analogue 2AP.

DNA bases can be divided into two groups based on their structure: the purines adenine and guanine, which consist of two fused rings; and the pyrimidines cytosine and thymine, which consist of a single six-membered ring. All four bases are numbered at each position according to the convention shown in Figure 2.6, either starting (pyrimidines) or ending (purines) at the nitrogen bound to the sugar moiety. Each of the purine-based fluorescent DNA base analogues 2AP and pA, as well as hypoxanthine/inosine, studied in this work are also shown.

The DNA bases A, C, G & T are covalently bound to the deoxyribose sugars at the 1' position, while the phosphate esters are bonded to 3' and 5' positions (the exocyclic carbon) on the sugar. DNA base sequences are therefore usually described in terms of the phosphate group positions on the sugar ring, with DNA bases listed in order from the terminal phosphate group at the 5' position to the phosphate group at the 3' position, shown in Figure 2.7 below.

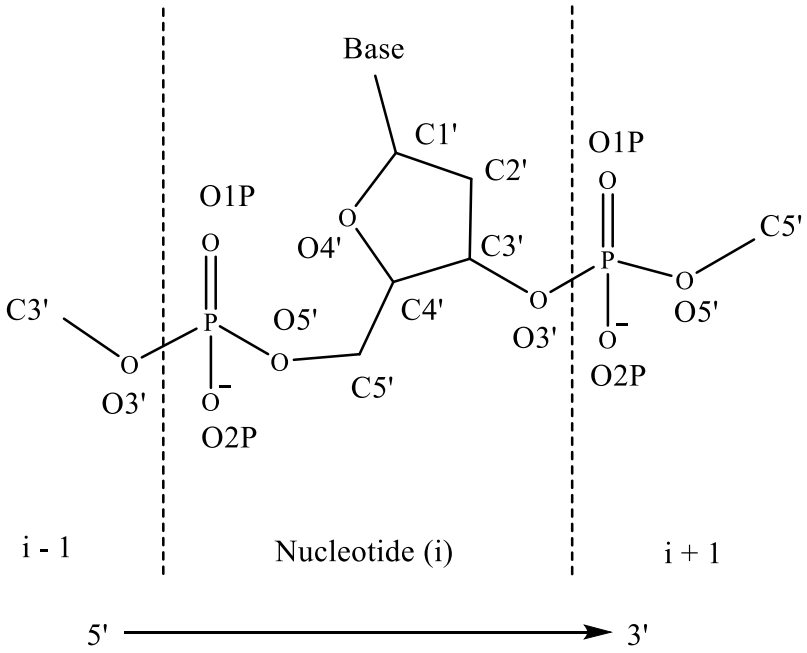

Figure 2.7: DNA sugar-phosphate backbone and conventional sequence direction.

The helical structure of DNA can be described by a series of structural parameters,[6-8] either based on rotation or translation between adjacent pairs of bases (base-step parameters), or dihedral angles in the sugar-phosphate backbone, illustrated in Figure 2.7, linking together the DNA bases.

2.3 Computational Chemistry

Modelling the structure and properties of molecules using computational techniques is the field known as computational chemistry. There are a variety of techniques employed to accurately model different systems, including force-field simulations, quantum mechanical methods, including semi-empirical and *ab initio* methods, density functional theory (DFT), and various combinations thereof. All have their strengths and weaknesses, and the choice of method employed depends on various considerations, such as the size of system to be studied, computational resources, and the nature of the problem to be studied or question asked.

At the most basic level, all computational methods rest on the same principle: first calculate the energy of a system from some initial condition, then try to minimise the energy of the system by altering various parameters. This is most easily visualised for geometry optimisation of a molecule, where the molecular structure is altered until an energy minimum is found, but the basic principle applies regardless of whether the calculation uses the simplest classical method in a molecular dynamics simulation or the highest level of theory with the largest basis set (functions used to represent molecular orbitals) in an excited state calculation.

As already implied in the previous paragraph, a large variety of computational methods are in wide use. These can be divided up into several categories, the first of which are the classical methods already mentioned. Classical methods are simply the application of Newton's laws of motion to the molecular scale and are more commonly referred to as force field methods. Chemical bonds are represented as springs with a force constant that corresponds to the bond strength. However, quantum mechanics shows that particles with the mass and size of atoms do not really behave as classical particles, so for greater accuracy the energy of a system is obtained by solving the Schrödinger equation. Methods that rely solely on obtaining the energy from the Schrödinger equation are referred to as *ab initio* methods. In between force field and *ab initio* methods are semi-empirical methods which rely on parameterisation of QM methods from experiment, or other computational methods, to simplify the calculation. The final category is DFT, which calculates the energy using functionals (functions of functions) of electron density. In theory, DFT is a fully *ab initio* method, but in practice requires some input from QM *ab initio* methods, particularly for the

electron exchange and correlation energy. So DFT is not really either a semi-empirical or *ab initio* method.

In terms of computational speed and accuracy, force-field methods are the least demanding computationally but usually have the lowest accuracy. Semi-empirical methods are the next least demanding computationally, however, this is achieved using a number of simplifications or partial simplifications at the cost of some accuracy. This most often shows up as an overestimate of the energy of some interactions, requiring careful choice of a method based on the system of interest. Finally, DFT and *ab initio* methods are generally the most accurate and similarly the most demanding computationally, although it should be noted the exact order depends on the DFT functional and the *ab initio* method being compared. DFT ranks with the less demanding *ab initio* methods computationally, but can often have as good or better accuracy.

In addition to computational speed and accuracy, there are a number of other important considerations when choosing which method is best suited. When using force-field methods in particular, it is important to bear in mind that these methods dispense with electronic information altogether and model interactions between atoms as spheres connected by springs, using empirically derived parameters. This works well enough, particularly for large systems like proteins with thousands of atoms where it is not feasible to use any other method, but it limits the information that it can provide to situations where the electronic state can be accounted for implicitly using empirical data, such as structure optimisations and vibrational frequency calculations. Hence force-field methods are silent on excited states, electronic transitions, etc., all relevant to UV-visible spectroscopy and fluorescence, which makes force-field methods of extremely limited use in the context of this project and hence will not be discussed further. Given the much greater computational resources that are now available, force-fields are not necessary for the size of systems studied in this thesis. Similarly, the trade-off between accuracy and computational speed in semi-empirical methods make them a poor choice for the work described in this thesis. Other considerations arising for *ab initio* and DFT methods will be discussed in more detail below.

2.3.1 *Ab Initio* Methods

As mentioned above, *ab initio* methods use quantum mechanics to model systems from first principles without empirical data, as the name suggests. That is not to say approximations are not applied, but the use of empirical data is avoided. These methods use the time-independent Schrodinger equation (2.15) with a number of assumptions to reduce the complexity of the calculations. The first assumption, which is applied to almost all *ab initio* methods, is the Born-Oppenheimer approximation, which ignores nuclear motion due to the much shorter timescale of electronic motion. Most other approximations revolve around electron exchange, which is a quantum mechanical interaction between identical particles whose wavefunctions overlap, and electron correlation, which is the interaction between each electron and all the other electrons in the system. For fermions such as electrons, the exchange interaction effectively results in increased repulsion between electrons with overlapping wavefunctions.

2.3.1.1 Hartree-Fock

At the earliest stages of development of the field of computational chemistry, with the much more limited processor power available at the time, it is logical that for purely quantum mechanical methods the maximum number of possible simplifying approximations were applied in order to make the calculations tractable. From this approach comes the simplest *ab initio* method, Hartree-Fock (HF), where the electron exchange-correlation energy is completely neglected. In effect, the electrons are treated as completely independent, by decomposing the wavefunction ψ into molecular orbitals (MO) which are one-electron wavefunctions ϕ_n. These one-electron wavefunctions make up a Slater Determinant, to preserve the anti-symmetry of the wavefunction (change of sign when electrons are swapped).

$$H^{elec}\psi^{elec}(\vec{r},\vec{R}) = E^{eff}(\vec{R})\psi^{elec}(\vec{r},\vec{R}) \qquad 2.19$$

Secondly, the HF wavefunction consists of a single Slater Determinant, which means that electron-electron repulsion is only included as an average (electron correlation is neglected). The third approximation is the representation of MO as linear combinations of atomic orbitals (basis functions), as in equation 2.20 where ϕ_i is the MO, $c_{\mu i}$ is the expansion coefficient and χ_μ is the atomic orbital (AO) or basis function.

$$\phi_i = \sum_{\mu=1}^{N} c_{\mu i}\chi_u \qquad 2.20$$

The atomic orbitals are defined beforehand in the basis set (this will be discussed in more detail later), leaving only the expansion coefficients to be determined. A concept called the variation principle (the energy of approximate wavefunctions always have an energy greater than or equal to the exact energy) is used. This leads to solving for the "best" set of expansion coefficients by attempting to minimise the energy of each MO using standard numerical techniques, and is referred to as the self-consistent field (SCF). The biggest problem with HF, although more accurate than semi-empirical and classical methods, is the lack of electron correlation. This is addressed in varying degrees using a variety of approaches in methods collectively referred to as post-HF methods.

2.3.1.2 Post-HF Methods

Configuration Interaction (CI) is the first post-HF method, which includes electron correlation by adding additional Slater Determinants (SD with occupied MO replacing unoccupied (virtual) MO to form excited state SD). MO are solved for the first SD as before using the variation principle and then copied to each excited SD without being re-optimised. In principle, every possible excited SD could be included (Full CI), however in practice a small set of excited SD (truncated CI) is used e.g. CISDT, where SDT refers to single, double and triple excitations.

Another method based on CI is Multi-Configuration SCF (MCSCF), where in addition to the first SD being optimised using the variation principle, the MO in the excited SD are optimised instead of being copied from the ground state SD. A special case of MCSCF is also sometimes used, called Complete Active Space SCF (CASSCF), where essentially full CI is performed over a carefully chosen range of higher energy occupied MOs and lower energy unoccupied MO (the "active space"). All other MO not included in the active space are treated the same as for CI. These two methods are often used to describe excited states or in systems with low-lying excited states nearly degenerate with the ground state. They do recover some electron correlation, but mostly "static" correlation and less of the correlation due to electron motion.

A very computationally demanding, but very accurate method is multi-reference CI (MRCI) which uses the MCSCF wavefunction to generate excited SDs. This is not much used except for small systems. Back to the other end of the scale of computational complexity, there is Moller-Plesset perturbation (MP) theory which applies a series of corrections to HF to account for electron correlation. This is the least computationally expensive *ab initio* method after HF. A first order MP (MP1) adds one correction term to the energy equation, second order (MP2) adds two terms, etc. MP2 is the most common, as the first correction is always negative. The idea that the energy would converge to the correct value after adding more terms has been shown to be false by Olsen *et al*[9] in some cases, suggesting the extra computational demands are not an efficient use of computational resources.

Rather than add additional corrections, or go to a more demanding level of theory like MCSCF or MRCI, coupled cluster (CC) theory is often used instead. Coupled cluster applies all corrections for given types (i.e. single, double, etc. excited SDs) to infinite order e.g. CCSD applies all corrections using single and double excited SDs. Coupled cluster is often used as the "gold standard", in particular CCSD, which is often used to validate less demanding methods for particular systems.

In summary, a range of *ab initio* methods exist, starting with Hartree-Fock as a base, and adding various improvements that have varying effects on computational resources and accuracy. Computationally these are often ranked as follows (in order of increasing computational demand): HF < MP2 < CCSD < CCSD(T) << MRCI, as shown in calculations of the dissociation energy of N_2 by van Mourik *et al*.[10]

2.3.2 Density Functional Theory

Density functional theory is a method somewhat distinct from both *ab initio* and semi-empirical methods, in that it uses the energy density instead of the wavefunction to model molecular systems. This is based on Hohenberg-Kohn theory, which states that the relationship between energy density and the ground state energy can be described by a functional. The exact form of this functional is not known, only various approximations of it. Another issue is that dispersion is not accounted for in DFT, although various functionals now include this implicitly or using empirical corrections (hence the distinction from *ab initio* methods stated earlier). Such a variety of functionals can be helpful as they have different advantages, but it adds an extra

consideration on top of deciding which level of theory and basis set (set of atomic orbitals) to use.

DFT functionals have been improved over several decades, such that several generations of functionals exist. In the earliest days of DFT, moving to wave mechanics methods to calculate the kinetic energy density was a significant leap. This left only the correlation energy to be corrected for, which is where subsequent improvements were focused. The first such improvements were the local density approximation (implying a uniform electron gas) and the generalised gradient corrected version (non-uniform electron gas) such as VWN5, BLYP functionals, currently less used. Further improvements came from using the second derivative of the electron density and including the HF exchange energy to create modern functionals (e.g. B3LYP, M06-2X).

Where traditional *ab initio* methods are by and large mature and not subject to significant changes currently, DFT is a relatively more recent theory which is still subject to revision and improvement. M06-2X, the functional mentioned earlier, has only in the last few years come into widespread use and is slowly replacing the B3LYP functional. M06-2X is reported to be more accurate at modelling dispersion and other electrostatic interactions,[11] which DFT typically is considered to handle poorly.

2.3.3 Basis Sets

One further parameter that needs to be defined for an *ab initio* or DFT calculation is the functions that represent single electron orbitals in the system being studied. Two main types of function are used to represent electrons, Slater functions (equation 2.21) and Gaussian functions (equation 2.22). Slater functions generally represent electron orbitals more accurately but are computationally more expensive.

$$R \propto e^{-\alpha r} \qquad 2.21$$

$$R \propto e^{-\alpha r^2} \qquad 2.22$$

Hence, Guassian functions are more commonly used for faster calculations despite requiring more functions per orbital to match the accuracy of Slater orbital functions. Only a simplified version of a Gaussian function (the radial part) is shown in equation 2.22, but these equations can be modified to account for very disperse electron density or polarisation. Other types of basis set functions exist, such as plane

wave functions, which are useful for periodic or crystalline structures, but are not relevant to this work and will not be discussed further.

There are also several ways to arrange the basis set functions used to describe the system of interest. It would seem obvious at first to just assign the same number of Guassian functions to every orbital, but for most systems this would be an unnecessary computational expense. Most chemical and physical properties involve the valence electrons of atoms, with very limited or no input from the core orbitals. Therefore it makes sense to focus computational resources on valence orbitals, which is one reason for the widespread use of Pople-type split-valence basis functions. These take the form X-YZ, where X is the number of Gaussian functions linearly combined to represent the core electron orbitals. The valence orbitals are described by two separate functions, which are linear combinations of Y and Z Gaussian functions, respectively. Additional functions can also be added to those describing the valence orbitals if desired. For example, the basis set used later in this thesis, 6-31+G*, describes the core orbitals with a linear combination of 6 Gaussian functions. Valence orbitals are described by two separate linear combinations of 3 Gaussian functions and 1 Gaussian function. In addition, heavy atoms are described with extra diffuse (+) and polarisation (*) functions.

As mentioned throughout this section, computational expense is a key factor to consider when setting the parameters of theoretical calculations, especially for large polyatomic molecules. Increasing the number of Gaussian functions used to describe orbitals does generally increase the accuracy of a calculation, up to the limit of the ‘complete’ basis set, but this comes at the expense of increased computational time. Generally, there is a law of diminishing returns and increased accuracy is balanced against the extra computational cost incurred when selecting a basis set. A double zeta plus polarisation basis set such as 6-31+G*, which has twice as many orbital functions than is required minimally for the valence orbitals, is used here for the reason that it offers sufficient accuracy for the purposes of this work at minimal computational cost.

2.4 References

1. J. R. Lakowicz, *Principles of Fluorescence Spectroscopy*, Springer, 3rd edn., 2006.
2. G. M. Barrow, *Introduction to molecular spectroscopy*, McGraw-Hill, 1962.
3. J. P. Simons, *Photochemistry and spectroscopy*, Chichester : Wiley-Interscience, Chichester, 1971.
4. J. M. Hollas, *Modern Spectroscopy (Fourth Edition)*, 2004.
5. J. B. Birks, *Photophysics of Aromatic Molecules*, Wiley-Interscience, 1969.
6. R. E. Dickerson, *Nucleic Acids Research*, 1989, **17**, 1797-1803.
7. R. E. Dickerson and H.-L. Ng, *Proceedings of the National Academy of Sciences*, 2001, **98**, 6986-6988.
8. W. K. Olson, M. Bansal, S. K. Burley, R. E. Dickerson, M. Gerstein, S. C. Harvey, U. Heinemann, X. J. Lu, S. Neidle, Z. Shakked, H. Sklenar, M. Suzuki, C. S. Tung, E. Westhof, C. Wolberger and H. M. Berman, *Journal of Molecular Biology*, 2001, **313**, 229-237.
9. J. Olsen, O. Christiansen, H. Koch and P. Jorgensen, *The Journal of Chemical Physics*, 1996, **105**, 5082-5090.
10. A. K. Wilson, T. Van Mourik and T. H. Dunning Jr, *Journal of Molecular Structure: THEOCHEM*, 1996, **388**, 339-349.
11. R. S. Hunter and T. van Mourik, *Journal of Computational Chemistry*, 2012, **33**, 2161-2172.

Chapter 3 Experimental

Three main experimental techniques were used in the work described in this thesis: absorbance spectroscopy, steady-state fluorescence spectroscopy, and time-resolved fluorescence spectroscopy. Theoretical calculations were carried out using Density Functional Theory (DFT). Details of the experimental and theoretical methods undertaken in this thesis will be contained within this chapter, details specific to each chapter will be included within the relevant chapter.

3.1 Absorption Spectroscopy

UV-visible absorption spectra were measured using a Cary 300 UV-visible spectrometer. A zero/baseline correction obtained using the solvent or pH buffer of the system of interest was applied to all spectra. All measurements were performed in dual-beam mode with 10 mm path length fused silica cuvettes, using a reference cuvette filled with the relevant solvent/buffer system. A zero/baseline correction was applied by measuring the transmittance of the blank solvent/buffer solution, as well as the transmittance of the blocked sample beam. Sample measurements were repeated three times to obtain standard deviations and means, which were used to calculate concentration.

3.2 Steady-state Fluorescence Spectroscopy

Where not otherwise stated measurements were carried out at room temperature, 20 °C. Steady-state fluorescence emission spectra were measured with a photon-counting Horiba Fluoromax-P spectrometer, the configuration of which is shown in Figure 3.1 below. An ozone-free xenon arc-lamp (150 W) was used as the excitation source, the resulting beam of which is directed through a Czerny-Turner type monochromator, consisting of entrance (3) and exit (7) slits set to the same bandwidth, with a diffraction grating (5) mounted on a motorised rotating stage. The resulting monochromatic light is sent to the sample chamber. A beamsplitter sends part of the excitation beam to a photodiode which records the lamp intensity as a photocurrent. Fluorescence emission is collected at right angles and passed through the emission monochromator (14-18), before being detected by a photomultiplier tube. The Fluoromax-P spectrometer was operated and data recorded by the Fluoressence

software running on a host computer. Origin graphing software was used to analyse the spectral data.

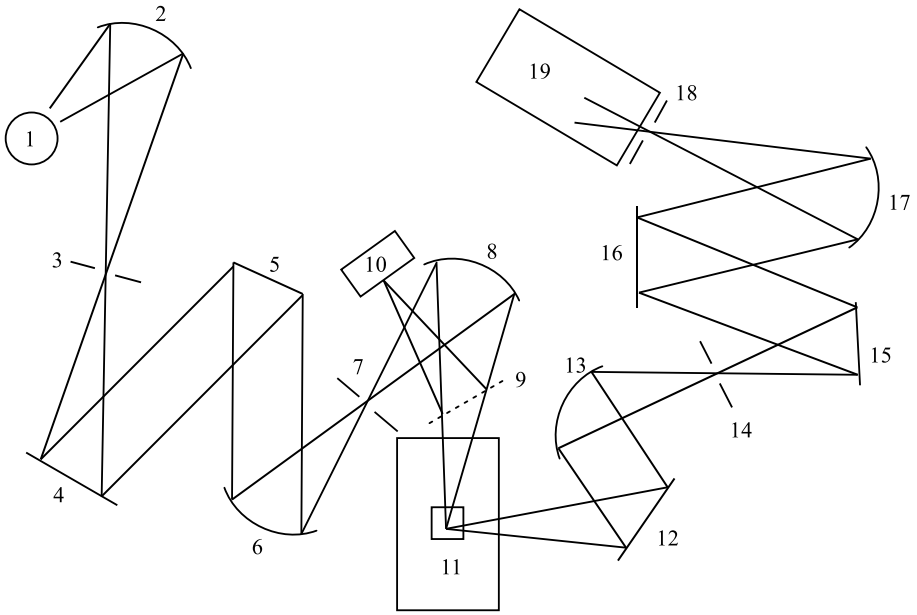

1. Xenon arc-lamp
2. Collection mirror (excitation)
3. Entrance slit (excitation)
4. Deflection mirror (excitation)
5. Diffraction grating (excitation)
6. Focussing mirror (excitation)
7. Exit slit (excitation)
8. Collection mirror (excitation)
9. Beamsplitter (reference)
10. Photodiode (reference)
11. Sample chamber and cuvette holder
12. Deflection mirror (emission)
13. Focussing mirror (emission)
14. Entrance slit (emission)
15. Deflection mirror (emission)
16. Diffraction grating (emission)
17. Focussing mirror (emission)
18. Exit slit (emission)
19. Photomultiplier tube

Figure 3.1: Schematic diagram of Fluoromax-P spectrometer used to obtain steady-state fluorescence spectra.

A fused silica micro-cuvette (200 µL) with 10 mm excitation and 2 mm emission path lengths was used to obtain fluorescence emission spectra. Emission and excitation bandwidths were chosen to maximise the emission intensity of the most intense sample, while keeping the number of counts per second under $4x10^6$ to minimise any non-linear response of the detector. An integration time of 0.1 s was used. For all samples, both the raw intensity data and the intensity corrected for the lamp output were recorded.

3.3 Time-resolved Fluorescence Spectroscopy

Time-resolved fluorescence spectra were collected using time-correlated single photon counting (TCSPC). The entire experimental setup, except for the controlling PC and cooling water baths, described in this section was kept on a vibrationally isolated table in a laboratory maintained at 20±1 °C in the COSMIC

(collaborative spectroscopy, micro-manipulation and imaging centre) facility in JCMB at the University of Edinburgh. Where the temperature is not stated, experiments were carried out at room temperature. TCSPC involves the measurement of the time between excitation of the sample (START pulse) and the arrival of the first emitted photon at the detector (STOP pulse). These times are recorded and cumulatively added to a single histogram until the peak channel reaches 10000 counts. The experimental setup used for TCSPC is shown in Figure 3.2 below. This entire setup, with the exception of the lasers, the pulse picker and the harmonic generator, were controlled by a host computer running Edinburgh Instruments' F900 software and containing a TCC900 Mark II PC expansion card.

Molecules absorbing a photon at the appropriate wavelength enter an excited electronic state for a finite, although very short (ps to ns), time. For fluorescent molecules, the fluorescence lifetime is defined as the time taken after excitation (t = 0) for the fluorescence emission intensity to fall to 1/e of its original value at time t = 0. TCSPC works by counting the number of photons emitted at given intervals after excitation and building up a histogram. Since fluorescence decay is an exponential process, the decay curve can be described using an exponential or sum of exponentials as:

$$I(t) = \sum_i \alpha_i e^{-t/\tau_i} \qquad 3.1$$

Equation 3.l is used to obtain the fluorescence lifetime τ and pre-exponential factor α for each emitting species present. The coefficient α is a measure of the contribution of each emitting species to the total observed emission.

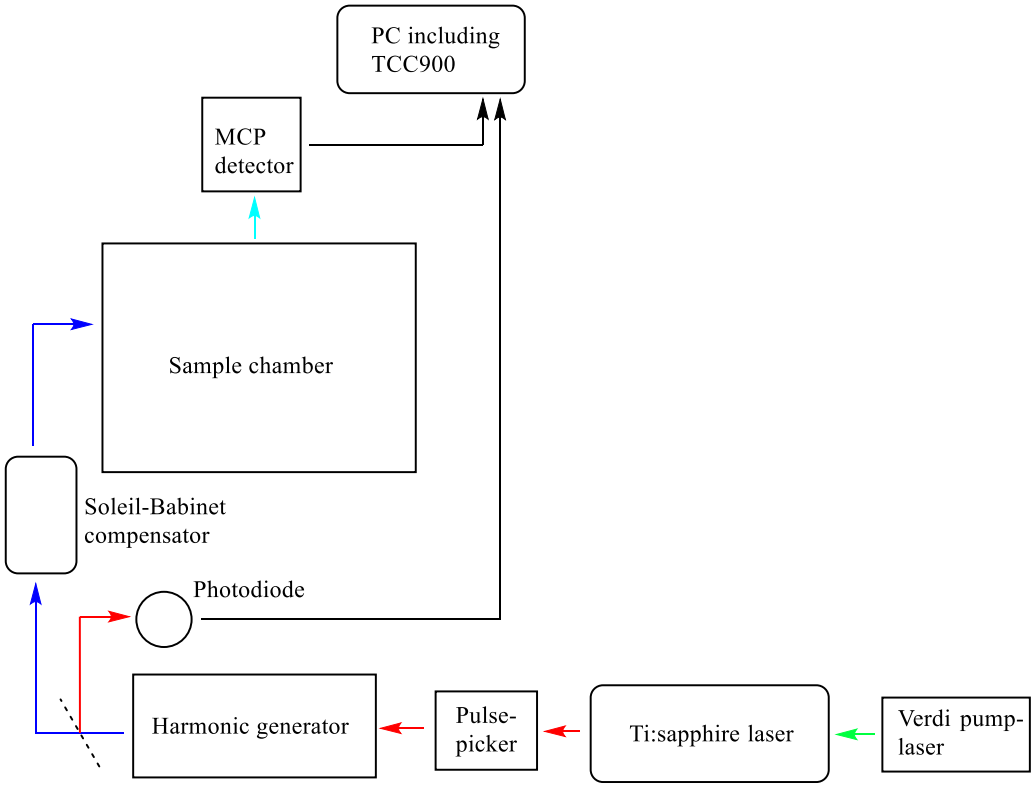

Figure 3.2: Equipment layout used to measure time-resolved fluorescence decays via time-correlated single photon counting.

The TCSPC setup used is shown in Figure 3.2 above. A photodiode was used to produce the START pulse, from residual second harmonic or fundamental of the excitation laser, which was passed to a constant fraction discriminator (CFD). Voltage of the START pulse was adjusted to 1 V using an oscilloscope. The CFD was set to trigger a time-to-amplitude converter (TAC) for pulses above 300 mV. Both the CFD and the TAC were located on the TCC900 card. A Soleil-Babinet compensator was used as an excitation polariser, which is wavelength-sensitive. The resolution of the excitation polariser therefore has to be set electronically according to equation 3.1, where λ is the excitation wavelength.

$$resolution = {}^{41.62}/_{\lambda} \qquad 3.1$$

Due to an error in the start-up sequence of the software, the excitation polariser had to be electronically set to 0 ° and then manually adjusted to the correct value, before being set to 90 ° electronically. Excitation pulses from the laser system, detailed below, were passed through the excitation polariser before being sent to the sample chamber. Emitted photons perpendicular to the excitation source were collected and passed through an attenuator, then a polariser and a Czerny-Turner type Edinburgh

Instruments monochromator. The entrance and exit slits were set manually to 10 nm. A diffraction grating with 1800 lines/mm was used. From equation 3.2, anisotropy *r* is zero when $\cos^2 \theta = 1/3$, where θ is the angle of the polariser. As anisotropy measurements were not required, the polariser was set to the magic angle 54.7 °C, hence anisotropic effects were removed from the emission decays measured.

$$r = \frac{3(\cos^2 \theta)-1}{2} \qquad 3.2$$

A pulse above 80 mV from fluorescence emission of the sample was recorded by a Hamamatsu R3809U series micro-channel plate photomultiplier tube (MCP-PMT), which was cooled by flowing water from a water bath. This STOP pulse was sent to the TCC900 PC card and halted the TAC linear voltage ramp with time. The final voltage is converted into a digital value by an analogue-to-digital converter (ADC) that was binned into one of 4096 channels.

A tuneable, mode-locked Coherent Mira Ti:sapphire laser, pumped by a 10 W Coherent Verdi continuous wave laser at 532 nm, was the excitation light source. Pulses from the Ti:sapphire laser, with a repetition rate of 76 MHz and a duration of ~100 fs, were passed to a pulse-picker. Every 16th pulse was allowed through the pulse-picker, the remainder being rejected or dumped, consequently reducing the pulse frequency to 4.75 MHz. From the pulse-picker, the remaining pulses were passed to a harmonic generator, where the second harmonic was produced by frequency doubling in a barium boronate (BBO) crystal. The fundamental pulse was separated from the second harmonic and sent along a path with a delay stage to optimise pulse matching, before being recombined with the second harmonic pulse in a lithium triboronate (LBO) crystal to generate the third harmonic. Second or third harmonic light, as desired, was then passed to the spectrometer to be used as the excitation source.

Samples were measured using the same quartz cuvette with 10 mm excitation and 2 mm emission paths as in the steady-state fluorescence measurements. The instrument response function (IRF) was measured at the wavelength of the excitation source. For experiments using the second harmonic as the excitation source, the full width at half maximum (FWHM) of the IRF was ~110 ps, while for the third harmonic the FWHM was typically ~80 ps. IRF measurements were taken at the beginning and end of every set of measurements, and repeated every 2-3 hours, where data collection took longer than three hours.

Stern-Volmer quenching constants of 2AP by the natural DNA bases were measured with an emission wavelength of 380 nm at room temperature using the third harmonic at 310 nm as the excitation source. Fluorescence decays of 2AP-containing dinucleotides were measured at 5, 10, 15, 20 and 25 °C by running water from a temperature-controlled water bath through the cuvette holder. Third harmonic light from the harmonic generator at either 310 or 260 nm was used as the excitation source. Separate decays were measured with emission set to 360, 380 and 400 nm for every excitation wavelength and temperature combination. Quenching measurements of pAr were taken at room temperature, using the second harmonic at 390 nm as the excitation source. An emission wavelength of 420 nm was used for every pA lifetime measurement.

Fluorescence lifetimes were obtained from the decay data by iterative non-linear least squares fitting and reconvolution with the appropriate IRF, using Edinburgh Instruments' FAST software suite. Fitting was performed over the range from within a few channels of the IRF peak at 10^4 counts to where the decay had fallen to tens of counts. The background was fixed to 1 or 2 counts, depending on the noise in the decay. Global fitting was performed over multiple decays by choosing the range of channels based on the shortest decay. From each fit, the χ^2 value and the randomness of the residuals were examined to determine the quality of the fit. A χ^2 value above 1.2 was considered a poor fit, and any non-random pattern in the residuals was taken as a sign that an extra lifetime component was required. Starting with one lifetime component, where the quality of the fit was poor, the number of lifetime components was increased until a sufficiently good fit was obtained.

3.4 DFT calculations

Geometry optimisations were performed using DFT calculations in the Gaussian 16 software suite. Frequency calculations on the resulting optimised structures were performed to ensure an energy minimised structure was obtained. Implicit solvation by water, with a dielectric coefficient ε of 78.3553, was included using a polarisable continuum model (PCM). The M06-2X functional and the double-zeta polarised basis set 6-31+G* were chosen, with an ultrafine numerical integration grid (99,590) and tight convergence criteria of forces. Calculations were carried out on the Eddie 3 computing cluster using parallel processing on Intel Zeon processors.

Chapter 4 Quenching of 2-aminopurine Fluorescence by the Natural Bases

"Discovery: A couple of months in the laboratory can frequently save a couple of hours in the library."

Anonymous

4.1 Introduction

2-aminopurine (2AP, shown in Figure 4.1) has been extensively used throughout the literature as a semi-intrinsic fluorescent probe of DNA conformation, due to its well-characterised photophysical properties.[1] In this chapter, steady-state and time-resolved fluorescence measurements will be presented in order to better characterise the interactions between 2AP and the natural bases that give rise to fluorescence quenching, which allows 2AP to be used as a fluorescent probe. These results will also be used as proof of principle for a method that can potentially be used to predict the behaviour of a fluorescent probe in DNA strands. Inosine (also referred to as hypoxanthine) is a non-canonical base which has a reported redox potential of zero or nearly zero relative to 2AP,[2] the significance of which will be discussed later.

In water, 2AP has a fluorescence quantum yield of 0.68, with an absorption peak at 303 nm and an emission peak at 370 nm. 2AP also has an average fluorescence lifetime of ~11.5 ns in water, however, the lifetime of free 2AP is wavelength dependent due to the existence of tautomeric forms, shown in Figure 4.2, that have slightly different lifetimes.[3] Due to the similar values of the two lifetime components, a mono-exponential lifetime is usually quoted for 2AP. For 2AP riboside (r2AP), the proton is replaced with a riboside moiety which prevents tautomerisation and therefore only a single fluorescence lifetime is observed. This also holds for 2AP-containing oligonucleotides, as the 2AP 'base' is attached to the backbone by the riboside sugar at the 9N position. The absorption of 2AP is substantially red-shifted compared to the natural DNA bases which absorb at ~260 nm, allowing 2AP to be selectively excited, and the quantum yield is a huge improvement over its natural isomer, adenine (~10^{-4}), or any of the other natural bases.[1]

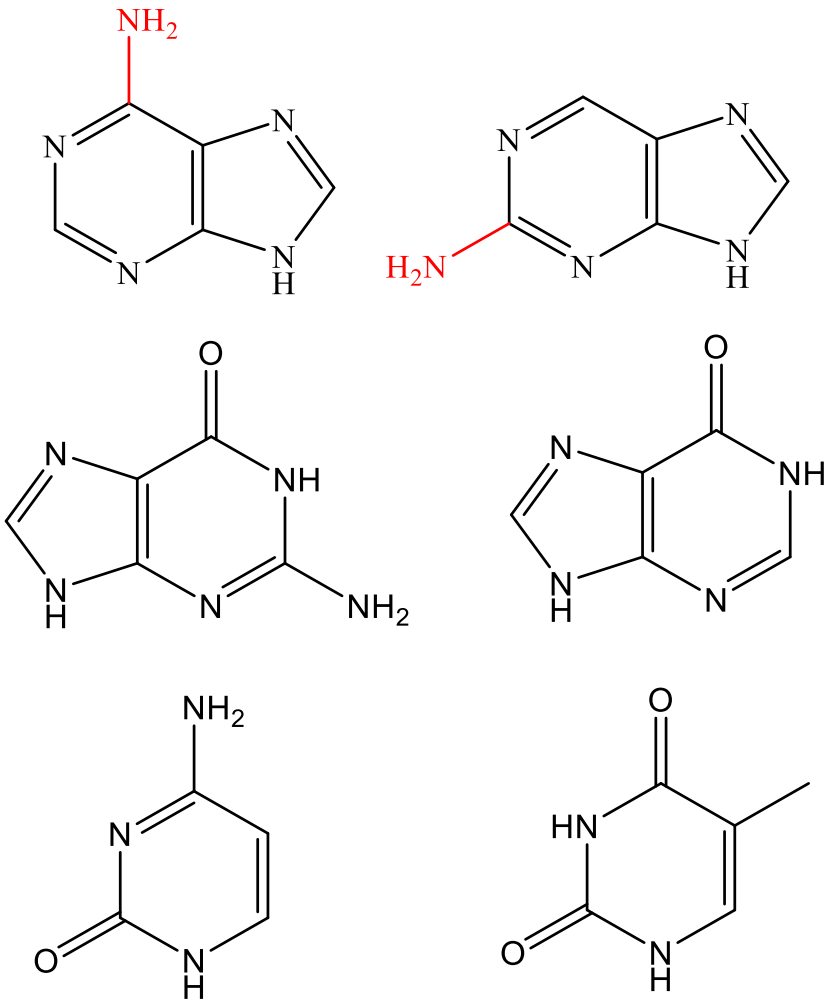

Figure 4.1: Structure of adenine (top left) and 2-aminopurine (top right), as well as the bases guanine (centre left), inosine (centre right), thymine (bottom right) and cytosine (bottom left).

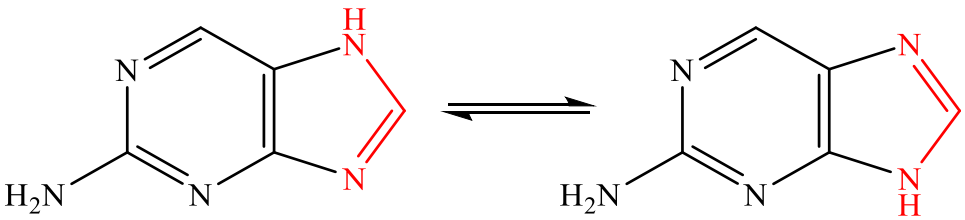

Figure 4.2: 7H (left) and 9H (right) tautomers of free 2AP in solution

The first report of 2AP as a potential fluorescent probe of DNA structure was made by Ward *et al*.[4] Oligonucleotide strands were prepared using monophosphate ribosides and enzyme catalysis, strongly suggesting that the structure of 2AP is sufficiently similar to adenine to overcome the specificity of enzyme binding that would normally reject modified substrates. This was an early indication that the substitution of adenine with 2AP does not significantly perturb the natural structure of the DNA helix. The authors went on to state that incorporation of 2AP into an oligonucleotide results in a 100-fold decrease in quantum yield. Subsequent denaturation was reported to show an increase in fluorescence emission between 3- and 10-fold. Both the combination of the decrease in emission intensity, and its subsequent partial recovery after denaturation, suggested that 2AP might be a useful fluorescent probe of DNA conformation. This potential application as a probe set the stage for an explosion in work involving 2AP over the intervening decades.

Structural studies of 2AP-containing oligonucleotides employing NMR[5] and melting temperatures[6-8] showed that 2AP and thymine form a Watson-Crick base pair. Base stacking of 2AP in dinucleotides was investigated computationally by Smith *et al*[9], a facet of DNA structure which has, until quite recently, mostly been neglected with regards to 2AP. They reported that the optimised structures obtained closely resembled a typical B-DNA conformation. A recent NMR study by Dallmann and co-workers[10] supported this conclusion, comparing two strands of DNA with identical sequence context but for the substitution of adenine with 2AP. The authors reported that substitution by 2AP has only a weak effect on the average helical structure, although there is a larger impact on the dynamics, particularly the base-pair lifetime (the average time before the base-pair hydrogen bonds are broken).

The efficient quenching of 2AP fluorescence emission in properly stacked B-DNA strands compared to free 2AP was reported by Barton and colleagues in more detail.[7, 8, 11, 12] They showed that the fluorescence quenching mechanism operates via electron transfer, and that the effect of neighbouring DNA bases on 2AP fluorescence is highly dependent on sequence context and conformation.[13-18] Neely and Jones[19, 20] showed that 2AP stacked in DNA at room temperature in solution has extra shorter lifetime components (four resolvable components, in total) compared with free 2AP in solution. These four components were attributed to four separate conformations of DNA, or more likely, four families of conformations with similar 2AP fluorescence

lifetimes, consistent with findings that 2AP fluorescence is sensitive to DNA conformation. Larsen *et al*[2] used dinucleotide strands containing 2AP to show a clear trend of the effect on the 2AP fluorescence intensity, which depends on the identity of the neighbouring base; in order of decreasing effect on the emission intensity of 2AP, G > A ~ T > C.

4.1.1 Quenching of free 2AP in solution

Rachofsky *et al*[21] carried out further investigation of the quenching process with measurements of collisional quenching of d2AP by the free nucleosides, ATP and GTP in tris buffer (20 mM). In their report it was shown that greater quenching by dT, ATP and GTP was observed from steady-state fluorescence measurements than for time-resolved data in higher buffer concentration (200 mM), particularly at higher quencher concentrations. This extra quenching in the steady-state data appeared as upward curvature of the plotted data, rather than a linear trend that would normally be expected. From these data they concluded that there are two simultaneous quenching processes taking place in solution: dynamic quenching as a result of collisional interactions between excited 2AP and quencher; and static quenching which arises from ground-state interactions between 2AP and quencher. For the quenching by the nucleosides in tris-HCl buffer (20 mM), only dynamic quenching was reported, shown in Table 4.1.

nucleoside	k_q /10^9 M^{-1} s^{-1}	K_{SV} /M^{-1}
rG	1.70±0.13	17.8
rA	2.21±0.10	22.5
dT	2.14±0.04	21.8
rC	1.90±0.03	19.4

Table 4.1: Quenching rate constants (k_q) and Stern-Volmer constants (K_{SV}) for d2AP by the natural nucleosides obtained from time-resolved fluorescence data. Table adapted from reference [21].

There are, however, a number of unsatisfactory aspects with this report[21] that quickly become apparent. It is hard to be definitive, as only a small subset of their data is published, but the Stern-Volmer plot of d2AP quenching by dT from steady-state fluorescence measurements shows significant upward curvature. The authors go on to state that similar behaviour is observed for the other nucleosides which indicated both static and dynamic quenching processes, however they also state that static quenching could not be reliably determined due to the reduced solubility of rA, rC & rG. This

does not explain why a static quenching value for dT was not reported under the same buffer conditions. Reasonably, that may be the case due to practical issues inherent with fitting of non-linear curves, particularly correlation between parameters.

Their interpretation of the fluorescence lifetime data also seems odd, although it may have been driven by the state of knowledge within the field at the time of publication. In particular, the assumption was made that statically quenched, stacked complexes are non-emissive and therefore do not contribute to the observed decay curve; it was not recognised that the stacked 2AP may simply appear as a shorter lifetime component. The reported appearance of additional shorter lifetime components at higher concentrations of dT is consistent with the stacked complexes exhibiting a very short lifetime. Rachofsky *et al*[21] presented an alternative transient diffusion model to explain the deviation from single exponential decay at higher quencher concentrations, but the model assumes only collisional quenching is observed in the measured decay curves. This mechanism is plausible, but seemingly contradicts their later statement that both static and dynamic quenching of 2AP fluorescence occur in combination. No satisfactory reasoning or evidence was given to support this model over any other, besides noting that a satisfactory fit is obtained, nor to explain why the deviation from a single exponential decay cannot be attributed to the presence of static quenching.

A more recent publication by Narayanan *et al*[22] reported the results of a similar study using the nucleotide monophosphates as quenchers in phosphate buffer (0.1 M). In contrast to the earlier quenching study,[21] they reported clear evidence of static quenching for all NMP except CMP. Their results also present a different trend of dynamic quenching efficiencies, and higher quenching constants on average. Despite this, their reported quenching rate constants are noticeably lower than the earlier study. These rate constants were calculated using a fluorescence lifetime of 11.4 ns for free 2AP, but no consideration was given to the effect of the buffer on the lifetime. Given that Rachofsky and colleagues[21] reported a decrease in lifetime at a similar buffer concentration, albeit with a different buffer system, this may have been a significant oversight. Although this does increase the likely uncertainty of the magnitude of their results, the observed trend of dynamic quenching efficiency (G > T > A > C) may still be correct, and is further supported by calculated free energy potentials. Charge transfer processes are dependent on the redox potentials of the donor and acceptor,

and the Weller equation relates the redox potentials of both donor and acceptor to the change in free energy due to charge transfer for a particular donor-acceptor pair. It is important to note that the direction of charge transfer doesn't appear to be the same for all the natural bases, however, comparison of the free energy change for charge transfer between excited state 2AP and the natural bases by Narayanan *et al*[22] was consistent with the quenching trend mentioned previously. In addition, this trend matches the observed trend of quenching efficiency for 2AP-containing dinucleotides.[13-18]

	k_q (σ) /10^9 M^{-1} s^{-1}	K_D (σ) /M^{-1}	K_S (σ) /M^{-1}
rGMP	2.52 (0.72)	28.66 (3.50)	1.43 (1.63)
rAMP	1.55 (0.42)	17.60 (1.45)	4.96 (0.99)
dTMP	1.71 (0.44)	19.41 (0.64)	2.21 (0.37)
rCMP	1.43 (0.41)	16.20 (2.01)	0.16 (1.16)

Table 4.2: Quenching rate constants (k_q), dynamic (K_D) and static (K_S) quenching constants for 2AP by the natural nucleotide monophosphates obtained from steady state fluorescence emission data. Table adapted from reference [22].

The more recent results by Narayanan *et al*[22] in Table 4.2 appear to better reflect the previously observed behaviour of 2AP fluorescence emission in the presence of DNA bases. However, these results relied on non-linear curve fitting to a finite set of steady-state fluorescence emission-derived data, which raises issues of overfitting. The effect of this can be seen in the relatively large standard deviations in Table 4.2, some of which are larger than the reported value. As noted previously, this could be due to correlation between parameters during the fitting process. Unlike the earlier work by Rachofsky *et al*,[21] no time-resolved fluorescence measurements were used to independently verify the accuracy of the reported dynamic quenching constants. These lifetime measurements would also have answered the question raised earlier of whether the reported unquenched lifetime used to calculate the quenching rate constants k_q was accurate, and therefore inspire more confidence in the reported quenching rate constants.

In this chapter, the focus will be on reproducing the measurements reported previously under identical solvent conditions using both steady-state and time-resolved fluorescence techniques. Fluorescence emission intensity measurements will be used to show the total quenching efficiency of the fluorescence of 2AP by the natural bases, while time-resolved measurements will be used to independently obtain

the static and dynamic quenching efficiencies. Statically quenched populations are typically considered non-fluorescent and therefore do not contribute to the observed fluorescence decays, although in the results reported here they do show up as short lifetime components. Regardless, the static and dynamic quenching processes can be separated using time-resolved fluorescence measurements. The results presented will be discussed further in the context of the previous reports already mentioned in order to gain an insight into the nature of the conflict between them, with the aim of resolving this dispute. Quenching of 2AP fluorescence due to inosine will also be presented in the context of the effect of redox potentials on charge transfer. Briefly, in principle a redox potential of zero between a donor-acceptor pair suggests charge transfer will not occur in any significant proportion, removing charge transfer as a non-radiative decay pathway.

4.2 Experimental Details

Adenosine (Sigma, 99%); Adenosine-5'-monophosphate disodium salt (Sigma, 99%); 2-aminopurine (Sigma, 99%); 2-aminopurine riboside (Carbosynth); Cytidine (Aldrich, 99%); Cytidine-5'-monophosphate disodium salt (Sigma, 99%); Deoxythymidine-5'-monophosphate disodium salt (Abcam, 98%); Ethylenediaminetetraacetic acid (Calbiochem); Guanosine (Sigma, 98%); Guanosine-5'-monophosphate disodium salt (Acros Organics, 97%); Inosine-5'-monophosphate disodium salt (Acros Organics, 97%); Potassium phosphate dibasic (Acros Organics, 98%); Potassium phosphate monobasic (Sigma, 99%); Sodium Chloride (Fisher, 99.5%); Thymidine (Sigma, 99%); Tris-hydrochloride (Fisher, 1M); Water (Fisher, HPLC grade) were all used as received without further purification.

Phosphate buffer (100 mM, pH 7.5), prepared from potassium phosphate monobasic (0.837 ± 0.002 g) and potassium phosphate dibasic (0.671 ± 0.002 g) in water (100 ± 0.5 mL), and tris-HCl buffer (20 mM tris-HCl, pH 7.5, 60 mM NaCl, 0.1 mM EDTA) were used separately to perform Stern-Volmer quenching measurements. Sample solutions of 2AP or r2AP (~ 10 μM) were prepared either in phosphate buffer or tris-HCl buffer solution. Ribosides or monophosphate nucleotides of each individual base were added at concentrations from 0 to 50 mM. Steady-state fluorescence spectra were collected using an excitation wavelength of 325 nm over emission wavelengths 330-550 nm. Time-resolved fluorescence measurements were

carried out using an excitation wavelength of 310 nm and emission wavelength at 380 nm with 10 nm bandwidth. Absorbance spectra between 200 and 400 nm were obtained to calculate sample concentrations.

4.3 Results

4.3.1 Steady-state fluorescence measurements

4.3.1.1 Phosphate buffer

The dependence of steady-state fluorescence intensity of 2AP on the concentration of each of the natural nucleotides, together with inosine, in phosphate buffer (0.1 M) are shown in Figure 4.3. The data shown were first fitted linearly following equation 2.11 to obtain K_{SV} from the gradient. Quenching constants K_D and K_S were then obtained from fitting of the data in Figure 4.3 with equation 2.18 and are shown in Table 4.3. The values of the intercepts in each case were within a few percent of unity, as expected from the modified Stern-Volmer equation (equation 2.18).

Results shown in Table 4.3 are not wholly consistent with those reported by Narayanan *et al*[22] (Table 4.2) using the same buffer, in particular for rCMP, likely as a result of overfitting, and rAMP, which appears to exhibit increased dynamic quenching but reduced static quenching in the present work. The authors quote a static quenching constant for rCMP close to zero, which suggests a linear fit using equation 2.11 would be more appropriate, giving a K_{SV} value closer to that previously reported for dynamic quenching. The values presented in this section for quenching by rCMP and rAMP were an early indication of an inherent problem with the use of equation 2.18 (modified Stern-Volmer equation) to obtain dynamic and static quenching constants simultaneously, namely substantial correlation between parameters, using steady state fluorescence measurements alone.

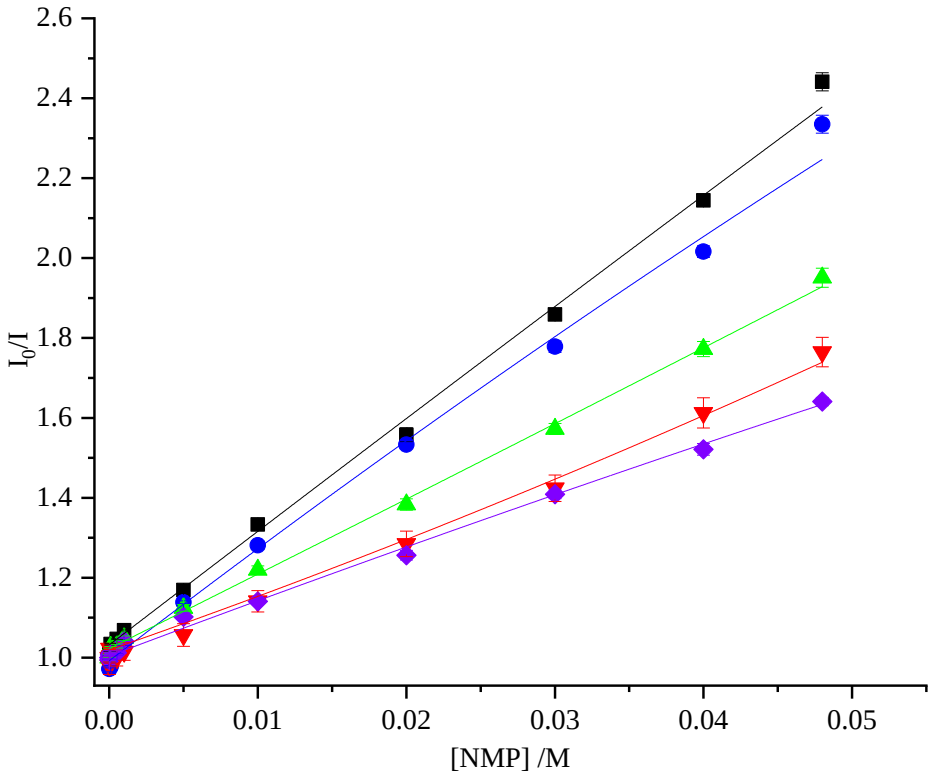

Figure 4.3: Stern-Volmer plot showing the dependency of 2AP fluorescence intensity on the concentration of each of the natural nucleotides and inosine monophosphate in 0.1 M phosphate buffer (pH 7). Graphs plotted: GMP (black squares), AMP (blue circles), dTMP (green triangles), CMP (red triangles), IMP (purple diamonds). Data fitted to equation 2.18

	K_{SV} (σ)[a] /M^{-1}	K_D (σ)[b] /M^{-1}	K_S (σ)[b] /M^{-1}
rGMP	30.20 (0.32)	28.43 (2.27)	0.81 (1.07)
rAMP	26.39 (0.32)	26.53 (2.30)	0 (1.05)
dTMP	18.66 (0.19)	18.96 (1.54)	0 (0.83)
rCMP	15.31 (0.23)	9.26 (3.97)	4.29 (3.35)
rIMP	12.74 (0.23)	14.85 (1.95)	0 (1.11)

Table 4.3: Stern-Volmer constants (K_{SV}), dynamic (K_D) and static (K_S) quenching constants for 2AP in phosphate buffer (0.1 M) in the presence of the natural nucleotide monophosphates, obtained from steady state fluorescence emission measurements. Obtained from fitting to (a) equation 2.11 (b) equation 2.18, with R^2 values >0.99 for each fit.

The validity of the use of the non-linear equation 2.18 is further questioned by equally good fits being obtained from linear fitting of the data. K_{SV} values similar to the K_D values were also found, the exceptions being rIMP (12.77 M^{-1}) and the aforementioned rCMP. These results imply that using equation 2.18 results in overfitting, with substantial correlation of the parameters. Quoted values of zero in Table 4.3 indicate that a result less than zero was obtained from the fitting. The algorithm used for polynomial curve fitting clearly does not prohibit solutions that aren't physically sensible, and suggests that the two parameters obtained from equation 2.18 show some degree of correlation. Overall, it appears that using equation 2.18 cannot be justified for this set of data alone. From the total quenching of 2AP fluorescence represented by the K_{SV} values in Table 4.3, the trend rGMP > rAMP > dTMP > rCMP appears.

4.3.1.2 Tris-HCl buffer

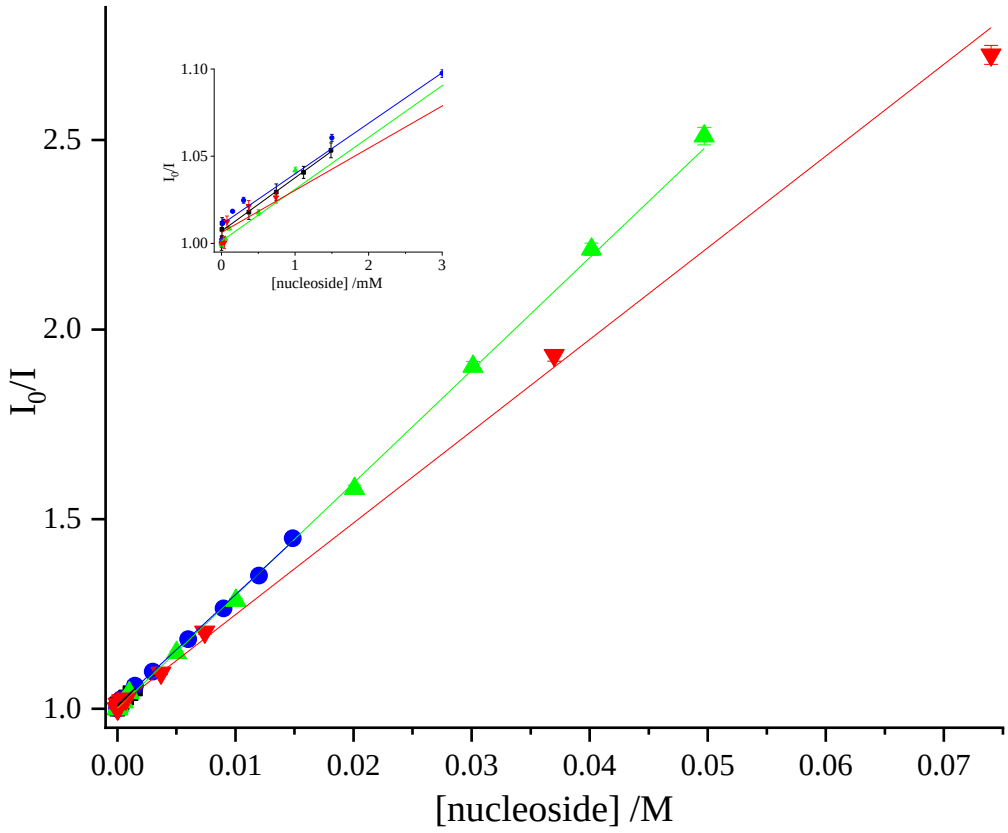

Figure 4.4: Stern-Volmer plot showing the dependency of r2AP fluorescence intensity on the concentration of the natural nucleosides in tris-HCl buffer (20 mM). Graphs plotted: rG (black squares), rA (blue circles), rT (green triangles), rC (red triangles). Inset: subset of same graph on mM scale.

	K_{SV} (σ)[a] /M^{-1}	K_D (σ)[b] /M^{-1}	K_S (σ)[b] /M^{-1}
rG	31.95 (2.44)	c	c
rA	29.04 (0.37)	23.50 (7.08)	4.24 (5.70)
rT	30.16 (0.19)	26.79 (0.76)	1.55 (0.37)
rC	23.48 (0.33)	28.58 (0.49)	0 (0.14)

Table 4.4: Stern-Volmer (K_{SV}), dynamic (K_D) and static (K_{SV}) quenching constants for r2AP in the presence of DNA bases using tris-HCl buffer (20 mM). Values obtained from fitting to (a) equation 2.11 (b) equation 2.18. (c) Values not determined due to limited solubility of. All R^2 values >0.99, with the exception of rG (0.95).

Repeating the Stern-Volmer measurements of r2AP using the nucleosides in tris buffer (20 mM), as reported by Rachofsky *et al*,[21] the data in Figure 4.4 were obtained, leading to the quenching constants in Table 4.4. The range of concentrations fitted was restricted, to minimise the effect of aggregation and the inner filter effect due to the nucleoside quencher in the results shown. As previously, a linear fit to equation 2.11 was used to obtain K_{SV}, while a polynomial fit to equation 2.18 was used to obtain K_D & K_S for rA, rT and rC. Reduced solubility of rG (an order of magnitude lower than the other bases) required it to be treated differently. The maximum rG concentration achieved was 1.8 x 10^{-3} M, which is only slightly above the concentration threshold where static quenching appears (see the following section on time-resolved measurements). Given that, once again, there was no clear improvement in the fit when using equation 2.18, the reasonable conclusion appears to be that K_{SV}, as a measure of the total 2AP fluorescence quenching, is the only result that can be obtained from this set of data. Consequently, rA and rT have very similar quenching efficiency, with the full trend rG > rA, rT > rC.

Using the same tris-HCl buffer system to measure the quenching of 2AP by the nucleotide monophosphates, rather than the nucleosides, gave the graphs in Figure 4.5. The quenching constants in Table 4.5 were obtained from fitting of this data as before; these are noticeably larger than the corresponding values in either of the earlier datasets. Based on the goodnes of fit, using equation 2.14 is unjustifiable. From the K_{SV} values in Table 4.5 obtained by linear fitting, the trend rGMP > rAMP > dTMP > rCMP can be seen.

Examining the errors for all the results presented in this section, it is immediately apparent that the errors are quite large and, in some cases, larger than the corresponding value. This is clearly far from satisfactory. Additionally, there are problems with fitting a polynomial curve to a relatively small dataset. Attempting to

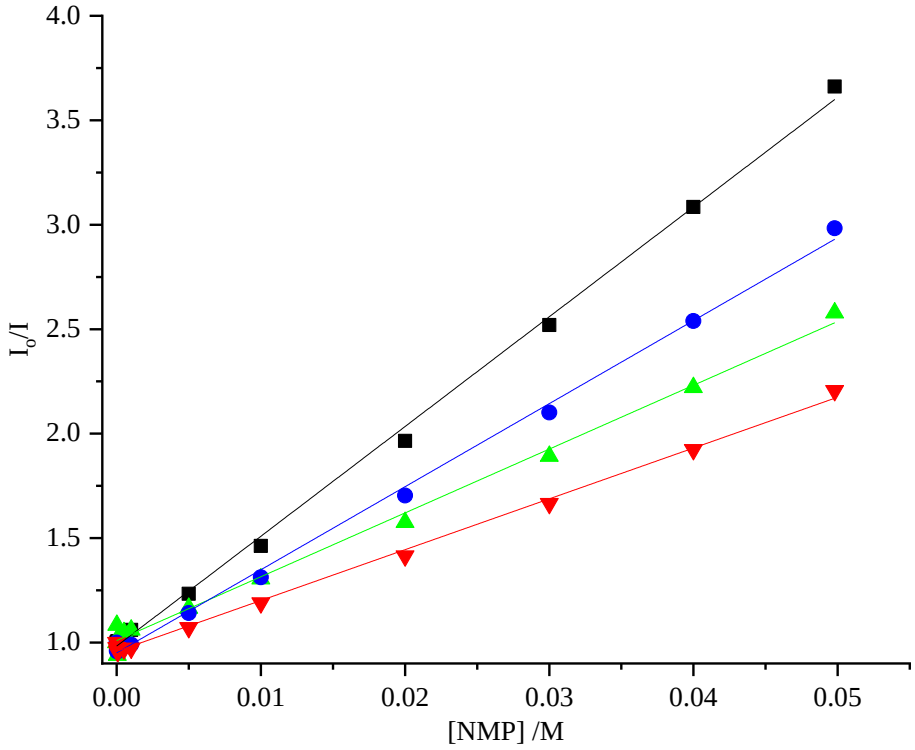

Figure 4.5: Stern-Volmer plots of the dependence of 2AP fluorescence intensity on the concentration of the natural monophosphate nucleotides in tris buffer (20 mM). Graphs plotted: rGMP (black squares), rAMP (blue circles), dTMP (green triangles), rCMP (red triangles).

	K_{SV} (σ)[a] /M^{-1}	K_D (σ)[b] /M^{-1}	K_S (σ)[b] /M^{-1}
rGMP	52.53 (0.65)	41.34 (0.81)	3.98 (0.34)
rAMP	39.75 (0.55)	29.57 (1.68)	4.44 (0.87)
dTMP	34.33 (0.68)	26.12 (4.97)	4.02 (2.80)
rCMP	24.33 (0.39)	15.36 (3.25)	5.36 (2.39)

Table 4.5: Stern-Volmer (K_{SV}), dynamic (K_D) and static (K_{SV}) quenching constants for 2AP in the presence of DNA bases using tris-HCl buffer (20 mM). Values obtained from fitting to (a) equation 2.11 (b) equation 2.18. R^2 values of >0.99 were obtained for each fit.

find a linearised version of equation 2.18, however, runs into separate problems. In particular, this approach assumes a significant static quenching contribution for the overwhelming majority of data points, which renders most of the concentration range presented here invalid for this process. As a consequence, higher concentrations are required, which is problematic due to quencher solubility and formation of aggregates, particularly for rGMP.

4.3.2 Time-resolved fluorescence measurements

4.3.2.1 Phosphate buffer

In order to obtain the dynamic quenching constant independently from the static quenching constant, time-resolved fluorescence measurements were performed. As discussed in the introduction to this chapter, static and dynamic quenching can be calculated separately using time-resolved fluorescence data. This provides a solution to the shortcomings outlined earlier, particularly as a linear fit can be applied to the time-resolved data. It soon became apparent that the fluorescence lifetime of 2AP in phosphate buffer (0.1 M) was much shorter than expected (~5.7 ns). After ruling out contamination, the lifetime of 2AP in phosphate buffer, up to 0.1 M, was measured as shown in Table 4.6, with mono-exponential decays fitted at all concentrations of phosphate buffer. This, combined with the consistent decrease in fluorescence lifetime with increasing phosphate concentration, is indicative of collisional quenching, without any ground state interactions or static quenching. Although 2AP has previously been shown to have two lifetime components in water, these components are sufficiently similar that global analysis of decays at several emission wavelengths is required to resolve them.

[Phosphate] /mM	Lifetime /ns
0	12.00
1	11.89
2	11.77
4	11.50
6	11.12
8	10.87
10	10.61
20	9.52
40	7.99
60	6.89
80	6.10
100	5.52

Table 4.6: Fluorescence lifetimes of 2AP in water as a function of phosphate buffer concentration. A single exponential decay was fitted in all cases.

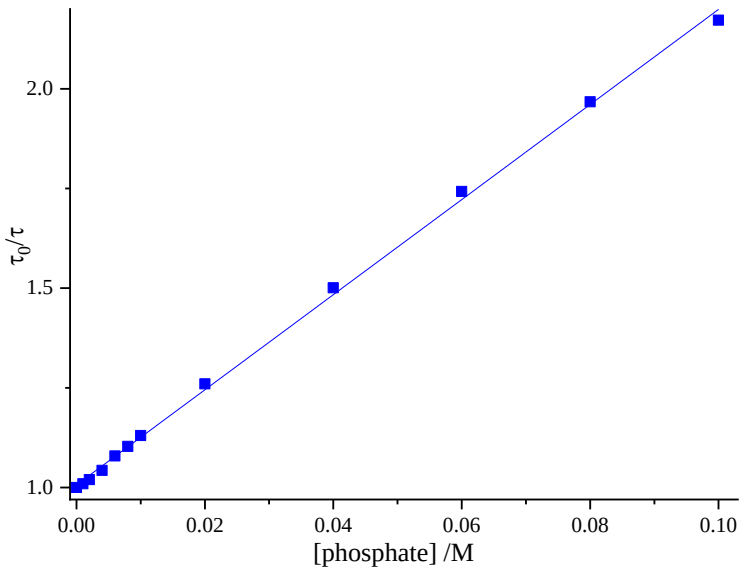

Figure 4.6: Stern-Volmer plot of 2AP fluorescence lifetime in water as a function of phosphate ions concentration. The fit had an R^2 value of 0.999 and 1.01 for the intercept.

Fitting these data to equation 2.11, as shown in Figure 4.6, yielded K_D = 11.92±0.13 M^{-1} and k_q = (1.00±0.01) x 10^9 M^{-1} s^{-1}, confirming that the shortened lifetime is a result of collisional quenching by the buffer. This finding only became obvious after time-resolved measurements were carried out, which may explain why this was not discussed by Narayanan *et al*.[22] Phosphate anions have previously been reported to have a similar effect on the fluorescence of tryptophan and tyrosine.[23-25] Fluorescence lifetimes of 2AP in phosphate buffer (0.1 M) in the presence of the nucleotide monophosphates are shown in Table 4.7 and discussed below. Fluorescence decay curves at low concentrations of NMP were fitted to a single exponential function, while at higher concentrations three lifetime components were fitted using global analysis and linking the two shortest components. The distinction was made based on the χ^2 value and the residuals from the individual fitting of each decay curve, as shown in Chapter 3. Where multiple lifetime components were fitted in Table 4.8, the relevant A-factors were corrected for scattered light, due to the higher concentration of NMP causing enhanced light scattering. This was achieved by plotting the inverse of the original A_1 values ($1/A_1$) as a function of NMP concentration and obtaining the intercept from a linear fit. Under ideal circumstances the intercepts would be close to unity, but in this case were noticeably larger (around 1.1 to 1.4). The scattered light component A_0 was then calculated from the multiplicative inverse of the intercept, which was subtracted from unity. Subsequent subtraction of A_0 from A_3 then gave the corrected A_3 value and the remaining A-factors were re-normalised to give the corrected set of values. The corrected A-factors obtained in this way and their corresponding lifetimes of 2AP in the presence of rAMP are shown in Table 4.7 below.

Fluorescence lifetimes of 2AP in the presence of rAMP show a few trends. First, the two shortest lifetime components τ_2 and τ_3 are constant, over the concentration range of rAMP where they are observed. However, the longest lifetime component τ_1 decreases with increasing rAMP concentration. Similarly, the population of the longest lifetime component (A_1) decreased with quencher concentration above 5 mM, while the combined proportion of the shorter lifetime components (A_2 and A_3) increased. This is consistent with static quenching occurring above 5 mM concentration of rAMP, as a characteristic of static quenching is a ground state interaction between 2AP and rAMP, likely a dimer or complex formed due to

base stacking. Such a dimer would behave as a distinct species with a much shorter fluorescence lifetime, which makes it unlikely that collisional quenching could occur over this short timescale due to the limitations of diffusion. In other words, the lifetime of statically quenched species would be independent of the concentration of the quencher, observed as shorter lifetime components τ_2 and τ_3 which are constant. In contrast, the population of the statically quenched dimer would increase with rAMP, which is reflected in the increasing proportion of the shortest lifetime components (A_2 and A_3). As expected, the population of the longest lifetime component A_1 decreased with increasing concentration of rAMP as a consequence. One aspect left to address is the appearance of two short lifetime components, both of which have been attributed to static quenching. Normally, it would reasonable to expect that only one ground state interaction takes place, but DNA base stacking exhibits a complex energy surface, with plenty of close-lying energy minima.[9, 26] It is likely the intermediate lifetime represents an alternative base stacked conformation (or a family of similar conformations) that is less favourable to the static quenching interaction, and it might even be the case that there were more than two distinct dimer species in reality, but the data presented here wasn't sufficient to resolve them as separate lifetime components. In oligonucleotides, it is generally accepted that there are four separate

[rAMP] /M	τ_1 /ns	τ_2 /ns	τ_3 /ns	A_1	A_2	A_3	$\langle\tau\rangle$ /ns
0	5.71	-	-	1	-	-	5.71
$1x10^{-5}$	5.68	-	-	1	-	-	5.68
$5x10^{-5}$	5.64	-	-	1	-	-	5.64
$1x10^{-4}$	5.61	-	-	1	-	-	5.61
$5x10^{-4}$	5.59	-	-	1	-	-	5.59
$1x10^{-3}$	5.54	-	-	1	-	-	5.54
$5x10^{-3}$	5.27	0.64	0.06	0.95	0.04	0.03	4.02
0.01	4.98	0.64	0.06	0.93	0.06	0.01	3.73
0.02	4.53	0.64	0.06	0.88	0.10	0.02	3.23
0.03	4.18	0.64	0.06	0.82	0.14	0.04	2.78
0.04	3.88	0.64	0.06	0.76	0.16	0.08	2.40
0.05	3.64	0.64	0.06	0.72	0.19	0.09	2.17

Table 4.7: Fluorescence lifetimes of 2AP as a function of rAMP concentration in phosphate buffer (0.1 M). A-factors corrected for scattered light.

lifetime components for 2AP,[1] which likely represent separate conformations or families of conformations, and that is with the extra constraint of the sugar-phosphate backbone. It is not surprising, therefore, that multiple short lifetime components are observed in the data presented here.

Similar behaviour is shown by 2AP in the presence of dTMP (Table 4.8), namely that mono-exponential decay is observed with concentrations of dTMP below 5 mM, while concentrations of dTMP at 5 mM or above displays 3 lifetime components in the fluorescence emission of 2AP. As before, the population of the longest lifetime component A_1 steadily decreases with increasing dTMP concentration, relative to the shorter lifetime components, with the exception of the outlier at 5 mM dTMP concentration. It isn't completely clear why there is an outlier, however, the fact that the outlier sits at the edge of a 'transition zone' between single exponential decay and multi-exponential decay is likely quite important. A-factors from the time-resolved data at dTMP concentration of 5 mM suggest that three lifetime components might not be justified. Working on the assumption that there are only 2 lifetime components at this concentration, re-normalising A_1 and A_2 gives 0.99 and 0.01, respectively, which is more consistent with the trend seen in the rest of the data at higher dTMP concentrations. Performing a separate fitting of the same data with two components and fixing the relevant lifetimes to the values shown in Table 4.8, gives reasonably consistent A-factors of 0.98 and 0.02 for A_1 and A_2, respectively. Obtaining values that are more consistent with the trend when only two lifetime components are assumed for a concentration of dTMP of 5mM, and an A-factor of zero when the concentration of dTMP is 10 mM, suggests that there aren't three real lifetime components in the fluorescence decay of 2AP for these concentrations of dTMP. Alternatively, the data obtained from the experimental setup used to collect this data may not be good enough to properly resolve the two shortest lifetime components when they form a very low proportion of the total emitting population. This is a particular issue for the shortest lifetime component, which is at the limit of detection for the system described in Chapter 3. Repeating the procedures described below in this section with the alternative values for dTMP at 5mM concentration gives similar results to those shown further on. The trends of decreases in the fluorescence lifetime and proportional population of the long lifetime component, simultaneous with the increase in population of the shorter lifetime components, were also seen for

2AP time-resolved fluorescence data in the presence of the remaining natural bases and inosine, which are shown in Appendix I.

[dTMP] /M	τ_1 /ns	τ_2 /ns	τ_3 /ns	A_1	A_2	A_3	$\langle\tau\rangle$ /ns
0	5.60	-	-	1	-	-	5.60
$1x10^{-5}$	5.68	-	-	1	-	-	5.68
$5x10^{-5}$	5.65	-	-	1	-	-	5.65
$1x10^{-4}$	5.63	-	-	1	-	-	5.63
$5x10^{-4}$	5.58	-	-	1	-	-	5.58
$1x10^{-3}$	5.54	-	-	1	-	-	5.54
$5x10^{-3}$	5.25	0.51	0.03	0.95 (0.98)[a]	0.01 (0.02)[a]	0.04 (0)[a]	4.99 (5.16)[a]
0.01	4.93	0.51	0.03	0.98	0.02	0	4.84
0.02	4.39	0.51	0.03	0.88	0.02	0.10	3.88
0.03	3.96	0.51	0.03	0.83	0.03	0.13	3.31
0.04	3.61	0.51	0.03	0.79	0.04	0.17	2.88
0.05	3.32	0.51	0.03	0.78	0.04	0.18	2.62

Table 4.8: Fluorescence lifetimes of 2AP as a function of dTMP concentration in phosphate buffer (0.1 M). A-factors were corrected for scattered light. (a) A-factors and number-averaged lifetime from refitting with two lifetime components, fixing the fluorescence lifetimes to the corresponding values shown in the table.

Stern-Volmer plots using the longest lifetime component τ_1 measured in phosphate buffer (0.1 M) are shown in Figure 4.7. These values were fitted to equation 2.11 in a similar fashion to that described earlier to obtain the K_D values, which were then fixed during an alternative fitting of the steady-state data using equation 2.18, which results in the data shown in Table 4.9. Fitted lifetime data for 2AP in the presence of rGMP was restricted to rGMP concentrations ≤ 0.02 M, due to a clearly observable increase in viscosity at higher concentrations. This was attributed to the formation of G-quadruplexes,[27] a form of self-aggregation unique to guanine. Comparing the dynamic quenching constants obtained in Table 4.9 gives the trend rGMP ~ dTMP > rAMP ~ rCMP >> rIMP. In addition, the dynamic quenching of rGMP doesn't appear to be an outlier as it is for the steady-state data. An important result is the noticeable increase in the corresponding quenching rate constants k_q reported here compared to those reported previously,[22] with the exception of rGMP, despite lower dynamic quenching constants being observed in this study. This is due to the value of τ_0 in phosphate buffer

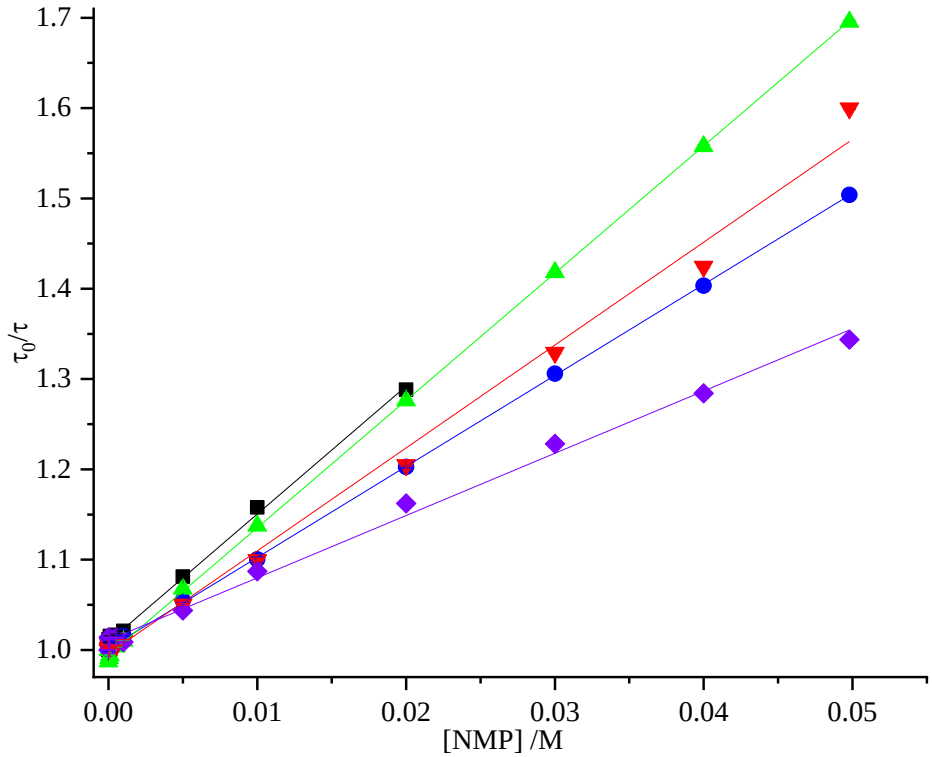

Figure 4.7: Stern-Volmer plot of 2AP fluorescence lifetime in phosphate buffer (0.1 M) as a function of concentration of nucleotide monophosphate. Plotted: rGMP (black squares), rAMP (blue circles), dTMP (red triangles), rCMP (green triangles), rIMP (purple diamonds).

	K_D (σ) /M^{-1}	K_S (σ) /M^{-1}	k_q (σ) /10^9 M^{-1} s^{-1}
rGMP	14.15 (0.27)	8.52 (0.30)	2.48 (0.05)
rAMP	11.37 (0.20)	9.93 (0.37)	1.99 (0.03)
dTMP	14.23 (0.11)	2.69 (0.15)	2.48 (0.03)
rCMP	11.60 (0.12)	2.31 (0.14)	2.06 (0.04)
rIMP	6.90 (0.14)	4.45 (0.22)	1.21 (0.02)

Table 4.9: Stern-Volmer (K_{SV}), dynamic (K_D) and static (K_S) quenching constants for 2AP in the presence of the nucleotides using both time-resolved and steady state data. A lifetime of 5.7 ns was used to calculate k_q, as this was the average lifetime measured for 2AP (absent quencher) in phosphate buffer (0.1 M). R^2 values >0.99 were obtained for each fit.

(0.1 M), which is approximately half that for 2AP in unbuffered water. Narayanan *et al* did not seem to be aware of the correct lifetime.

Examining the observed static quenching constants K_S obtained from fixing the K_D values in a separate fitting of equation 2.18 to the steady-state fluorescence data, the trend rAMP ~ rGMP > rIMP > dTMP ~ rCMP is found. The K_S values in Table 4.9 are derived from the fluorescence emission intensity which encapsulates information from the entire static quenching process, including both the propensity to form a stacked complex and the enhanced quenching that occurs within that complex. The trend in Table 4.9 therefore likely represents the overall effect of static quenching on the quantum yield.

An alternative way to obtain the static quenching constant is possible using equation 2.13 with the time-resolved data. Plotting $1/A_1$ using the corrected A_1 values (shown in Appendix I) allows the static quenching constant to be obtained from the gradient, shown in Table 4.10 below. This method is based on the assumption that all of the lifetime components besides the longest component, are due to static quenching. Such an assumption is likely quite reasonable, as the quenching rate constant of the dynamic (collisional) quenching is already close to the diffusion limit and there is an order of magnitude difference between the longest lifetime component and remaining components, strongly suggesting that the shorter lifetime components must be due to ground-state interactions between 2AP and the natural bases. There are clear discrepancies between the static quenching constants presented in Table 4.10 from time-resolved measurements and in Table 4.9 from steady-state measurements.

It seems likely that this discrepancy is a consequence of the different techniques used to calculate K_S values, particularly in the case of steady-state measurements where the assumption that intensity is proportional to quantum yield. However, this is only true when the absorbance of the fluorophore under investigation remains low (< 1) for each measurement compared. The fluorescence intensity is also highly sensitive to a number of factors, including fluctuations in the intensity of the light source and fluorophore concentrations between samples, which are minimised under the experimental conditions described earlier by careful sample preparation and applying a correction to spectra using the measured lamp intensity during each measurement. Putting aside such factors, there are additional issues specific to the

system studied in this work, in particular any shift in the absorbance profile due to the formation of the new dimer species at higher concentrations of NMP. Due to the very high concentration of natural base relative to 2AP (which also affect fluorescence intensity due to non-negligible absorbance at the excitation wavelength, leading to an inner filter effect), a longer excitation wavelength of 325 nm is used. At this wavelength, the gradient of the spectral profile will result in a significant change in absorbance for even relatively small wavelength shifts. In contrast, fluorescence lifetimes are proportional to quantum yield and are not affected by changes in fluorescence intensity, unless those changes are due to real changes in quantum yield. Notwithstanding the difference in magnitude between the values in Table 4.9 & Table 4.10, the pattern followed is essentially the same. The trend for static quenching based purely on time-resolved fluorescence data is likely similar to that shown in Table 4.9, although the data series in Table 4.10 is incomplete for the reasons discussed earlier. Overall, taking into account both static and dynamic quenching, the trend for the DNA base quenchers used seems to be rGMP > rAMP ~ dTMP > rCMP > rIMP.

K_S (σ) /M^{-1}		
	$1/A_1$	$\tau_0/\langle\tau\rangle$
rGMP	a	a
rAMP	7.46 (0.33)	6.44 (0.20)
dTMP	5.92 (0.80)	5.95 (0.22)
rCMP	5.89 (0.54)	5.05 (0.94)
rIMP	6.04 (0.37)	7.11 (0.7)

Table 4.10: Static quenching constants K_S for NMP quenching of 2AP in phosphate buffer (0.1 M), obtained using A-factor of long lifetime component and number-averaged lifetime from time-resolved fluorescence decay measurements. (a) Reliable fit could not be obtained due to signs of aggregation.

4.3.2.2 Tris-HCl buffer

Fluorescence lifetimes of 2AP riboside (r2AP) in the presence of thymidine riboside are shown below in Table 4.11, where much of the same behaviour discussed earlier can be seen. In particular, the same 'threshold concentration' property of the natural base quencher applies, above which more complicated multi-exponential fluorescence decay was observed. In the results presented in Table 4.11 below, the threshold concentration appears to be slightly less, although the shortest lifetime component (A_3) does not appear in any significant proportion until the concentration

[rT] /M	τ_1 /ns	τ_2 /ns	τ_3 /ns	A_1	A_2	A_3	$<\tau>$ /ns
0	10.39	-	-	1	-	-	10.39
$7.50x10^{-6}$	10.42	-	-	1	-	-	10.42
$3.75x10^{-5}$	10.38	-	-	1	-	-	10.38
$7.50x10^{-5}$	10.36	-	-	1	-	-	10.36
$3.75x10^{-4}$	10.29	-	-	1	-	-	10.29
$7.50x10^{-4}$	10.21	2.09	0.08	0.98	0.02	0	10.02
$3.75x10^{-3}$	9.57	2.09	0.08	0.97	0.03	0.00	9.36
$7.50x10^{-3}$	8.87	2.09	0.08	0.97	0.03	0	8.67
0.015	7.77	2.09	0.08	0.93	0.04	0.04	7.28
0.023	6.93	2.09	0.08	0.93	0.05	0.02	6.55
0.030	6.25	2.09	0.08	0.90	0.05	0.05	5.74
0.037	5.73	2.09	0.08	0.88	0.06	0.06	5.15

Table 4.11: Fluorescence lifetimes of r2AP as a function of rT concentration in tris-HCl buffer (20 mM). A-factors corrected for scattered light. A-factors presented as '0' represent cases where applying the scattered light correction gave a negative value.

[rG] /M	τ /ns
0	10.44
$3.45x10^{-7}$	10.41
$1.72x10^{-6}$	10.41
$3.44x10^{-6}$	10.40
$1.72x10^{-5}$	10.40
$3.45x10^{-5}$	10.38
$1.72x10^{-4}$	10.34
$3.45x10^{-4}$	10.29
$6.89x10^{-4}$	10.21
$1.0x10^{-3}$	10.11
$1.4x10^{-3}$	10.03
$1.7x10^{-3}$	9.96

Table 4.12: Fluorescence lifetimes of r2AP as a function of rG concentration in tris-HCl buffer (20 mM).

of rT exceeds 10 mM. Previously observed trends of the longest lifetime and the A-factors with rT concentration are also present in the data shown in Table 4.11, which was replicated in the data for the other riboside bases (rA and rC shown in Appendix I) with the exception of rG. One difference that does stand out for the conditions used in this section is the increased lifetimes for the shorter components τ_2 and τ_3 of r2AP, which was observed for the other natural bases as well, with the exception of rG where multiple fluorescence lifetimes were not observed for r2AP (Table 4.12). The other notable exception is rC, where the shortest fluorescence lifetime component τ_3 is consistent with those observed in the presence of the other natural bases, but the intermediate lifetime component τ_2 was shorter (0.51 ns), which is more consistent with the previous results for the monophosphate nucleotides (Table 4.7 & Table 4.8). This is interesting, as it implies that there were actually four lifetime components, but the data and the fitting algorithm were only capable of resolving three of them, with the lifetime appearing from the fitting dependent on which produces the better fit to the data. However, the concentration range used for rC was substantially higher than for the other ribosides, which may have given rise to the change in observed fluorescence lifetime components.

The effect of the presence of rG on the fluorescence lifetime of r2AP is shown in Table 4.12 above. In contrast to all the previous data sets, the transition to a more complicated multi-exponential decay of r2AP fluorescence was not observed for rG, but this is more likely to be as a result of the reduced concentration range studied due to lower solubility of rG compared to the other natural bases, rather than any fundamental property of fluorescence quenching of r2AP by guanine. It is important to note that there are a number of significant differences between the conditions employed to obtain the data in the current section and those for the data represented previously, namely the change in pH buffer and the use of the riboside derivative of 2AP (r2AP). r2AP has a single exponential fluorescence decay curve, while 2AP as a free base has two tautomers and two lifetime components, which can't be resolved using the data presented here.

The exact structure of the natural base quenchers used was also different, with the riboside derivatives used instead of the monophosphate nucleotides. However, the concentration range used was likely the most significant contributing factor, which will be discussed in more detail later. The fluorescence lifetimes of r2AP described

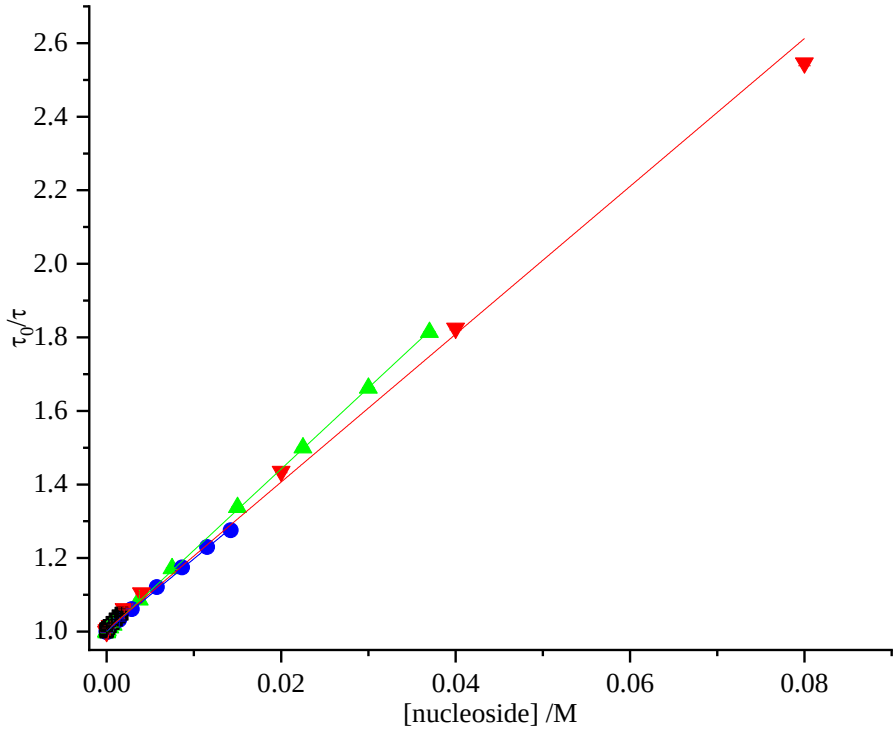

Figure 4.8: Stern-Volmer plot of fluorescence lifetimes of r2AP in tris-HCl buffer (20 mM) as a function of nucleoside concentration. Quenchers: rT (geen triangles), rA(blue circles), rC (red triangles), rG (black squares).

	K_D (σ) /M^{-1}	K_S (σ) /M^{-1}	k_q (σ) /10^9 M^{-1} s^{-1}
rG	27.23 (0.80)	3.99 (2.60)	2.62 (0.08)
rA	19.58 (0.19)	7.53 (0.29)	1.88 (0.02)
rT	22.04 (0.07)	4.09 (0.11)	2.12 (0.01)
rC	19.40 (0.28)	1.67 (0.23)	1.80 (0.02)

Table 4.13: Stern-Volmer (K_{SV}), dynamic (K_D) and static (K_S) quenching constants for r2AP in the presence of the nucleosides in tris-HCl buffer (20 mM). A lifetime of 10.4 ns was used to calculate the quenching rate constant k_q.

K_S (σ) /M^{-1}		
	$1/A_1$	$\tau_0/\langle\tau\rangle$
rA	8.57 (0.25)	7.87 (0.22)
rT	3.16 (0.31)	2.90 (0.17)
rC	40.79 (0.81)	29.70 (0.82)

Table 4.14: Static quenching constants of r2AP fluorescence by the nucleoside bases in Tris-HCl buffer (20 mM), using the A-factors and number-averaged lifetimes obtained from fluorescence decay measurements.

above in the presence of the ribosides of the natural bases in tris-HCl buffer (20 mM) were used to derive the Stern-Volmer quenching data, shown in Figure 4.8, to which a linear fit was applied. Dynamic quenching constants in Table 4.13 were derived from the gradient, according to equation 2.11. Static quenching values were obtained by fixing the dynamic quenching constants in a separate fitting of the steady-state fluorescence data. It is immediately apparent that the dynamic quenching constants follow the trend rG > rT > rA ~ rC. Although rG was fitted to the modified Stern Volmer equation, the static quenching observed is essentially negligible. However, the lower solubility of rG limits the maximum concentration to the order of 10^{-3} M. This is the same concentration at which extra components start to appear in the fluorescence decay curves, which in this work is attributed to ground state interactions, i.e. static quenching. These extra components only appear at concentrations of 10^{-3} M or higher, regardless of base identity or buffer system used as demonstrated in Table 4.8 and the full set of time-resolved fluorescence data in Appendix I. This pattern of static quenching only being observed at or above concentrations on the order of 1 mM is consistent across all data used in this chapter. For this reason, it is highly likely that the small static quenching constant observed for rG is a consequence of the concentration range, and not the ability of rG to form ground state complexes with 2AP. For bases other than rG, static quenching values in Table 4.13 follow the trend rA > rT > rC.

Using the A-factors from the fitting of the fluorescence decays as before, the corrected A-factors of the longest lifetime component gave the K_S values in Table 4.14 above. The value for rG is not included for the reasons mentioned previously, fitting more than one lifetime component could not be justified in terms of the χ^2 parameter or the pattern of residuals, which supports the lack of static quenching over the concentration range used. Comparing the shortest 2AP fluorescence lifetimes as described earlier, the trend rT > rA ~ rC is found for the non-radiative decay rate, however the trend is incomplete and is not consistent with the data shown elsewhere in this chapter, particularly with regards to rC. It isn't immediately clear why the value for rC is so much greater than the others, but a possible explanation comes from the range of concentrations used, which is much broader for rC than for the other nucleosides due to its higher solubility. Although an excitation wavelength of 310 nm was used, which is substantially removed from the peak wavelength of the main rC

absorption band, the much greater concentration range (compared to all other measurements in this chapter) and the use of a laser excitation source makes it possibly that rC molecules were also excited. The excitation wavelength used for the steady-state measurements was also further from the peak of rC's absorption band. It is known that cytosine undergoes some photochemistry, including photohydration and formation of dimers,[28] so there may be additional interactions between r2AP and rC which distorts the observed static quenching. This can be seen in the measurements shown here by comparing the A-factors of the long lifetime component between rC and the other natural bases. From Table 4.15, it can be seen that the proportion of the long lifetime component is markedly lower for rC than for rA at similar concentrations. A similar qualitative difference can be seen between rC and the other bases.

[rC] /mM	A_1	[rA]	A_1
2.0	0.886	2.9	0.969
4.0	0.841	5.8	0.948
20.0	0.556	14.2	0.885

Table 4.15: Population of long-lifetime component A_1 of 2AP fluorescence decay in the presence of the riboside DNA bases.

Fluorescence decay of 2AP in the presence of the monophosphate nucleotides were also measured using the same buffer system, with the resulting lifetimes in the presence of dTMP shown in Table 4.8 below. Once again, a decreasing trend for the lifetime (τ_1) and A-factor (A_1) of the longest lifetime component is seen in the presence of dTMP as well as the other natural NMP (). The A-factors are also similar at a given concentration of NMP, regardless of the identity of the base, which has implications for static quenching which will be discussed further later. Shorter lifetimes observed at higher concentrations of NMP were also similar in magnitude across all bases. As a consequence, the number-averaged fluorescence lifetimes $<\tau>$ also followed a similar trend, regardless of the identity of the base quencher, although the magnitude varied enough to yield the noticeably different k_q values.

Fluorescence quenching of 2AP by the nucleotide monophosphates in tris buffer (20 mM) are shown in Figure 4.9. As before, K_D and k_q values in Table 4.17 were obtained using equation 2.11. The dynamic quenching follows the pattern dTMP > rGMP >> rAMP > rCMP. In contrast, static quenching for the nucleotide

[dTMP] /M	τ_1 /ns	τ_2 /ns	τ_3 /ns	A_1	A_2	A_3	$<\tau>$ /ns
0	11.95	-	-	1	-	-	11.95
$1x10^{-5}$	11.91	-	-	1	-	-	11.91
$5x10^{-5}$	11.87	-	-	1	-	-	11.87
$1x10^{-4}$	11.83	-	-	1	-	-	11.83
$5x10^{-4}$	11.72	-	-	1	-	-	11.72
$1x10^{-3}$	11.57	-	-	1	-	-	11.57
$5x10^{-3}$	10.54	2.65	0.06	0.95	0.02	0.02	10.07
0.01	9.45	2.65	0.06	0.95	0.03	0.02	9.06
0.02	7.81	2.65	0.06	0.85	0.04	0.11	6.75
0.03	6.65	2.65	0.06	0.82	0.05	0.14	5.59
0.04	5.79	2.65	0.06	0.81	0.06	0.14	4.86
0.05	5.14	2.65	0.06	0.72	0.07	0.21	3.90

Table 4.16: Fluorescence lifetimes of 2AP as a function of dTMP concentration in tris-HCl buffer (20 mM). A-factors were corrected for scattered light.

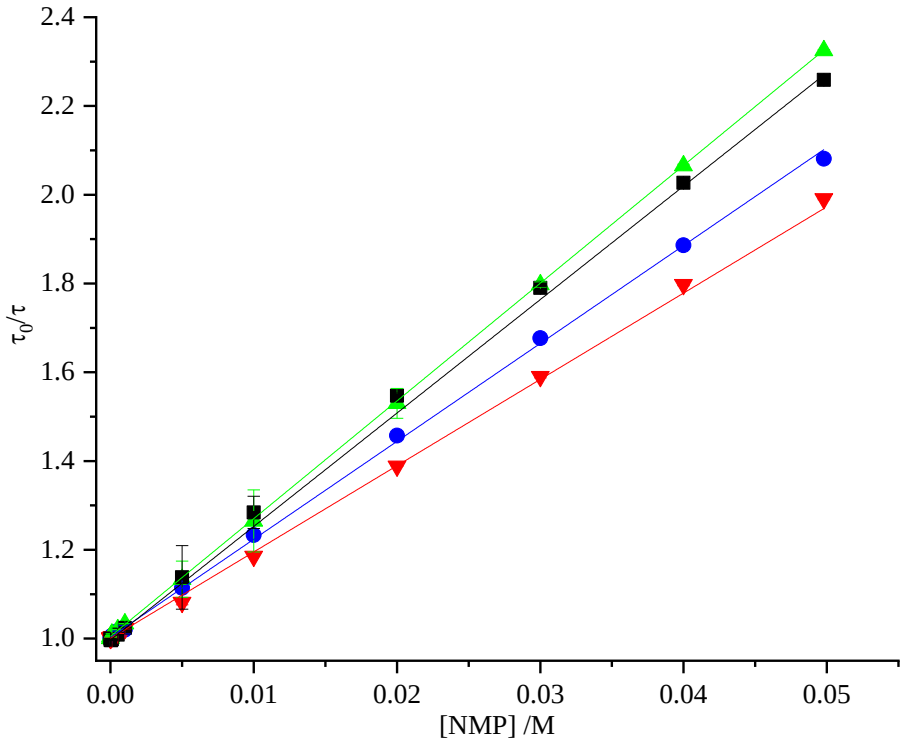

Figure 4.9: Stern-Volmer plot of 2AP fluorescence lifetime in tris-HCl buffer (20 mM) as a function of nucleotide monophosphate concentration. Quenchers: rAMP (blue circles), rCMP (red triangles), dTMP (green trinagles), rGMP (black squares).

	K_D (σ) /M^{-1}	K_S (σ) /M^{-1}	k_q (σ) /10^9 M^{-1} s^{-1}
rGMP	25.66 (0.28)	12.52 (0.29)	2.19 (0.02)
rAMP	21.90 (0.17)	9.02 (0.17)	1.88 (0.01)
dTMP	26.50 (0.05)	3.68 (0.32)	2.26 (0.01)
rCMP	19.84 (0.12)	2.43 (0.14)	1.70 (0.01)

Table 4.17: Stern-Volmer (K_{SV}), dynamic (K_D) and static (K_S) quenching constants for 2AP in the presence of DNA bases using tris-HCl buffer (20 mM). K_D values were obtained from fitting time-resolved data, K_S values from fixing K_D values when fitting steady-state data. An average lifetime of 11.7 ns for 2AP in tris-HCl buffer was used to calculate k_q.

monophosphates in tris buffer in Table 4.17 shows the trend rGMP > rAMP >> dTMP > rCMP. In the same manner described earlier, the static quenching shown in Table 4.18 was obtained independently from the A-factor of the longest lifetime component ($1/A_1$) and from fitting equation 2.18 to the number-averaged lifetime ($\tau_0/\langle\tau\rangle$). As for the earlier datasets, the A-factor of the longest lifetime was used to calculate K_S values for quenching of 2AP fluorescence by the natural monophosphates. Here, the static quenching trend previously obtained from fitting of the steady-state data disappears, or at least the differences between individual values in the same series are of a similar magnitude to the uncertainty. Therefore it appears that static quenching of 2AP fluorescence by the nucleotide monophosphates is essentially the same in Tris-HCl buffer. It is interesting to compare the static quenching values obtained from the different methods discussed above. There is better agreement between the values in Table 4.18 from the time-resolved data, than there is between Table 4.17 and Table 4.18. However, it should be noted that with the exception of the pyrimidines in Table 4.17, the variation in static quenching is much smaller than that observed for dynamic quenching. This is related to the observation about the A-factors noted earlier, where the A-factors observed at a given concentration don't substantially change with the identity of the quenching base. Since changes in the A-factor indicate a change in the static quenching taking place as a proportion of the total quenching, it logically follows that similar A-factors signify a similar proportion of static quenching. In addition, the most reliable values are likely those derived from A_1 shown in Table 4.18, as these are completely independent of the dynamic quenching constants obtained previously. In this set of values, the biggest variation appears to be between the purines and the pyrimidines, although it should be stressed that the difference is quite small, especially when the quoted error estimates are taken into account.

K_S (σ) /M^{-1}		
	$1/A_1$	$\tau_0/<\tau>$
rGMP	9.03 (0.83)	7.98 (0.20)
rAMP	9.64 (0.17)	7.62 (0.20)
dTMP	7.71 (0.53)	5.97 (0.31)
rCMP	8.79 (0.63)	7.49 (0.14)

Table 4.18: Static quenching constants of 2AP fluorescence by the natural monophosphate bases in Tris-HCl buffer (20 mM), obtained from corrected A-factors and number-averaged lifetimes in the time-resolved fluorescence data.

It is also important to bear in mind that there are crucial differences between the steady-state and time-resolved fluorescence quenching measurements. Using fluoresecence emission intensity to calculate quenching relies on the assumption that any changes in intensity are solely due to presence of the quencher. There are, unfortunately, many experimental parameters which have an effect on the emission intensity. Some of these are general to all fluorophores and can be controlled by precise experimental technique, such as producing a consistent fluorophore concentration and instrument parameters (especially bandwidth). Another, specific to the 2AP/natural base system discussed here, is the overlap of the edges of the 2AP and natural base absorption peaks. At low concentrations, the effect is negligible but the natural base concentration is increased to three or four orders of magnitude more than the concentration of 2AP. Shifting the excitation wavelength to 325 nm in the steady-state fluorescence measurements limits the absorption of the natural base, but there is still a significant inner-filter type effect. This issue is absent in time-resolved fluorescence measurements, as the quenching calculated from the fluorescence lifetime data was dependent on fluorescence lifetime and not emission intensity. Comparing the shorter fluorescence lifetimes of 2AP-base complexes, which represent information about the competition between the fluorescence emission and the non-radiative decay process (quenching), the trend rGMP ~ dTMP > rAMP ~ rCMP emerges for quenching of 2AP fluorescence within the complex with the natural bases. This trend is consistent with an electron transfer mechanism for the reasons previously described.

4.4 Discussion

The steady-state fluorescence measurements presented in the previous section suggest that a similar trend G > A > T > C in the quenching efficiency of 2AP

fluorescence by the natural bases is obtained. This occurs regardless of the buffer system or whether riboside bases or the monophosphate nucleotides are used as quenchers. However, this trend is based on total fluorescence quenching observed, via the K_{SV} values obtained, and does not say anything about the mechanism of fluorescence quenching, other than that it is dependent on the identity of the natural base quencher. As previously mentioned, using equation 2.18 to obtain values for static and dynamic quenching creates issues with correlation between these two parameters. Herein lies the first potential reason for the discrepancy between the two previous reports on fluorescence quenching of free 2AP in solution. Narayanan *et al*[22] presented values for both static and dynamic quenching based solely on steady-state fluorescence measurements, which raises questions about the accuracy of the magnitudes reported as already discussed. Although the authors did use an excitation wavelength of 325 nm, which is likely due to the very high concentrations of quencher used, and the limited spectral separation between 2AP and the DNA base quenchers.

In contrast, Rachofsky and colleagues[21] used both steady-state and time-resolved fluorescence techniques, but state that static quenching constants could not be resolved, although they also state that deviation from linearity was observed in the steady-state fluorescence derived data and thereby conclude that both static and dynamic quenching processes of 2AP fluorescence take place. This is somewhat confusing, but may be a product of the state of the field at the time, and will be discussed in more depth later. They also use an excitation wavelength of 309 nm, which may cause problems due to the inner-filter effect. Although the extinction coefficient of the natural bases is fairly small at 309 nm, it is not zero, and the concentrations used suggest that the absorbance at the excitation wavelength use may be significant, perhaps even larger than the 2AP absorbance at the highest natural base concentrations. This will result in a significant inner filter effect, something that is not taken into consideration, or even mentioned, by the authors. It is hard to be sure of the impact this will have had on their reported results, not least because only the quencher concentrations for dT are quoted, with a maximum of 272 mM. For thymine, using an excitation wavelength of 309 nm will result in decreased fluorescence intensity equivalent to quenching of ~7 M^{-1} in their steady-state measurements, although fluorescence lifetime measurements would likely be less affected.

Steady-state fluorescence intensity-derived results presented in this work show that total fluorescence quenching of free 2AP is overwhelming dependent on the base identity, and moreover that this trend is consistent with the quenching trend observed in single-strand dinucleotides, although the magnitudes vary under altered buffer conditions. Unfortunately, neither Narayanan *et al*[22] nor Rachofsky and co-workers[21] consider that fluorescence quenching of 2AP in DNA is due to combined static and dynamic quenching. Measuring static and dynamic quenching separately is useful and important, however doing so has limited use in isolation.

In order to untangle the question of the two different quenching mechanisms, and the presence or absence thereof, time-resolved fluorescence data was collected to resolve static and dynamic quenching separately. However, it was found during this process that the 0.1 M phosphate buffer significantly quenched the fluorescence of 2AP, with a fluorescence lifetime of approximately 5.7 ns in buffer against 11.4 ns in water. Two previously hidden complications are raised by this issue, the first is that extra quenching distinct to that due to the DNA bases occurs in the phosphate buffer system, and secondly that the quenching rate constants reported by Narayanan and co-workers, which are calculated using the fluorescent lifetime, cannot be relied upon to make a fair comparison between the two papers. Since K_D is dependent on the fluorescence lifetime, while the quenching rate constant k_q is not, it is more reliable to use k_q to compare quenching under different conditions, but this assumes that the k_q values reported are accurate. This also explains the differences in magnitude of the collisional quenching, both in the results reported here and in the literature,[21, 22] although not necessarily the different trends reported. Such extra uncertainty from the effect of the buffer is in addition to the issue of correlation between the parameters obtained from non-linear fitting.

The caveats already mentioned for the time-resolved fluorescence data presented in this chapter, namely the concentration effects due to the reduced solubility of the riboside bases, and the additional quenching effect of the phosphate buffer, mean that the most reliable set of data comes from the quenching by the nucleotide monophosphates in tris-HCl buffer. To illustrate this point, consider the quenching by guanine determined under all three conditions. The static quenching constant obtained for rG in tris-HCl buffer is substantially lower than the other two cases due to rG being the least soluble of all the ribosides (indeed, no static quenching at all could be derived

solely from time-resolved fluorescence measurements), while the dynamic quenching constant for GMP (and, in fact, for all of the other NMPs) is lower in phosphate buffer than it is in tris-HCl buffer, whether the riboside or the monophosphate is used as quencher. This is not to say that the first two time-resolved fluorescence datasets in 4.3.2.1 and for the riboside in 4.3.2.2 are irrelevant, but rather that some of the results reported therein are not necessarily solely due to the effect of the identity of the chosen quencher.

It is important to bear in mind that the trends reported here are only consistent when the total quenching, which consists of combined static and dynamic quenching, from the steady-state data is considered. Obtaining separate values for the static and dynamic quenching constants is more complicated, but was achieved using data from time-resolved fluorescence measurements as shown earlier, within the caveats already mentioned. This has the dual advantages of substantially improving the precision of the values obtained, and showing that above a certain threshold concentration, extra lifetime components appear which are of similar order to fluorescence lifetime components observed in 2AP-containing oligonucleotides,[2, 19, 20, 29] which suggests that distinct emitting populations appear above the threshold. These extra lifetime components support the existence of simultaneous quenching mechanisms, dynamic quenching from the linear decrease in the longest lifetime component, and static quenching from the appearance of additional emitting species at higher quencher concentrations. Considering dynamic quenching first, a trend of G ~ T > A ~ C is generally observed, although there is some variation under different conditions. In contrast, the dynamic quenching shows greater variation, which indicates quenching of 2AP fluorescence emission due to electron transfer, as it is consistent with the free energies of electron transfer calculated for the corresponding natural DNA base and excited state 2AP pairs.[22]

Determining a consistent trend for static quenching is more dubious, due to problems with guanine and concentration effects due to the solubility of the ribosides, but with these caveats the general trend G ~ A > T ~ C is obtained for static quenching from combined time-resolved and steady-state fluorescence data. However, examining the static quenching calculated solely from time-resolved data shows the equilibrium constant of complex formation, and by inspecting the values of the shorter lifetime components, the trend of efficiency of non-radiative decay within the 2AP-base dimer

structures is consistent with the trend that one would expect from an electron transfer mechanism. Combined static and dynamic quenching observed from the time-resolved data is consistent with the total quenching represented in the steady-state fluorescence data, since guanine is generally the strongest quencher in both mechanisms, adenine and thymine have intermediate quenching efficiency, and cytosine is the least efficient quencher. The overall trend of combined quenching from time-resolved fluorescence measurements is thus found to be G > A ~ T > C, which is consistent with the trend found from steady-state fluorescence data, and moreover is consistent with the observed quenching of 2AP fluorescence in dinucleotides.[2]

4.5 Conclusions

In contrast to the findings of prior reports, consistent trends for the total quenching efficiency of free 2AP by the natural DNA bases in solution has been found, in the order G > A > T > C, in both 0.1 M phosphate buffer and 20 mM tris-HCl buffers. Dynamic quenching represented by rate constants k_q were greater for GMP and dTMP than for AMP and CMP, which is consistent with charge transfer when considered in conjunction with previously reported redox potentials.[22] Flourescence lifetime measurements revealed that the nature of the buffer can significantly affect the fluorescence decay of 2AP in the absence of the chosen quenchers. In 0.1 M phosphate buffer, 2AP had a fluorescence lifetime half that seen in tris-HCl buffer, with a dynamic quenching rate constant k_q 1.0 x 10^9 M^{-1} s^{-1}. This behaviour has not previously been reported for 2AP, somewhat unexpectedly given the common usage of phosphate buffers, and was not accounted for by Narayanan *et al.*[22]

Time-resolved fluorescence measurements of 2AP also clearly indicate the appearance of extra, shorter lifetime components at higher concentrations of the natural bases, with similar lifetimes to those seen in 2AP-containing oligonucleotides. These lifetime components are consistent with ground state interactions between 2AP and the natural bases, leading to the conclusion that these complexes take the form of stacked structures. Conventionally, statically quenched fluorophores are considered non-fluorescent and not observable in time-resolved fluorescence measurements due to extremely rapid non-radiative decay, but with the advent of femtosecond laser light sources and more accurate detection equipment, it is entirely reasonable that these statically quenched populations move into the window of detection. The increased

sensitivity afforded by this improved instrumentation means that static quenching can be directly quantified, despite exhibiting quantum yields some orders of magnitude smaller than 2AP in water. Based on the short lifetime components of 2AP attributed to static quenching by the natural DNA bases, a similar trend to that found for dynamic quenching is seen, which is again consistent with a charge transfer mechanism.

Lastly, the work presented in this chapter shows that with care and an appropriate solvation environment, fluorescence measurements of free 2AP in solution yields insights into the processes taking place in 2AP-substituted oligonucleotides and closely mimics previously observed properties of 2AP in such oligonucleotides.

4.6 References

1. A. C. Jones and R. K. Neely, *Q Rev Biophys*, 2015, **48**, 244-279.
2. O. F. A. Larsen, I. H. M. van Stokkum, F. L. de Weerd, M. Vengris, C. T. Aravindakumar, R. van Grondelle, N. E. Geacintov and H. van Amerongen, *Physical Chemistry Chemical Physics*, 2004, **6**, 154-160.
3. R. K. Neely, S. W. Magennis, D. T. F. Dryden and A. C. Jones, *The Journal of Physical Chemistry B*, 2004, **108**, 17606-17610.
4. D. C. Ward, E. Reich and L. Stryer, *Journal of Biological Chemistry*, 1969, **244**, 1228-1237.
5. L. C. Sowers, G. V. Fazakerley, R. Eritja, B. E. Kaplan and M. F. Goodman, *P Natl Acad Sci USA*, 1986, **83**, 5434-5438.
6. R. Eritja, B. E. Kaplan, D. Mhaskar, L. C. Sowers, J. Petruska and M. F. Goodman, *Nucleic Acids Res*, 1986, **14**, 5869-5884.
7. T. M. Nordlund, S. Andersson, L. Nilsson, R. Rigler, A. Graslund and L. W. McLaughlin, *Biochemistry*, 1989, **28**, 9095-9103.
8. D. Xu, K. O. Evans and T. M. Nordlund, *Biochemistry*, 1994, **33**, 9592-9599.
9. D. A. Smith, L. F. Holroyd, T. van Mourik and A. C. Jones, *Phys Chem Chem Phys*, 2016, **18**, 14691-14700.
10. A. Dallmann, L. Dehmel, T. Peters, C. Mügge, C. Griesinger, J. Tuma and N. P. Ernsting, *Angewandte Chemie International Edition*, 2010, **49**, 5989-5992.
11. C. R. Guest, R. A. Hochstrasser, L. C. Sowers and D. P. Millar, *Biochemistry*, 1991, **30**, 3271-3279.
12. E. L. Rachofsky, E. Seibert, J. T. Stivers, R. Osman and J. B. A. Ross, *Biochemistry*, 2001, **40**, 957-967.
13. C. Wan, T. Fiebig, O. Schiemann, J. K. Barton and A. H. Zewail, *Proceedings of the National Academy of Sciences*, 2000, **97**, 14052-14055.
14. M. A. O'Neil and J. K. Barton, *Journal of the American Chemical Society*, 2002, **124**, 13053-13066.
15. M. A. O'Neill, H.-C. Becker, C. Wan, J. K. Barton and A. H. Zewail, *Angewandte Chemie International Edition*, 2003, **42**, 5896-5900.
16. M. A. O'Neill and J. K. Barton, *Journal of the American Chemical Society*, 2004, **126**, 13234-13235.
17. M. A. O'Neil and J. K. Barton, *Journal of the American Chemical Society*, 2004, **126**, 11471-11483.
18. M. A. O'Neill, C. Dohno and J. K. Barton, *Journal of the American Chemical Society*, 2004, **126**, 1316-1317.
19. R. K. Neely, D. Daujotyte, S. Grazulis, S. W. Magennis, D. T. Dryden, S. Klimasauskas and A. C. Jones, *Nucleic Acids Res*, 2005, **33**, 6953-6960.
20. R. K. Neely and A. C. Jones, *Journal of the American Chemical Society*, 2006, **128**, 15952-15953.
21. E. L. Rachofsky, R. Osman and J. B. Ross, *Biochemistry*, 2001, **40**, 946-956.
22. M. Narayanan, G. Kodali, Y. J. Xing and R. J. Stanley, *Journal of Physical Chemistry B*, 2010, **114**, 10573-10580.

23. T. Alev-Behmoaras, J. J. Toulmé and C. Hélène, *Biochimie*, 1979, **61**, 957-960.

24. H. Pal, D. K. Palit, T. Mukherjee and J. P. Mittal, *Journal of Photochemistry and Photobiology A: Chemistry*, 1990, **52**, 391-409.

25. S. I. Vdovenko, M. T. Kolycheva, I. I. Gerus and V. P. Kukhar, *Amino Acids*, 1993, **4**, 303-306.

26. L. Holroyd, University of St. Andrews, 2015.

27. W. Eimer and T. Dorfmueller, *The Journal of Physical Chemistry*, 1992, **96**, 6790-6800.

28. G. McKenzie, University of Edinburgh, 2017.

29. O. J. G. Somsen, v. A. Hoek and v. H. Amerongen, *Chemical Physics Letters*, 2005, **402**, 61-65.

Chapter 5 Electronic Energy Transfer in 2AP-containing Dinucleotides

"We haven't the money, so we've got to think."

Ernest Rutherford

5.1 Introduction

It has been understood for over a century that exposure of DNA to UV radiation causes mutations and damage to DNA strands. This has been extensively studied in the context of skin cancer and melanoma, skin naturally being the most exposed bodily organ to UV radiation.[1-3] Electronic energy transfer[4-8] between DNA bases under UV-illumination is reported to increase the likelihood of photochemical damage, mutations and consequently diseases such as cancer. Until recently, the mechanism by which electronic energy transferred between DNA bases was poorly understood and could not explain observed patterns of damage to DNA as a result of UV irradiation.[9] Recent work by McKenzie[10] using 2AP-containing dinucleotides showed that energy transfer between electronically excited DNA bases demonstrated conformational selectivity of the transfer process, by comparing rates of energy transfer at 77 K and at room temperature. A number of specific findings were reported by McKenzie, including different 2AP excited state decay observed due to direct (310 nm) or indirect (260 nm) excitation; similarly, different QY for direct and indirect excitation of 2AP (neglected in previous studies, such as work published by Nordlund *et al*[11]); energy transfer being favoured by conformations with stacked bases; and extraction of energy transfer efficiency from fluorescence lifetimes and A-factors.

In this chapter, the focus will be on the temperature dependence of energy transfer in the solution phase from 5 °C to 25 °C. This is in contrast to most previous work already cited, which largely has a biological or medical context. It could be considered that this is an extension of previous work described in Chapter 4, using 2AP as a fluorescent probe of DNA conformation. However, where in the previous chapter the focus was on changes in the fluorescence emission of 2AP, here the method of excitation will also play a role. In short, fluorescence lifetimes from direct excitation of 2AP in a dinucleotide at 310 nm will be compared to fluorescence from 2AP as a result of excitation of the adjacent natural base to estimate the degree of energy transfer from the electronically excited natural base and 2AP.

5.1.1 Excited State Decay of DNA Bases

As has been alluded to elsewhere in this thesis, the shared photophysical property of DNA bases is their extremely fast non-radiative decay, on 10's of femtosecond to picosecond timescales.[12, 13] A computational study by Serrano-Andres

et al have shown this to be due to the presence of conical intersections (CIs) between the potential energy surfaces (PES) of ground and excited states.[14] These CIs are the points on the PES where the ground and excited state become degenerate and therefore intersect. Despite this very fast decay, however, DNA bases, particularly pyrimidines, can remain in the excited state long enough for interactions or processes with neighbouring bases to occur. Bearing in mind that these are essentially intramolecular processes, photoproducts can form even in the very short excited state lifetime. It is possible for pyrimidines in general to form covalently-bonded dimers,[15-17] or for cytosine in particular[10] to undergo photohydration. More pertinently, it is also possible for electronic energy to be transferred from a natural base to 2AP.

5.1.2 Electronic Energy Transfer

As discussed in Chapter 2, energy can be transferred between an electronically excited molecule (donor) and a nearby ground state species (acceptor), given certain conditions such as (in the case of resonance energy transfer, RET) the alignment of the donor and acceptor transition dipole moments. In consequence, not only do donor and acceptor have to be in close proximity while the acceptor is in the excited state, but the relative orientation of donor and acceptor is also important for energy transfer to take place. To give an idea of the typical scale over which energy transfer occurs, RET (the most common type of energy transfer) often occurs over distances (between donor and acceptor) up to tens of angstroms and is proportional to the inverse sixth power of the distance.[18] Potentially, this will allow inferences about the effect of DNA conformation on the fluorescence of 2AP to be drawn from energy transfer measurements. A Jablonski diagram illustrating the process is shown in Figure 5.1 below. Briefly, absorption of a photon by the donor propels it into the excited state, followed by relaxation to the lowest energy vibrational level (if this is not already the case). If decay to the ground state of the donor causes a difference in energy closely matching the energy required for electronic excitation of the acceptor, energy transfer between donor and acceptor can take place. The excited state acceptor can then undergo either radiative or non-radiative decay as it normally would, in the case of a fluorophore decaying *via* fluorescence emission.

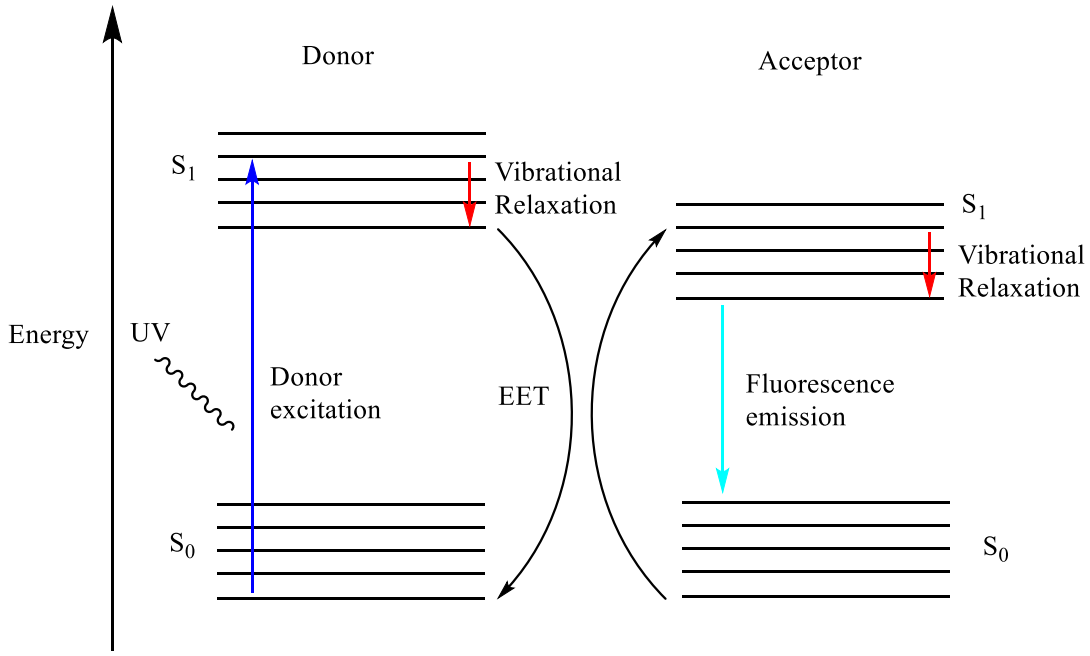

Figure 5.1: Jablonski diagram representing electronic energy transfer from excited state donor to acceptor. Electronic excitation of the donor molecule *via* UV light absorption is followed by vibrational relaxation. Energy transfer between donor and acceptor takes placing, propelling the acceptor into an excited electronic state S_1. This is followed by vibrational relaxation and decay to the ground state by fluorescence emission of the acceptor.

5.1.2.1 Energy transfer between the natural bases

Earlier work on energy transfer in DNA utilised steady-state fluorescence[8, 11, 19, 20] to elucidate the mechanism of electronic energy transfer, more recently theoretical calculations and femtosecond pump-probe spectroscopy[21-26] were employed. Typically, a 'point-to-point' exciton approximation is used as the mechanism of electronic energy moving from one base to an adjacent, preventing localisation of excess electronic energy. Each 'hop' is often presented as the result of traditional resonance energy transfer from the interaction of transition dipole moments, but as Czader *et al*[27] point out, this neglects the short distance between adjacent DNA bases relative to average DNA base dimensions. This point is reinforced by Olaya-Castro and Scholes,[28] who point out that overlap of donor and acceptor orbitals, which is normally neglected because of rapid attenuation with distance of this overlap, may be significant in the case of adjacent DNA bases due to the relatively short separation distance. Regardless of the exact mechanism, however, the message is clear that electronic energy resulting from incident radiation can transfer between adjacent natural DNA bases.

5.1.2.2 Energy transfer between 2AP and the natural bases

It is likely for 2AP substituted into a strand of DNA that a similar energy transfer process takes place, given the similarity of the structure of 2AP and adenine, and that substitution of 2AP into DNA has already been shown in previous chapters not to greatly perturb the natural conformation of DNA. Interactions between 2AP and the natural bases due to orbital overlap of the type described in the previous paragraph has to some extent been implied in previous work by Bonnist and Jones.[29] The authors showed that 2AP in a stacked oligonucleotide clearly exhibited signs of emission at longer wavelengths than free 2AP, suggesting orbital overlap between 2AP and the adjacent DNA bases. This is important for the reason that energy transfer at relatively short separation distances likely involves a significant amount of orbital overlap, as in the discussion above about the limitations of the typical Förster energy transfer model.

	η_{SS} (rt) /%	η_{SS} (77K) /%
2AP/G	<15	63
2AP/T	11	~100
2AP/A	27	86
2AP/I	11	54

Table 5.1: Energy transfer efficiencies reported for 2AP-containing dinucleotides in tris-HCl buffer (20 mM, 0.1 M NaCl) at room temperature and LiCl (6 M) at 77 K from steady-state fluorescence measurements. Data reproduced from reference 10.

Some crucial differences exist between energy transfer between natural bases and energy transfer to 2AP from the natural bases, besides the fact that 2AP is fluorescent. Absorbance wavelengths for 2AP are longer than those for the natural bases, so it is possible to selectively excite 2AP or natural bases in an oligonucleotide strand, and measure the resulting fluorescence with the reasonable assumption that any emission is solely due to 2AP. Earlier work by Grant McKenzie[10] reproduced in Table 5.1 showed that energy transfer clearly occurs for 2AP-containing dinucleotides, both at room temperature in water and with greatly increased efficiency at 77 K in LiCl glass.

A large change in transfer efficiency at room temperature (298 K) compared to 77 K was seen in the previous work (Table 5.1). At first glance, this would appear to be due to the large temperature change; while this is highly relevant, a temperature change of this magnitude will have caused a change in phase. Even considering the high salt concentration, which will have depressed the melting point, at 77 K an

aqueous solution will be in a different state than at room temperature. Whether this state is a solid or a "glass", the mobility and structural flexibility of any solutes, whether a dinucleotide or anything else, will be highly restricted. In essence, the dinucleotide structure at 77 K will be rigid and static, unlike at room temperature, not only because the low temperature reduces vibration and rotation, but because the surrounding solvent molecules hold it in place. From the previously reported results, it seems that reduced mobility of the dinucleotide structures favours interactions between 2AP and the adjacent natural base which give rise to energy transfer.

	η_{TRF} /%	$\eta_{TRF,multi}$ /%
2AP/G	8	11
2AP/T	6	10
2AP/A	5	26
2AP/I	5	11

Table 5.2: Energy transfer efficiencies reported for 2AP-containing dinucleotides (~10 μM) in tris-HCl buffer (20 mM, 0.1 M NaCl) at room temperature from time-resolved fluorescence measurements. Data reproduced from reference 10.

Two sets of energy transfer efficiencies for 2AP-containing dinucleotides are shown in Table 5.2, both from time-resolved fluorescence measurements with multi-exponential decay observed. As discussed already in Chapter 4, different fluorescence lifetime components of 2AP in di- or oligonucleotides are interpreted as representing different conformations of DNA. One set of results (η_{TRF}) is based on the assumption energy transfer occurs in only one conformational state of the dinucleotide (i.e. excites only one lifetime component of 2AP), while the calculation of $\eta_{TRF,multi}$ allows for energy transfer in all conformational states. This leads to a clear difference in energy transfer efficiency obtained, especially for 2AP/A with a five-fold increase. The results in Table 5.2 show that assuming that only one lifetime component, i.e. only one observed conformation of the dinucleotide, contributed to energy transfer yields an underestimate of the correct value.

	η_{TRF} /%
G	19
T	10
A	57

Table 5.3: Energy transfer efficiencies at 5 °C from Nordlund *et al*[11] of septamer oligonucleotides with sequence CCAN(2AP)CC, where N = G, T or A.

Other literature sources have used longer oligonucleotide strands to measure energy transfer efficiency to 2AP, such as Nordlund *et al*[11] with a study of heptamers. Their calculated energy transfer efficiencies for each base 5' to 2AP are shown in Table 5.3 above. These efficiencies have the advantage of being measured in the solution phase at a more precisely specified temperature. Unfortunately, there is also a large dose of uncertainty created by the use of oligonucleotides rather than dinucleotides, making it harder to discern exactly how much of the energy transfer was due to specific bases. It is not impossible to correct for this, given their careful choice of sequences, but there is still a chance of over- or underestimation. The calculated transfer efficiency from bases adjacent to 2AP relies on accurately estimating the contribution of bases further away. Regardless, it still appears that there is an increase in energy transfer from guanine and adenine with decreased temperature in the solution phase. This may indicate that the vast increase in transfer efficiency at 77 K is not just a consequence of the change in phase. For this reason, the work in this chapter will focus on the energy transfer between 2AP and natural bases in systems with only two nucleotides in solution at a range of defined temperatures. Time-resolved fluorescence measurements of 2AP by direct and indirect excitation within 2AP-containing dinucleotides, and used to calculate energy transfer efficiencies. Related, unpublished, previous work using steady-state fluorescence measurements to calculate energy transfer efficiencies by a project student James Kent[30] will also be presented.

5.2 Experimental Details

Dinucleotides containing 2AP (6-13 μM) were obtained from ATDBio and used as received. Fluorescence measurements were carried out in Tris-HCl buffer (20 mM, 60 mM NaCl). Sample temperature was controlled by passing water from a water bath set to the chosen temperature through the wall of the cuvette holder in the sample chamber. Steady-state fluorescence measurements were carried out by undergraduate student James Kent,[30] using excitation wavelength 260 nm with emission wavelength range 275 – 505 nm & 305 nm with emission wavelength range 320 – 595 nm. Time-resolved fluorescence measurements were carried out with excitation wavelengths of 310 nm for direct excitation and 260 nm for indirect excitation were used. Emission was measured separately at 360, 380 and 400 nm for each dinucleotide and excitation wavelength. Fluorescence decay curves were fitted multi-exponentially with four

lifetime components using Edinburgh Instrument's FAST software. This was based on previous studies which found that four components were required in order to accurately describe the fluorescence decay of 2AP-containing oligonucleotide strands.[31]

Under the assumption that only one lifetime component was populated by energy transfer, as set out above, energy transfer efficiency was calculated using the method described by Grant McKenzie in his PhD thesis.[10] If we ignore the small changes in lifetime between direct and indirect excitation, then it follows that the decay from indirect excitation can be described by:

$$I(t)_{260} = \left(\frac{1}{1 + B_j}\right) \sum_i A_{i(310)}\, e^{-t/\tau_i} + B_j\, e^{-t/\tau_j} \qquad 5.1$$

where the proportion of component *j* excited by energy transfer is $\left(\frac{B_j}{1+ B_j}\right)$, τ_i/τ_j is the fluorescence lifetime of component *i*/*j*, and A_i is the A-factor of the i^{th} component at the given excitation wavelength so that $\sum A_{i(310)} = 1$. With some rearrangement, B_j can be defined in terms of the measured A-factors as

$$B_j = \frac{A_{j(260)} - A_{j(310)}}{1 - A_{j(260)}} \qquad 5.2$$

Hence, the excited state population of 2AP due to energy transfer, A_{ET}, can be calculated using

$$A_{ET} = \frac{B_j}{1 + B_j} \qquad 5.3$$

Energy transfer efficiencies based on time-resolved fluorescence measurements were then obtained from

$$\eta_{TRF} = \frac{A_a(\lambda_{exc})}{A_d(\lambda_{exc})} \text{ x } \frac{A_{ET}}{1 - A_{ET}} \qquad 5.4$$

where η_{TRF} is the energy transfer efficiency from time-resolved fluorescence, A_a is the absorbance of the acceptor (2AP) and A_d is the absorbance of the donor (the adjacent natural base) at the excitation wavelength. For the remaining lifetime components assumed not to be populated by energy transfer (that is, $i \neq j$), the A-factors for indirect excitation at 260 nm were obtained with

$$A_{i(260)} = \frac{A_{i(310)}}{1 + B_j} \quad 5.5$$

In order to account for the possibility that energy transfer occurred across multiple lifetime components, the energy transfer efficiencies were re-calculated as set out below, again using the method described by Grant McKenzie in his PhD thesis.[10] Here, the fluorescence decay resulting from 260 nm excitation was described by

$$I(t)_{260} = \frac{1}{\sum(A_{i(310)} + B_i)} \sum_i (A_{i(310)} + B_i)\, e^{-t/\tau_i} \quad 5.6$$

Following similar logic from the experimental details section, A-factors for 260 nm excitation can be calculated from

$$A_{i(260)} = \frac{A_{i(310)} + B_i}{\sum(A_{i(310)} + B_i)} \quad 5.7$$

where the directly excited proportion of component *i* is $\frac{A_{i(310)}}{\sum(A_{i(310)}+B_i)}$ and $\frac{B_i}{\sum(A_{i(310)}+B_i)}$ is the indirectly excited proportion of component *i* by energy transfer, $A_{i(ET)}$. Non-linear least squares fitting in Microsoft Excel was used to solve equation 5.7 for B_i, and subsequently $A_{i(ET)}$. Energy transfer efficiency was then calculated using

$$\eta_{TRF} = \frac{A_a(\lambda_{exc})}{A_d(\lambda_{exc})} \text{ x } \frac{\sum A_{ET}}{1 - \sum A_{ET}} \quad 5.8$$

5.3 Results

Energy transfer efficiencies of 2AP-containing dinucleotides from steady-state fluorescence emission are shown in Table 5.4, performed by project student James Kent.[30] A range of temperatures from 5 to 25 °C were measured, showing clear inverse trends of increasing transfer efficiency with decreasing temperature. Assuming that excitation at 305 nm represented direct excitation of 2AP, while excitation at 260 nm represented indirect excitation of 2AP *via* the adjacent natural base, energy transfer efficiencies were calculated from the different emission intensities at the two excitation wavelengths.

Temperature /°C	2AP/A /%	2AP/G /%	2AP/T /%
5	22	4.7	8
10	20	4.4	8
15	18	3.3	7
20	16	2.2	6
25	15	0.7	4

Table 5.4: Energy transfer efficiencies for 2AP-containing dinucleotides calculated from steady-state fluorescence emission measurements, using excitation wavelengths of 260 and 309 nm separately. Data reproduced from project student James Kent.[30]

Fluorescence lifetime components for 2AP-containing dinucleotides (with the exception of 2AP/C, due to the formation of photo-products at an excitation wavelength of 260 nm) are shown in Table 5.5 to Table 5.7 below, at temperatures from 5 °C to 25 °C inclusive in 5 °C increments. Only results obtained from emission at 380 nm are shown here, but data for emission at 360 and 400 nm are shown in . In similar fashion to the steady-state results, excitation at 310 nm was taken to represent direct excitation of 2AP, while excitation at 260 nm was assumed to represent excitation solely of the natural base adjacent to 2AP, which it was assumed was followed by energy transfer to 2AP (indirect excitation). However, the absorbance of 2AP at 260 nm was small but not negligible, which was accounted for in the final step of the energy transfer calculation described further on.

Time-resolved fluorescence data of 2AP/G and 2AP/T in Table 5.6 and Table 5.7, respectively, showed that by comparing the corresponding A-factors from excitation at 260 and 310 nm, both dinucleotides exhibited energy transfer most clearly for the shortest lifetime component. In contrast, 2AP/A in Table 5.5 show that the population of τ_3 was significantly higher for indirect excitation at 260 nm relative to direct excitation at 310 nm, at the expense of the other lifetime components. There is also a clear decrease in the population of the relevant lifetime component with increasing temperature, suggesting that energy transfer is temperature-dependent for all three dinucleotides studied. It is useful to recall the model from Chapter 4, whereby the shortest lifetime component represents ‘perfect’ base stacking, while the longest lifetime component represents a completely unstacked conformation, with the remaining intermediate components representing stacked conformations somewhere in-between the two ‘extreme’ components. By this model, the results for 2AP/A are unexpected, since they suggest that energy transfer is most efficient for the second

Excitation wavelength /nm	260		310	
Temperature /°C	τ_i /ns	A_i	τ_i /ns	A_i
5	10.18	0.06	10.07	0.11
	3.07	0.09	2.93	0.15
	0.91	0.55	0.74	0.37
	0.29	0.30	0.18	0.37
10	10.07	0.06	9.97	0.11
	2.96	0.09	2.84	0.15
	0.86	0.54	0.72	0.36
	0.29	0.30	0.16	0.38
15	9.80	0.07	9.77	0.11
	2.66	0.11	2.60	0.17
	0.78	0.56	0.67	0.35
	0.24	0.27	0.15	0.37
20	9.63	0.06	9.65	0.11
	2.65	0.10	2.59	0.17
	0.76	0.56	0.77	0.35
	0.22	0.28	0.18	0.37
25	9.43	0.07	9.44	0.10
	2.49	0.11	2.34	0.17
	0.74	0.53	0.64	0.33
	0.24	0.29	0.12	0.39

Table 5.5: Fluorescence lifetimes of 2AP/A (5'/3') dinucleotide with emission wavelength 380 nm and excitation wavelengths at 260 and 310 nm, over the temperature range 5 – 25 °C in 5 °C increments. Measurements were taken in a tris-HCl (20 mM, 60 mM NaCl) buffer solution. Fluorescence lifetimes for each temperature were obtained using global analysis of emission wavelengths 360, 380 and 400 nm.

Excitation wavelength /nm	260		310	
Temperature /°C	τ_i /ns	A_i	τ_i /ns	A_i
5	10.47	0.09	10.14	0.09
	2.48	0.06	2.54	0.15
	0.49	0.06	0.45	0.13
	0.06	0.79	0.07	0.63
10	10.34	0.09	9.97	0.08
	2.33	0.06	2.31	0.12
	0.48	0.06	0.45	0.16
	0.05	0.79	0.07	0.64
15	10.13	0.10	9.76	0.08
	2.12	0.08	2.10	0.18
	0.45	0.07	0.43	0.11
	0.05	0.76	0.06	0.63
20	9.94	0.10	9.56	0.07
	1.92	0.08	1.90	0.19
	0.42	0.06	0.36	0.13
	0.05	0.76	0.05	0.61
25	9.72	0.11	9.34	0.07
	1.79	0.10	1.73	0.20
	0.42	0.07	0.35	0.12
	0.05	0.73	0.05	0.61

Table 5.6: Fluorescence lifetimes of 2AP/G (5'/3') dinucleotide with emission wavelength 380 nm and excitation wavelengths at 260 and 310 nm, over the temperature range 5 – 25 °C in 5 °C increments. Measurements were taken in a tris-HCl (20 mM, 60 mM NaCl) buffer solution. Fluorescence lifetimes for each temperature were obtained using global analysis of emission wavelengths 360, 380 and 400 nm.

Excitation wavelength /nm	260		310	
Temperature /°C	τ_i /ns	A_i	τ_i /ns	A_i
5	9.35	0.02	9.09	0.03
	3.36	0.13	3.40	0.27
	0.48	0.09	0.46	0.16
	0.06	0.76	0.07	0.54
10	9.55	0.02	9.54	0.03
	3.08	0.14	3.12	0.30
	0.47	0.09	0.46	0.14
	0.06	0.75	0.08	0.53
15	9.49	0.01	9.41	0.02
	2.80	0.16	2.83	0.31
	0.42	0.09	0.45	0.13
	0.05	0.74	0.07	0.54
20	9.54	0.01	9.40	0.02
	2.54	0.18	2.54	0.34
	0.39	0.10	0.40	0.13
	0.05	0.71	0.07	0.51
25	9.52	0.01	9.44	0.02
	2.31	0.21	2.32	0.34
	0.40	0.09	0.40	0.12
	0.06	0.69	0.07	0.52

Table 5.7: Fluorescence lifetimes of 2AP/T (5'/3') dinucleotide with emission wavelength 380 nm and excitation wavelengths at 260 and 310 nm, over the temperature range 5 – 25 °C in 5 °C increments. Measurements were taken in a tris-HCl (20 mM, 60 mM NaCl) buffer solution. Fluorescence lifetimes for each temperature were obtained using global analysis of emission wavelengths 360, 380 and 400 nm.

most well-stacked conformation, and not the most well-stacked conformation. There was also no immediately apparent trend in the population of the third lifetime component A_3, as a proxy for energy transfer efficiency (discussed further below).

Energy transfer efficiencies obtained using equations 5.2, 5.3 & 5.4 as a function of temperature are shown in Table 5.8 below. Only 2AP/T exhibited a consistent trend, decreased energy transfer efficiency with increased temperature, with 2AP/G showing a similar trend but not for all temperatures recorded here. In contrast, 2AP/A showed no apparent trend at all with temperature. The results shown here are not consistent with the trends in previous steady-state measurements by James Kent[30] in the introduction, where decreased energy transfer efficiencies with increased temperature and higher corresponding energy efficiencies were shown across all three dinucleotides.

Temperature /°C	2AP/A /%	2AP/G /%	2AP/T /%
5	5	12	9
10	5	12	8
15	5	9	7
20	6	11	7
25	5	7	5

Table 5.8: Energy transfer efficiencies for 2AP-containing dinucleotides calculated from fluorescence lifetime data at 380 nm emission, on the assumption that a single lifetime component is populated by energy transfer. For 2AP/A this was assumed to be τ_2, while for 2AP/G and 2AP/T τ_1 appeared to be the main component populated by indirect excitation at 260 nm.

The explanation for this discrepancy may lie in the assumption that only one lifetime component was populated in the energy transfer process. When predicted A-factors from equation 5.5 were compared with the measured values at 20 °C, both shown in Table 5.9, numerous discrepancies were found between predicted and measured values. This suggests that more than one lifetime component is excited by energy transfer.

		A_1	A_2	A_3	A_4	$< \tau > /ns$
2AP/A	Measured	0.06	0.10	0.56	0.28	1.37
	Predicted	0.08	0.11	0.56	0.25	1.33
2AP/G	Measured	0.10	0.08	0.06	0.76	1.18
	Predicted	0.04	0.12	0.08	0.76	0.73
2AP/T	Measured	0.02	0.17	0.10	0.71	0.65
	Predicted	0.01	0.20	0.08	0.71	0.68

Table 5.9: Measured and predicted A-factors for 2AP fluorescence in dinucleotides at 20 °C from indirect excitation of the adjacent natural base at 260 nm and subsequent energy transfer from the natural base to 2AP. Equation 5.5 was used to calculate the predicted values.

Calculated A_i values at 260 nm from fitted B_i values for each dinucleotide at 20 °C are shown in Table 5.10 below. These predicted values, taking into account the contribution of each decay component, are in extremely close agreement with the measured values displayed in Table 5.9 previously. This provided further confirmation the previous assumption that only one decay component contributes to energy transfer was not sufficiently representative of the energy transfer process.

	A_1	A_2	A_3	A_4	$< \tau > /ns$
2AP/A	0.06	0.10	0.56	0.27	1.37
2AP/G	0.07	0.10	0.07	0.76	1.18
2AP/T	0.01	0.17	0.10	0.71	0.65

Table 5.10: Predicted A_i values at 260 nm excitation calculated from fitted B_i values for each dinucleotide at 20 °C, assuming every decay component contributes to energy transfer.

Energy transfer efficiencies from equation 5.8 are shown in Table 5.11 below. Energy transfer for all dinucleotides showed decreased transfer efficiency with increased temperature over the range shown. The trends and values shown have very good agreement with the values obtained previously, shown in Table 5.4, from steady-state fluorescence measurements by James Kent.[30] These trends are also consistent with the previous results from Grant McKenzie[10], where measurements at room temperature and 77 K showed significantly reduced temperature vastly increased the efficiency of energy transfer. However, the magnitude of values for individual dinucleotides reported here at 20 °C is different to those in the previous study. It is likely that the values obtained at 20 °C are the most comparable to the previous work, due to those measurements being performed in the same COSMIC facility, which is maintained at 20 °C. The discrepancy may be due to degradation over time of the

samples, which were obtained several years before the start of the work described in this thesis. This appears less likely, however, when considering the good agreement between the steady-state measurements from James Kent[30] in the introduction and the time-resolved fluorescence-based results presented above in Table 5.11, which were carried out at least a year apart using the same sample stock. It is also possible, however, that controlling the temperature reduced variability in the energy transfer measurement, as shown here even over the relatively short temperature range examined, clearly observable changes in energy transfer efficiency were found. These changes could easily account for the difference in magnitudes seen here and in the work by Grant McKenzie, due to heating effects from the power of the laser excitation source over the course of the measurement. A single decay measurement typically took between 10 minutes and half an hour in the current work, during which time laser heating in the absence of any temperature control was highly likely to have occurred.

Temperature /°C	2AP/A /%	2AP/G /%	2AP/T /%
5	30	8	26
10	28	8	24
15	25	6	20
20	25	6	18
25	20	5	11

Table 5.11: Energy transfer efficiencies for 2AP-containing dinucleotides calculated from fluorescence lifetime data at 380 nm emission, taking into account energy transfer for all fluorescence lifetime components. Energy transfer efficiencies at 360 and 400 nm emission are shown in .

$$\eta_{SS,corr} = \eta_{SS} \text{ x } \frac{< \tau >_{dir}}{< \tau >_{ind}} \qquad 5.9$$

A correction can also be applied to the steady-state results found previously by James Kent,[30] which relied upon the assumption that the fluorescence quantum yield of 2AP is the same for direct and indirect excitation. Average lifetimes (calculated using the B_i values from the least-squares analysis for indirect excitation) from the time-resolved fluorescence measurements presented in this work showed that this is not a reasonable assumption, although for 2AP/G the values for direct and indirect excitation were not very dissimilar. Since quantum yield and average fluorescence lifetime are proportional, the relevant correction can be applied using equation 5.9 and the calculated average lifetime for both direct and indirect excitation. These corrected steady-state energy transfer values from equation 5.9 were in extremely good

agreement with the transfer efficiencies in Table 5.11 derived from time-resolved fluorescence measurements, with the exception of 2AP/G at higher temperatures. This may simply be due to the reduced transfer efficiency of guanine causing extra uncertainty in the average lifetime due to indirect excitation. Using this average lifetime with equation 5.9 to correct the steady-state-derived transfer efficiency reduced the accuracy of the 2AP/G values reported in Table 5.12, especially at 25 °C.

Temperature /°C	2AP/A /%	2AP/G /%	2AP/T /%
5	30	8	26
10	28	7	24
15	25	4	20
20	25	4	18
25	20	<1	11

Table 5.12: Energy transfer efficiencies for 2AP-containing dinucleotides from steady-state fluorescence measurements, corrected using average fluorescence lifetimes of the relevant dinucleotide at the stated temperature. Original energy transfer values from project student James Kent.

5.4 Discussion

As already stated, energy transfer efficiencies for the dinucleotides 2AP/A, 2AP/T and 2AP/G were found for the temperature range 5-25 °C. In all cases, the efficiency of energy transfer dropped with increased temperature. It was shown in the introduction that energy transfer occurs as a result of interaction between 2AP and the natural base in the excited state, and generally an increase in temperature leads to increased interaction between molecules in solution. However, the system and interaction being studied here was intramolecular in nature. Furthermore, energy transfer relies specifically on the interaction between the transition dipole moments of 2AP and the adjacent natural base, which is highly sensitive to the degree of alignment between the two dipole moments. In addition, as noted in the introduction, the very close proximity of neighbouring DNA bases suggests that significant overlap of molecular orbitals is highly likely, which is usually neglected by classical resonance energy transfer models. Regardless of whether energy transfer proceeds *via* dipole-dipole interactions or molecular orbital overlap or even both mechanisms simultaneously, a common feature of both mechanisms is a strong dependence on separation distance and relative orientation.

Seen in this context, it appears obvious that an increase in temperature will lead to a decreased probability of energy transfer, due to increased conformational flexibility and vibrational motion of the dinucleotide. Recall from the introduction that natural bases undergo non-radiative decay extremely quickly due to the presence of CI in the PES. This effectively means that the dinucleotide must ideally already be in the correct conformation for energy transfer at the time of excitation, or else be able to adopt a suitable conformation within the very short lifetime of the excited state of the natural base. In practice, a suitable conformation likely means that 2AP and the natural base in the dinucleotide need to be π-stacked, typically represented by the shorter lifetime components. The lifetime data shown above in Table 5.5, Table 5.6, and Table 5.7 show that the proportion of shorter lifetimes, which likely represent the base-stacked structures that contribute the most to energy transfer, decreased with increased temperature. This suggests that the observed decrease in energy transfer with increasing temperature was likely due to increased flexibility reducing the population of the ideal dinucleotide conformation(s) for energy transfer.

So far, based on the results presented here, it seems that energy transfer is linearly dependent on temperature, more specifically that it is inversely proportional to temperature. A number of inferences can be drawn from this information, most importantly that the observed results are actually a consequence of energy transfer and not charge or electron transfer. As repeatedly mentioned throughout this chapter, energy transfer is dependent on relative orientation, not just separation distance, and increased thermal motion makes conformations conducive to energy transfer less likely, or disrupts such conformations during the excited state lifetime, making other decay processes more likely. In contrast, electron transfer is less particular about conformation and will be favoured by higher temperatures. However, temperature of aqueous solutions cannot be decreased indefinitely and remain in the liquid phase. Certainly by 77 K, as shown in the previous work by Grant McKenzie,[10] a phase transition takes place, which is a qualitative change. Extrapolating the trends shown in Figure 5.2 to 77 K yields transfer efficiencies of a maximum of 100 % for 2AP/A & 2AP/T (assuming efficiency does not decrease with temperature once 100 % efficiency is reached), and ~80 % for 2AP/G were found using the data from the present work. There are consistent overestimates of energy transfer efficiency compared to those at 77 K in Table 5.1 reported previously by McKenzie. This may

indicate a qualitative difference in the energy transfer process due to the change in phase, as mentioned in the introduction.

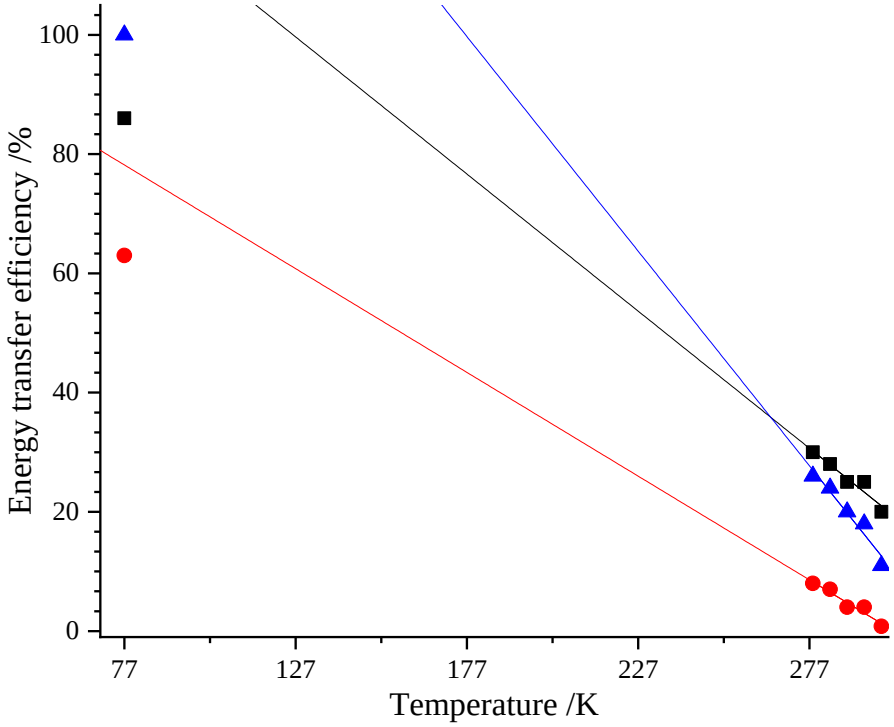

Figure 5.2: Energy transfer efficiency of 2AP-X dinucleotides from time-resolved fluorescence measurements with temperature. Points plotted at 77 K represents previous results from McKenzie.[10] Data plotted: 2AP/G (red circles), 2AP/T (blue triangles), 2AP/A (black squares).

It is also important to consider the fluorescence lifetime data from which energy transfers at 77 K were obtained, where only two fluorescence lifetime components were observed.[10] Both of these components have similar lifetimes to those seen for the two longest components of 2AP-containing dinucleotides in water. Generally, DNA is considered to exist in a variety of conformations, with a complex PES and multiple energy minima. Longer fluorescence lifetimes are interpreted as conformations with limited interaction between 2AP and the natural bases, such as extrahelical 2AP with minimal interactions between 2AP and adjacent natural bases. However, extrahelical conformations are not consistent with energy transfer, and the fluorescence lifetime components reported by McKenzie for direct and indirect excitation are almost identical. The only plausible explanation, in this context, is that only dinucleotide conformations conducive to energy transfer exist at 77 K, while simultaneously non-radiative quenching processes are suppressed. Somsen *et al*[32] showed that at least two states were temperature dependent, and proposed that the lifetimes of these states are dependent on excited state dymanics, which are also

reported as the quenched states in the authors' three-state model. There are two consequences arising from this. First, that not only does energy transfer become more efficient as temperature decreases, fluorescence quenching becomes less efficient. Second, that excited state processes, and by extension energy transfer, are dependent on DNA conformation, which in turn is affected by temperature (at extremes, by phase changes precipitated by large temperature changes).

5.5 Conclusions

It was found that there is a clear temperature dependence in solution of electronic energy transfer between the natural bases and 2AP in 2AP-containing dinucleotides. This trend was shown to be somewhat consistent with previous measurements at 77 K in LiCl,[10] suggesting the observed linear increase in energy transfer efficiency presented in this chapter continues even after the formation of the solid-like "glass" state at lower temperatures. However, it should be noted that the extrapolated energy transfer efficiencies are higher than those shown in the previous work, which may be related to the change in excited state decay kinetics shown by McKenzie. Overall, the explanation offered by Somsen *et al*[32] is reasonably consistent with the observed trend of changing conformational populations of DNA with decreased temperature that favours energy transfer shown here. More importantly, the change in energy transfer efficiency with temperature in the solution phase showed that DNA conformation is affected by temperature even without a phase change. These findings provide further confirmation that energy transfer within DNA is enhanced by the loss of conformation flexibility as a consequence of reduced temperature.

5.6 References

1. P. G. Unna, *The histopathology of the diseases of the skin*, Edinburgh : Clay, Edinburgh, 1896.
2. V. O. Melnikova and H. N. Ananthaswamy, *Mutation Research/Fundamental and Molecular Mechanisms of Mutagenesis*, 2005, **571**, 91-106.
3. R. B. Setlow and J. K. Setlow, *P Natl Acad Sci USA*, 1962, **48**, 1250-1257.
4. N. N. Shafranovskaya, E. N. Trifonov, Y. S. Lazurkin and M. D. Frank-Kamenetskii, *Nature New Biology*, 1973, **241**, 58-60.
5. M. Guéron, J. Eisinger and R. G. Shulman, *The Journal of Chemical Physics*, 1967, **47**, 4077-4091.
6. J. P. Ballini, P. Vigny, G. Thomas and A. Favre, *Photochemistry and Photobiology*, 1976, **24**, 321-329.
7. S. Georghiou, S. Zhu, R. Weidner, C. R. Huang and G. Ge, *Journal of Biomolecular Structure and Dynamics*, 1990, **8**, 657-674.
8. M. Guéron, R. G. Shulman and J. Eisinger, *Proceedings of the National Academy of Sciences*, 1966, **56**, 814.
9. D. G. Xu and T. M. Nordlund, *Biophysical Journal*, 2000, **78**, 1042-1058.
10. G. McKenzie, University of Edinburgh, 2017.
11. T. M. Nordlund, *Photochemistry and Photobiology*, 2007, **83**, 625-636.
12. S. D. Camillis, J. Miles, G. Alexander, O. Ghafur, I. D. Williams, D. Townsend and J. B. Greenwood, *Physical Chemistry Chemical Physics*, 2015, **17**, 23643-23650.
13. H. Kang, K. T. Lee, B. Jung, Y. J. Ko and S. K. Kim, *Journal of the American Chemical Society*, 2002, **124**, 12958-12959.
14. L. Serrano-Andrés, M. Merchán and A. C. Borin, *Proceedings of the National Academy of Sciences*, 2006, **103**, 8691-8696.
15. A. A. Lamola, *Biochemical and Biophysical Research Communications*, 1971, **43**, 893-898.
16. T. Douki and J. Cadet, *Biochemistry*, 2001, **40**, 2495-2501.
17. S. E. Freeman, R. W. Gange, J. C. Sutherland and B. M. Sutherland, *Photochemistry and Photobiology*, 1987, **46**, 207-212.
18. J. R. Lakowicz, *Principles of Fluorescence Spectroscopy*, Springer, 3rd edn., 2006.
19. C. Hélène, P. Douzou and A. M. Michelson, *Proceedings of the National Academy of Sciences*, 1966, **55**, 376.
20. J. Eisinger and R. G. Shulman, *Journal of Molecular Biology*, 1967, **28**, 445-449.
21. D. Markovitsi, D. Onidas, T. Gustavsson, F. Talbot and E. Lazzarotto, *Journal of the American Chemical Society*, 2005, **127**, 17130-17131.
22. E. R. Bittner, *The Journal of Chemical Physics*, 2006, **125**, 094909.
23. D. Markovitsi, T. Gustavsson and F. Talbot, *Photochemical & Photobiological Sciences*, 2007, **6**, 717-724.
24. A. Trifonov, M. Raytchev, I. Buchvarov, M. Rist, J. Barbaric, H. A. Wagenknecht and T. Fiebig, *The Journal of Physical Chemistry B*, 2005, **109**, 19490-19495.

25. C. Curutchet and A. A. Voityuk, *Angewandte Chemie International Edition*, 2011, **50**, 1820-1822.

26. C. Curutchet and A. A. Voityuk, *Chemical Physics Letters*, 2011, **512**, 118-122.

27. A. Czader and E. R. Bittner, *The Journal of Chemical Physics*, 2008, **128**, 035101.

28. A. Olaya-Castro and G. D. Scholes, *International Reviews in Physical Chemistry*, 2011, **30**, 49-77.

29. B. E. Y. M. and J. A. C., *ChemPhysChem*, 2008, **9**, 1121-1129.

30. J. Kent, unpublished work.

31. A. C. Jones and R. K. Neely, *Q Rev Biophys*, 2015, **48**, 244-279.

32. O. J. G. Somsen, L. B. Keukens, M. N. de Keijzer, A. van Hoek and H. van Amerongen, *ChemPhysChem*, 2005, **6**, 1622-1627.

Chapter 6 The Fluorescence of Pentacyclic Adenine In the Presence of the Natural Bases

"The scientist is not the person who always gives the right answers, he is the one who always asks the right questions."

Claude Levi-Strauss

6.1 Introduction

In recent years a number of different fluorescent base analogues (FBAs) have been presented in the literature, which exhibit certain desirable, improved photophysical properties, such as longer emission/excitation wavelengths or increased brightness. One such base analogue is pentacyclic adenine (pA, Figure 6.1), which first appeared in a publication[1] early in 2018. The effect of interaction with the natural bases on the fluorescence properties of pA will be the focus of this chapter.

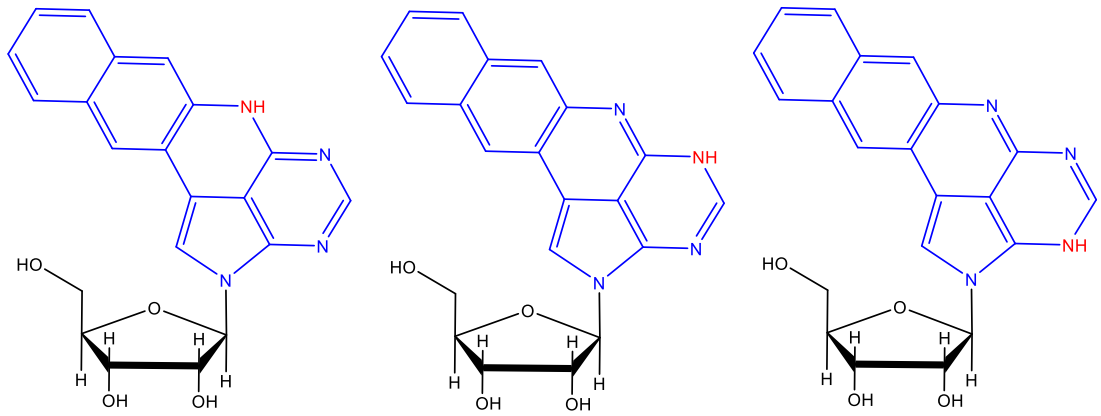

Figure 6.1: Molecular structure of pentacyclic adenine riboside tautomers, pentacyclic adenine moiety highlighted in blue.

Bood *et al*[1] first presented the molecular structure of pA, which is one example of a family of FBAs derived from adenine by adding fused phenyl rings, and compared it to a selection of existing FBAs. The authors then proceeded to tabulate its intrinsic photophysical properties (such as peak absorbance wavelengths and fluorescence quantum yield) both as the free monomer and in DNA, in comparison with a series of previously known FBAs, including 2-aminopurine (2AP), which is discussed at considerable length in Chapter 4. A value of 387 nm is given for the absorption wavelength of pA, which is longer than that for 2AP as well as all the other FBAs listed, while 420 nm is reported for the emission wavelength, which is longer than that reported for 2AP, but overall is close to the median value. The fluorescence quantum yield (66%) is similar to 2AP and is among the highest of the analogues presented by Bood *et al*, with only 2AP (68%) and 6MI (70%) showing higher quantum yields. However, the stand-out property of pA is its fluorescence brightness, which is the product of the extinction coefficient and the quantum yield. For the results presented in the previous work, in the monomer form pA has easily the greatest fluorescence brightness 10100 M^{-1} cm^{-1}, while in double stranded DNA it is the second brightest

(1400 M^{-1} cm^{-1}). In addition, pA has the highest two-photon cross-section (a proxy for the probability of two-photon absorption occurring, analogous to the extinction coefficient for conventional one-photon excitation) of any known FBA, with greater photostability for two-photon excitation than for conventional one-photon excitation. More recent work by Fisher *et al*[2] raised the potential of two-photon excitation of pA being used for single molecule measurements, among other advantages inherent in two-photon techniques, but this falls outside the scope of the current work and will not be discussed further.

A closer look at the fluorescence properties of pA, particularly fluorescence decay parameters from time-resolved measurements, is provided in the PhD thesis of Rachel Fisher.[3] In contrast to 2AP riboside, which has a single lifetime of 10.6 ns,[4] monomeric pA riboside (pAr) was found in the previous work to have two fluorescence lifetimes in PBS of 190 ps and 5.97 ns, with A-factors of 0.35 and 0.65, respectively. It is important to draw a distinction here between the free base form and the riboside of a FBA, particularly for 2AP and pA. In the case of 2AP as a free base, two tautomers exist in aqueous solution, which results in two similar but distinct fluorescence lifetimes, as discussed elsewhere in this work. Once a riboside moiety is attached to 2AP, only one tautomer exists and true single exponential decay is observed.[4] A similar process is likely for pA, which can be seen upon inspection of the pA structure shown in Figure 6.1 earlier. However, three tautomers are still possible for pAr, even with a riboside sugar attached to the amine within the five-membered ring. This complicated fluorescence decay behaviour seen for pAr makes an analysis of the type discussed in Chapter 4 more difficult, if not impossible.

Unlike 2AP, which exhibits a clearer dependence of its photophysics on the identity of the neighbouring base,[5] pA displays a more complex relationship with the identity of the surrounding bases. It is reasonable to point out that the previous study by Bood *et al*[1] of interest in this chapter looks at longer decamer oligonucleotides rather than dinucleotides as is the case for 2AP, but some conclusions can still be drawn, particularly if the assumption is made that only the bases immediately adjacent to pA are significant. In the study under consideration, 16 oligonucleotides were included, that cover the full set of possible combinations of adjacent bases (given that order is important, e.g. AC is not the same as CA, and four distinct natural bases in two positions gives 16 (4^2) combinations). Positioning pA 5’ or 3’ in an

oligonucleotide induces large changes in its quantum yield with factors of two or more, for example oligonucleotides with adjacent bases GT and TG arranged 5' to 3' have quantum yields for pA of 8.3 % and 3.3 %, respectively. Moreover, focusing on the oligonucleotides where the identity of both adjacent bases is the same, in order of decreasing quantum yield the series AA (58 %), GG (28 %), CC (3.6 %), TT (2.6 %) is obtained. Comparing a selection of mixed oligonucleotides such as CT (4.1 %), which has a higher quantum yield than both CC and TT; and TC (2.4 %), which has a lower quantum yield than either CC or TT, on the face of things, it becomes clear that the quantum yield observed is not simply the sum of the separate effects of the neighbouring bases on the fluorescence of pA. It is important to point out two effects: (1) that pA undergoes significant photobleaching during traditional one-photon excitation, which would have added a significant source of uncertainty to the quoted quantum yield values in the previous work; and (2) quenching due to the natural bases would also act as a protection against photobleaching, all three of which (fluorescence, quenching, and photobleaching) compete as decay pathways.

For these reasons, time-resolved fluorescence measurements are useful in supplementing the steady-state data in understanding the photophysical processes taking place in pA-containing oligonucleotides. Unfortunately, due to the time-consuming and expensive nature of time-resolved fluorescence measurements, data for the full set of 16 oligonucleotides discussed earlier are not available, but the lifetime data of the oligonucleotides that have been measured are shown in Table 6.1 below. The behaviour is complex, and it may not be possible to draw definitive conclusions from these data alone, but a number of interesting patterns can be extracted. For example, there is not necessarily a clear qualitative shift observable going from free pAr to pA-containing oligonucleotides, with either two or three lifetime components seen for both oligonucleotides and free pAr. In contrast, r2AP in solution shows only a single lifetime, with extra lifetime components only appearing in the presence of the natural bases. The somewhat variable nature of the pA decay parameters in Table 6.1 is consistent with the previous discussion about the greater complexity of the dependence of the observed fluorescence emission intensity of pA on the sequence context, not merely the identity of the neighbouring bases but their ordering as well.

	τ_1 /ns	τ_2 /ns	τ_3 /ns	A_1	A_2	A_3	$\langle\tau\rangle$/ns
pAr	5.97	-	0.19	0.65	-	0.35	3.95
GG	7.48	2.14	0.55	0.29	0.15	0.56	2.80
GA	7.24	-	0.89	0.50	-	0.50	4.09
AA[a]	7.58	1.37	-	0.69	0.31	-	5.68
AT	6.72	1.61	0.16	0.20	0.24	0.56	1.81
TT	3.96	0.80	0.10	0.05	0.13	0.82	0.38
CC	3.57	0.78	0.20	0.02	0.29	0.69	0.45

Table 6.1: Time-resolved fluorescence decay parameters of free pA and pA-containing single-stranded oligonucleotides in PBS solution. An excitation wavelength of 390 nm was reported, with A-factors from an emission wavelength of 430 nm. Lifetimes and A-factors ordered from longest lifetime to shortest. Oligonucleotides labelled by the bases immediately adjacent to pA. Table reproduced from data in reference 3 and (a) from unpublished work by Rachel Fisher.[6]

In a similar fashion to the approach taken for interpretation of the 2AP decay parameters, assuming that lifetime components falling within a similar range represent equivalent interactions or conformational states may provide a useful handle for rationalising the data previously reported. It appears that the lifetime components of pA can largely be grouped into four distinct ranges, at around 0.1-0.2 ns, 0.5-0.9 ns, 1-4 ns, and 6-8 ns. Of these, free pAr has two lifetime components that fall into the longest and shortest lifetime groups, while all the oligonucleotides reported have at least one intermediate lifetime. Taken at face value, this could suggest the intermediate lifetime component for pA in oligonucleotides is a product of the interactions between pA and the adjacent bases.

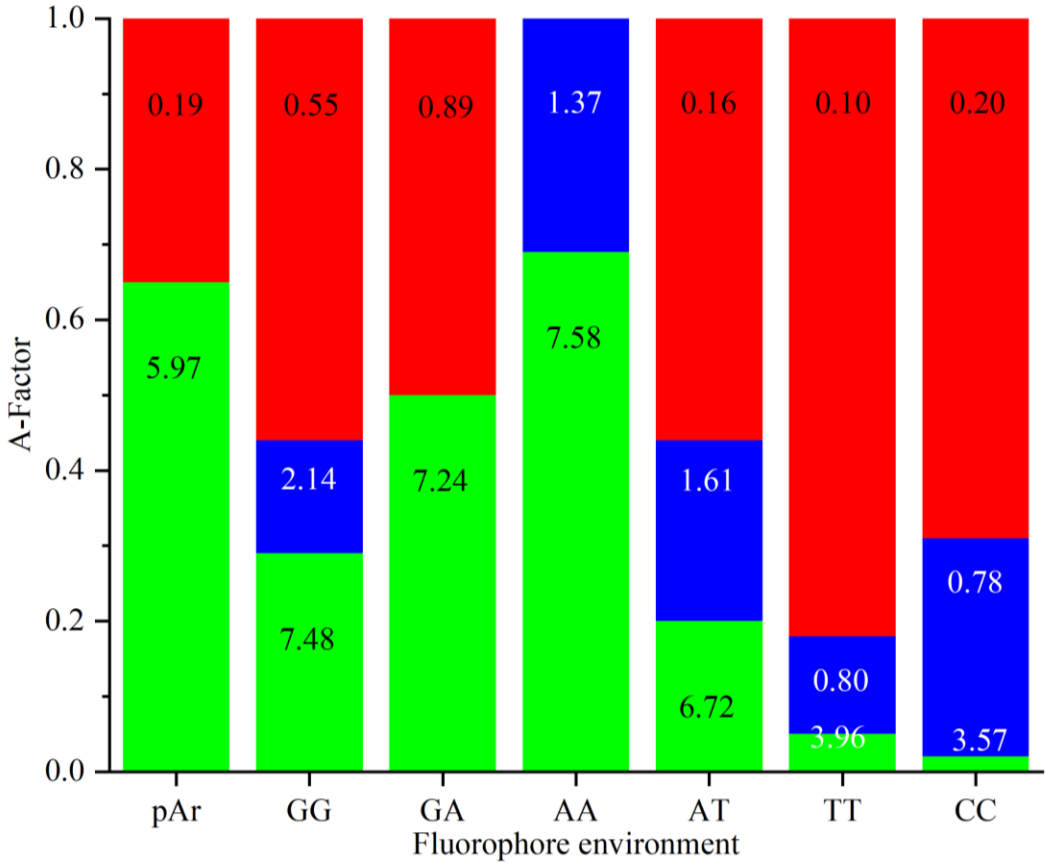

Figure 6.2: Graphical representation of time-resolved fluorescence data in Table 6.1 of pAr and pA-containing single-strand oligonucleotides.[3, 6] Lifetime data shown: τ_1 (green); τ_2 (blue); τ_3 (red).

Following the logic for quenching of 2AP fluorescence set out in Chapter 4, the longest lifetime represents unstacked or poorly stacked conformations, while the shorter lifetimes represent more highly stacked structures, but as noted previously the more complex multi-exponential decay of free pAr in the absence of any natural DNA bases, whether in an oligonucleotide structure or not, renders such a straightforward explanation invalid. Another distinction between 2AP and pA is that in oligonucleotides, the number and magnitude of lifetime components observed for 2AP shows little variation; there are almost always four lifetime components with similar magnitudes for corresponding lifetime components across oligonucleotides (although the A-factors do vary considerably). However, pA decay parameters are highly dependent on sequence context, not just for the A-factors, but the lifetime components as well. In addition to the intermediate lifetimes, all the oligonucleotides with a purine base at the 5' position are shown to have a lifetime component within the longest 6-9 ns range, while the oligonucleotides with a pyrimidine base at the 3' have a lifetime component within the 0.1-0.2 ns range. This does not appear to be mutually exclusive,

as evidenced by the reported values for AT. In general, pyrimidine bases appear to produce shorter fluorescence lifetime components from pA, while purine bases seem to elicit longer lifetime components from pA, which can also be seen from the number-averaged lifetimes. A visual illustration of this is shown in Figure 6.2, where both the shortest (which represents 50 % or more of the total emitting population in the oligonucleotides) and longest lifetime component appear for free pAr, as well as (almost) all the oligonucleotides. However, the intermediate component only appears for pA-substituted oligonucleotides.

GA and AA appear to be anomalous, with only two lifetime components, suggesting that adenine is responsible for the observed anomaly. Confusingly, AT contradicts this finding, with three lifetime components observed, suggesting there is an additional factor. One key difference is the location of adenine at the 5' position for AT and not the 3' position, as it is for both GA and AA. This may also explain why GA exhibits the shortest and longest lifetime component, while for AA with adenine at both 3' and 5' positions the intermediate component is observed, rather than the very short component. The resulting increased proportion of the longest lifetime component very likely explains why the average lifetime for GA and AA is even higher than for free pAr, which is somewhat inconsistent with the fluorescence quantum yield mentioned previously, given that the number-average lifetime is generally proportional to the quantum yield. An increase in the average lifetime relative to free pAr therefore also implies a similar rise in the quantum yield, which does not appear to be the case here for any of the oligonucleotides reported. However, as already mentioned, free pA in solution undergoes very rapid and severe photobleaching, a point Bood *et al*[1] mentioned briefly but did not address in the context of their reported quantum yield data, so there is a question about the accuracy of the reported data, especially for free pAr. Typically, a reduced fluorescence lifetime results in a reduced rate of photobleaching, because photochemical processes which are most often the cause of photobleaching have less time to occur before radiative decay (fluorescence) takes place. This suggests that oligonucleotides with a short average lifetime, such as CC, TT, AT and even GG, may have a reduced rate of photobleaching and therefore the quantum yields quoted for these in the previous work by Bood *et al*[1] are more likely to be reliable, in inverse proportion to the magnitude of their average lifetimes. In contrast, GA and AA have a longer average lifetime than free pAr, which indicates

that photobleaching may have an even greater effect on pA in these oligonucleotide sequences than on free pAr. Conversely, it is fair to point out that free pAr in solution will be more accessible to photochemical attack, which is likely also an important factor, but it should be borne in mind that the measurements in the current discussion were obtained for single-strand oligonucleotides, with pA still somewhat accessible to photochemical processes without a complementary hydrogen-bonded partner. In short, GA and AA are likely to experience a greater rate of photobleaching than free pAr, which is somewhat counter-intuitive, but nevertheless is consistent with the observed discrepancy between the relevant quantum yields and average lifetimes. This further supports the earlier statement about the utility of time-resolved fluorescence measurements, perhaps not completely replacing steady-state fluorescence measurements, but certainly complementing them.

Examining the previous reports discussed in this section, it suggests that the identity of the neighbouring base(s) is not the only significant factor determining the fluorescence output of pAr. Positioning a base at the 3' or 5' position of pA clearly creates quantitatively different impacts on the fluorescence of pA, which is most likely due to the base sequence changing the way the natural bases stack with pA. It has been shown previously in Chapter 4 of this thesis that 2AP is affected by base stacking, and that base stacking of FBAs with the natural bases may occur for the free bases, without the sugar-phosphate backbone, and can be observed and even quantified. This chapter reports the application of a similar approach to pAr; the interaction of free pAr in solution with the natural bases has been investigated, without the complication of multiple distinct natural bases being present, or the effect of DNA backbone structure. This has allowed any changes in fluorescence to be ascribed with more certainty to the identity of the interacting base. This work has focused on time-resolved fluorescence measurements, in order to overcome the problem with photobleaching mentioned throughout this introduction. Fluorescence lifetime measurements of free pAr as a function of the concentration of the monophosphate nucleotides are presented for each of the canonical bases.

6.2 Experimental

Adenosine-5'-monophosphate disodium salt (Sigma, 99%); Cytidine-5'-monophosphate disodium salt (Sigma, 99%); Deoxythymidine-5'-monophosphate disodium salt (Abcam, 98%); Ethylenediaminetetraacetic acid (Calbiochem);

Guanosine-5'-monophosphate disodium salt (Acros Organics, 97%); Tris-hydrochloride (Fisher, 1M); Water (Fisher, HPLC grade) were all used as received without further purification. Pentacyclic adenine riboside (pAr) was used as received from Prof. Marcus Wilhelmsson at Chalmers University of Technology.

Time-resolved fluorescence measurements of pAr (~1 μM) were carried out in tris-HCl buffer (20 mM tris-HCl, 60 mM NaCl, 0.1 mM Na_2EDTA) at room temperature in the presence of each of the canonical nucleoside monophosphates. An excitation wavelength of 390 nm was used and decay curves were measured with an emission wavelength of 420 nm.

Geometry optimisation, frequency and TDDFT calculations were carried out on the pAr tautomers shown in Figure 6.1, using the M06-2X/6-31+G* functional and basis set in Gaussian 16 on the Eddie cluster.

6.3 Results

The fluorescence decay of pAr alone was found to show that three lifetime components, as shown in Table 6.2. This contradicts the previous study that reported pAr with only two lifetime components,[3] but fitting two lifetime components did not appear to adequately represent the data obtained in the present work. It is significant, however, that the additional component has a much smaller A-factor. As shown in Figure 6.3, a small deviation (between 0 and 25 ns) appears in the residuals for a 2-component fit (b), which disappears when three components (c) are fitted. There is also a small decrease in the χ^2 going from two components (1.091) to three components (1.006), a further indication that fitting three lifetime components yields a better representation of the data. Lifetime and A-factor values obtained from fitting two or three components are shown in Table 6.2, where fitting two components gives similar values to the previous work, although the average lifetime is slightly higher, but the quality of the fit is less than ideal, for the reasons already stated. Also significant is the fact that the lifetime components common to both 2- and 3-component fits do not vary

pAr fit	τ_1 /ns	τ_2 /ns	τ_3 /ns	A_1	A_2	A_3	$\langle\tau\rangle$/ns
2-component	6.00	-	0.21	0.66	-	0.34	4.01
3-component	6.15	3.53	0.17	0.58	0.06	0.36	3.85

Table 6.2: Separate 2-component and 3-component exponential fitting to pAr (~1 μM) fluorescence decay data in 20 mM tris-HCl buffer.

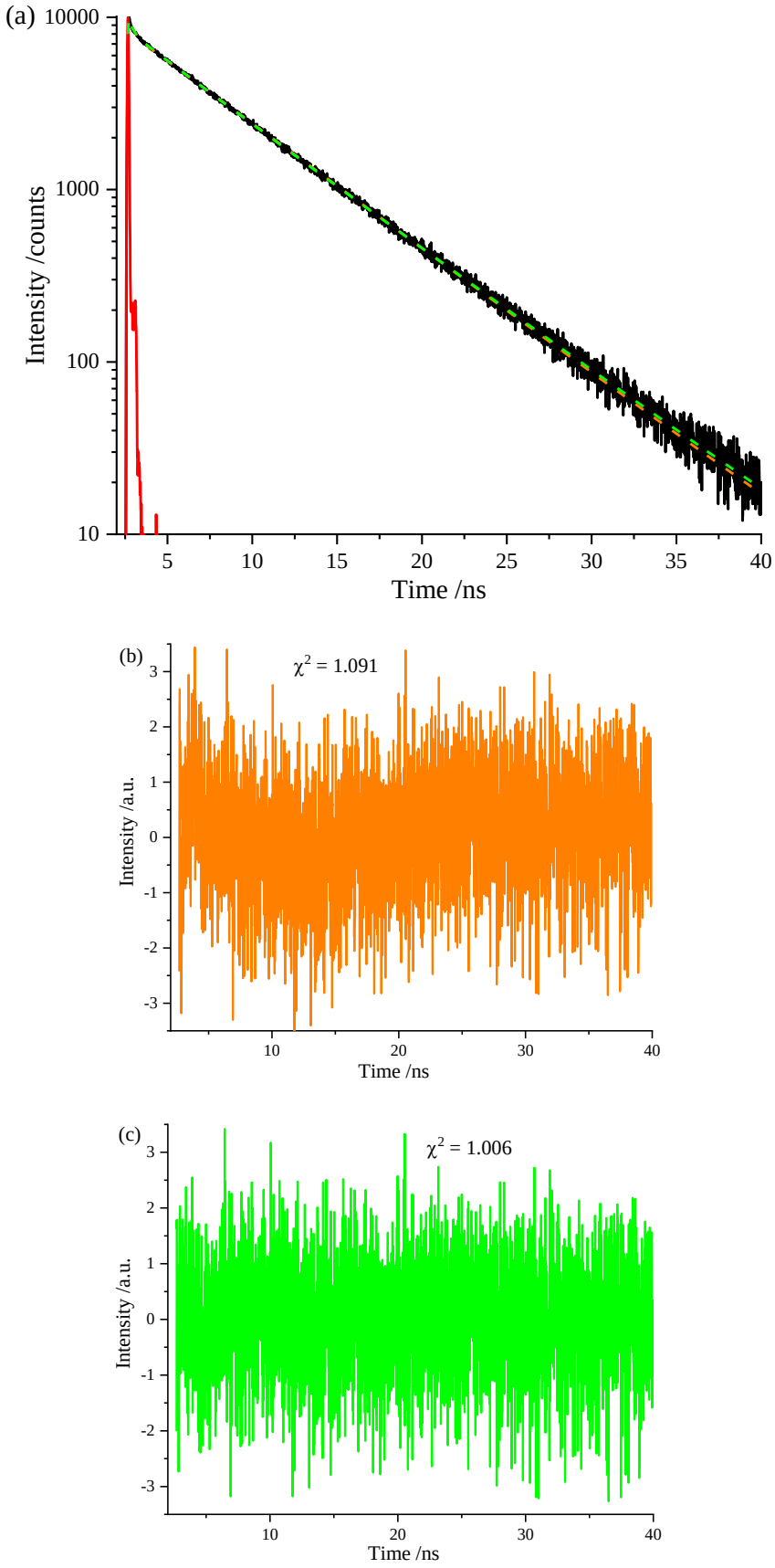

Figure 6.3: (a) Fluorescence decay of pA (black, solid) with the IRF (red, solid) fitted with 2 lifetime components (orange, dashed) and 3 lifetime components (green, dashed) separately. Residuals from (b) 2-component fit and (c) 3-component fit.

significantly, which is reflected in the limited decrease in the average lifetime, despite the appearance of a new intermediate lifetime component, which accounts for a much smaller proportion of the total emitting population than the other two components. It is possible that this second component is just an artefact of the fitting process, but there is also sufficient difference in magnitude between the three lifetime components that a third lifetime could have been resolved by the TCSPC setup used. It is also reasonable to assume that distinct tautomers appear as separate excited state species, as has been well established for other base analogues such as 2AP.[4] Examining the structure of pAr in Figure 6.1, where as previously noted in the introduction, three tautomers are possible *via* proton exchange between the three remaining nitrogen atoms within the fused aromatic ring system. Therefore, three lifetime components were fitted to the data in this chapter, although there is reasonably some question about the correct number of components, as there typically is for multi-exponential curve fitting.

From the results of calculations performed on the three pAr tautomers identified in Figure 6.1, free energies were obtained with a range of 59 $kJ.mol^{-1}$ between the highest and lowest energy tautomers. These energies give relative populations of 0.99, $1.43x10^{-6}$, and $4.30x10^{-11}$ for each of the distinct tautomers. Such proportions are clearly wildly inconsistent with the proportion of each emitting species in Table 6.2, but there are a number of caveats to this data. First, the resulting populations depend entirely on the accuracy of the calculated energies, a higher level of theory than DFT may give more accurate and reliable results. Second, these are the ground state tautomer populations, whereas the A-factors from TCSPC relate to the populations of the excited state emitting species. These emitting populations depend on any interconversion processes between the various excited tautomers, as well as the likelihood of excitation from individual ground state tautomers to the relevant excited state following photon absorption. More relevant information was obtained from time-dependent calculations by comparing oscillator strengths of the transition to the first excited state, shown in Table 6.3. The oscillator strengths imply one tautomer (pA2) has a lower likelihood of transition to the excited state than the other two, which is consistent with the observed emitting populations, although the previous caveat about calculation accuracy also applies here.

	pA1	pA2	pA3
Free energy /kJ.mol-1	-3492465	-3492439	-3492406
Population	0.99999	1.4324E-06	4.29966E-11
Oscillator strength	0.4376	0.3537	0.4615

Table 6.3: Results from DFT calculations on pAr tautomers using functional and basis set M06-2X/6-31+G* in Gaussian 16. Oscillator strengths from TD-DFT, populations and free energies from frequency calculations.

Previous literature reports[4] for the more well-studied FBA 2AP demonstrated that the existence of tautomers in solution leads a corresponding increase in the number of fluorescence lifetime components. A plausible explanation is that three lifetime components appear in the data due to the presence of three distinct tautomers, and will form a key assumption for the current work.

The fluorescence decay parameters measured for pAr in the presence of rAMP, as a function of rAMP concentration, are given in Table 6.4 below. These results are quite consistent with the lifetime data for pA-containing oligonucleotides from previous work[3, 6] reproduced in Table 6.1 earlier. In retrospect, it seems obvious that there should be an extra lifetime component for pAr in the presence of rAMP, based on the fact that the shortest lifetime component disappears for pAr sandwiched between two adenine bases in an oligonucleotide structure. There is no immediately obvious process that could block the fastest decay pathway for pA in an oligonucleotide but not for pAr in solution. Both the longest and shortest lifetime components exhibit a clear increasing trend with rAMP concentration, while the intermediate lifetime is more complicated and appears to oscillate around a median value, if the decay curves are fitted separately. In contrast, when global analysis is used, linking the value of the intermediate lifetime component across all decay curves, the values shown in Table 6.4 were obtained. Fitting the data using global analysis does lead to an increased χ^2 of 1.01 over all fitted curves, however considering that an extra constraint is applied, an increase is not unreasonable, and the χ^2 value is still within the historical range of χ^2 values typically seen for data obtained from the experimental setup used in this work. In addition, the graph of residuals obtained from the global fitting were similar to those shown for the 3-component fitting in Figure 6.3c earlier. Linking both the A-factor A_2 and the lifetime τ_2 of the intermediate component across all decay curves was attempted, but poor quality fits were obtained ($\chi^2 > 1.2$). It is possible that the population of the emitting species represented by the intermediate component is highly sensitive to environmental conditions, such as

temperature (which wasn't controlled during these measurements), or that the relatively small proportion of the intermediate component increases the relative uncertainty. Separate fitting of the decay curve of free pAr is shown for purposes of comparison with the globally fitted lifetimes. There is some evidence that there was a larger uncertainty in the value of τ_2 than for the other lifetime components as a result of its small population, which can be seen by comparing the different values obtained for each of the datasets already presented and those to be presented shortly in this section.

[rAMP] /M	τ_1 /ns	τ_2 /ns	τ_3 /ns	A_1	A_2	A_3	$<\tau>$/ns
0[a]	6.15	3.53	0.17	0.58	0.06	0.36	3.85
0	6.19	3.95	0.17	0.56	0.08	0.36	3.85
$1x10^{-5}$	6.15	3.95	0.16	0.58	0.06	0.36	3.85
$5x10^{-5}$	6.15	3.95	0.17	0.59	0.06	0.35	3.89
$1x10^{-4}$	6.18	3.95	0.17	0.59	0.07	0.34	3.99
$5x10^{-4}$	6.22	3.95	0.18	0.60	0.07	0.33	4.07
$1x10^{-3}$	6.25	3.95	0.18	0.61	0.07	0.32	4.17
$5x10^{-3}$	6.49	3.95	0.23	0.64	0.07	0.29	4.50
0.01	6.65	3.95	0.25	0.64	0.07	0.28	4.63
0.02	6.83	3.95	0.27	0.65	0.06	0.29	4.73
0.03	6.96	3.95	0.29	0.65	0.06	0.29	4.87
0.04	7.06	3.95	0.31	0.66	0.06	0.28	4.98
0.05	7.11	3.95	0.32	0.66	0.06	0.28	4.99

Table 6.4: Fluorescence lifetimes of pAr as a function of the concentration of rAMP concentration in tris-HCl buffer (20 mM). Values obtained from global analysis of data, with a common value τ_2 for all decays. (a) from separate fitting of free pAr decay data.

Globally fitting all of the free pAr decay curves measured in each separate set of data results in the values shown in Table 6.5, where each lifetime component is linked across all spectra. No obvious pattern of deviation was observed in the residuals of the fitted decay curves. Fluorescence lifetime components obtained in this way, particularly the intermediate component, are reasonably consistent with the lifetime components of free pAr presented in Table 6.2 previously, in contrast to the data that will be examined in a moment.

As noted previously, three tautomers exist for pAr, so it is probable that the intermediate component merely represents a tautomeric species with a low population. However, there is an alternative plausible explanation, that there is a fluorescent impurity as a result of photobleaching over the course of each measurement. It has been shown previously[1] that pA exhibits very severe photobleaching, and each decay measurement using the experimental setup described earlier takes a minimum of ~10 minutes. This is somewhat less plausible when the subsequent reduction in steady-state intensity is taken into account, which as already stated is quite severe, suggesting an essentially non-fluorescent species is responsible for the drop in emission intensity. A lifetime of 3-3.5 ns is hardly typical of a non-fluorescent impurity. It should also be noted that the sample used was characterised by high resolution mass spectrometry with a view to using it in fluorescence studies,[1] suggesting no impurity was found. The presence of an intermediate component independently of NMP concentration suggests that any potential impurity did not come from the NMP used. It is, however, impossible to definitively and unconditionally prove an absence of an impurity. Nevertheless, the presence of three tautomers will be assumed in the rest of this chapter.

		A-factors			
Component	Lifetime /ns	pAr-AMP	pAr-CMP	pAr-GMP	pAr-TMP
1	6.19	0.59	0.47	0.30	0.43
2	3.12	0.07	0.09	0.07	0.08
3	0.18	0.34	0.44	0.63	0.49

Table 6.5: Lifetime components linked across all measured pAr decay curves from global fitting. A global χ^2 of 1.074 was obtained. A-factors for each set of data shown separately.

Nevertheless, whatever the nature of the intermediate lifetime component, which only accounts for 6-8 % of the emitting population based on the relevant A-factors, there is a steady increase in the average lifetime $<\tau>$. There are clear, consistent trends for the shortest and longest lifetime components, so linking these values globally was not attempted. The steadily increasing average lifetime appears to be due to the increases in both the shortest and longest lifetime components, as well as the increase in the proportion of the longest lifetime. Furthermore, it does appear that the longest lifetime component and corresponding A-factor, as well as the average lifetime, are not only increasing but are tending with increasing concentration of rAMP towards the corresponding values from previous work for the AA oligonucleotide in Table 6.1 in the introduction.

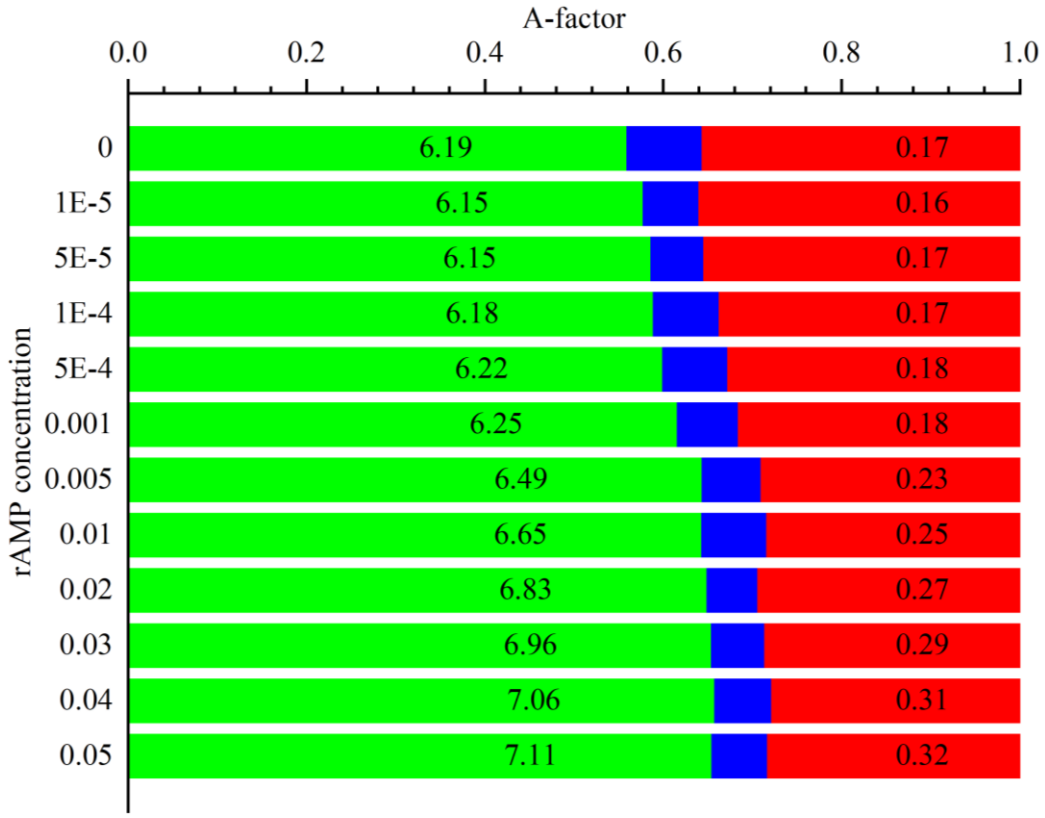

Figure 6.4: Graphical representation of time-resolved fluorescence measurements presented in Table 6.2 of pAr as a function of rAMP concentration in tris-HCl buffer (20 mM). Lifetime data shown: τ_1 (green); τ_2 (blue); τ_3 (red). Lifetimes and A-factors obtained from global analysis across all concentrations, the intermediate component τ_2 (3.95 ns) was kept constant across all decay curves.

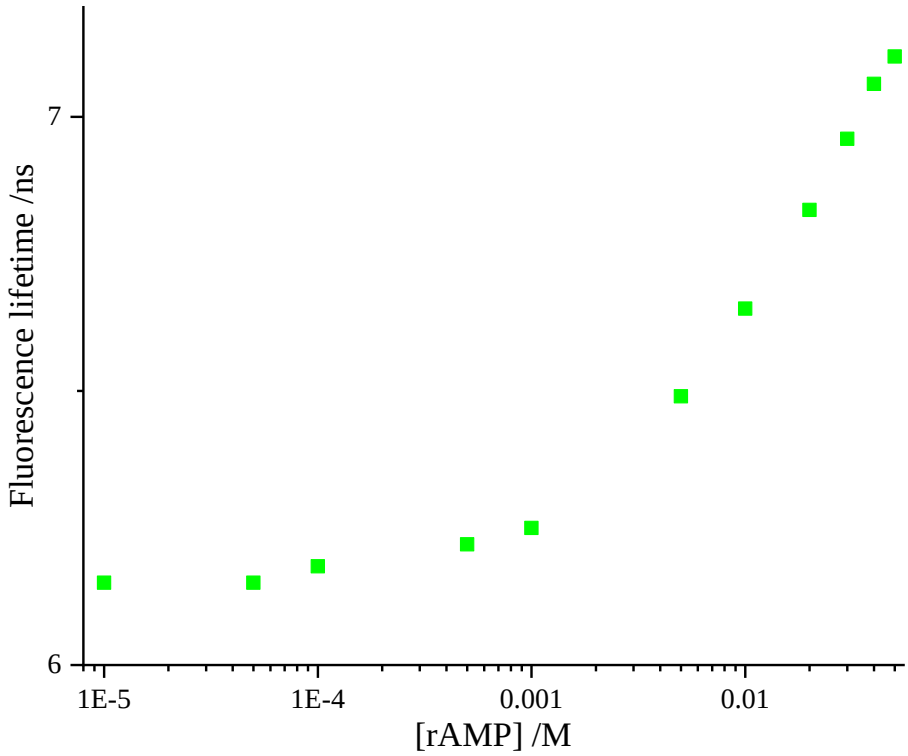

Figure 6.5: Fluorescence lifetime τ_1 from global fitting of decays from pAr in tris-HCl buffer (20 mM) as a function of rAMP concentration.

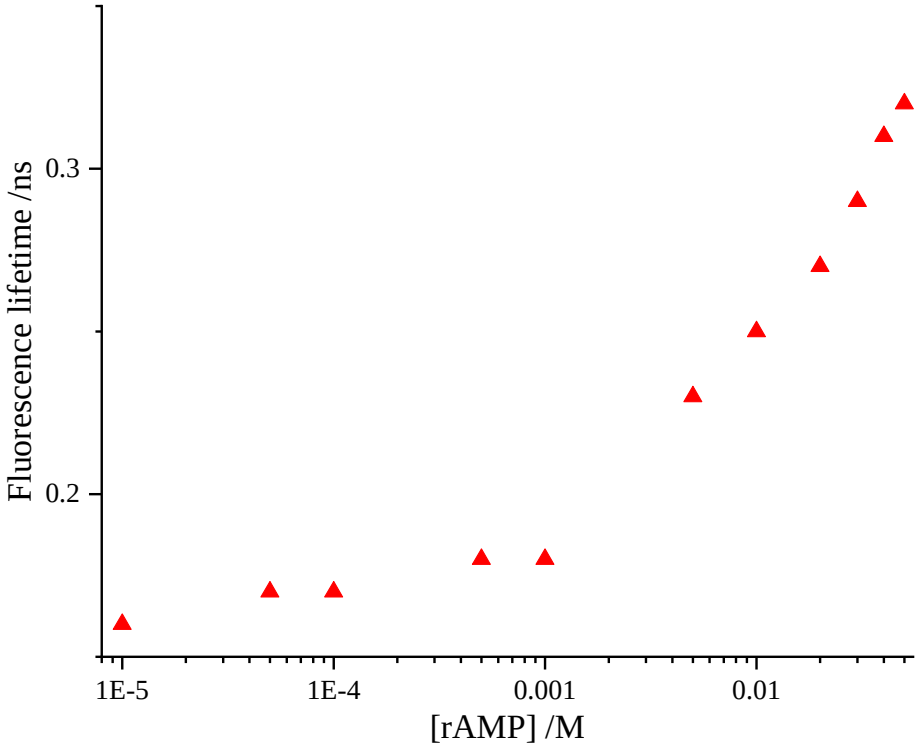

Figure 6.6: Shortest lifetime component from global fitting of decays from τ_3 of pAr in tris-HCl buffer (20 mM) as a function of rAMP concentration.

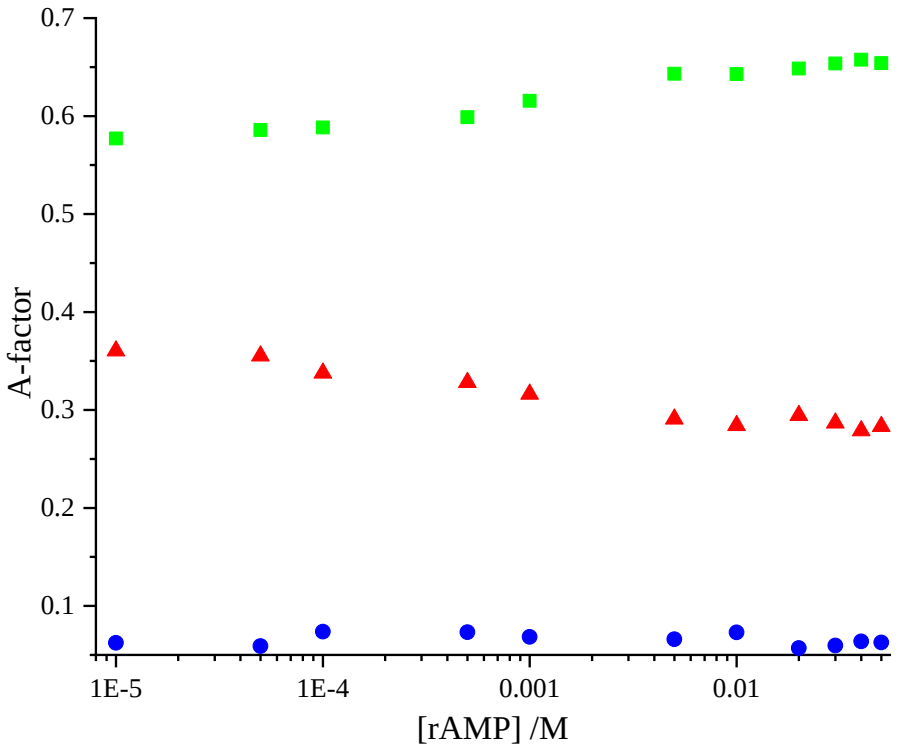

Figure 6.7: Pre-exponential factors (A-factors) of pAr fluorescence lifetime components as a function of rAMP concentration. A-factors shown: A_1 (green squares); A_2 (blue circles); A_3 (red triangles).

Trends in the lifetime data shown in Table 6.1 are presented in Figure 6.4 to Figure 6.7 visually. There appears to be a sharp discontinuity at 1 mM in the shortest and longest lifetime components (Figure 6.5 & Figure 6.6), with the intermediate lifetime fixed. This suggests an additional interaction begins to occur above 1 mM concentration of rAMP, although the fact that the lifetimes increase does not support the same static quenching process due to dimer formation or complexation of pAr with rAMP shown in Chapter 4, but does not rule out dimer formation altogether. It is also significant that the population of the longest lifetime component A_1 increases simultaneously with a decrease in the population of the shortest lifetime A_3. In contrast, the population of the intermediate lifetime A_2 remains relatively constant and does not seem to be affected. Whatever process is taking place as a result of the presence of rAMP, it seems to make the longest lifetime species more favourable. One possible explanation is excited state proton transfer (ESPT) between pA and nearby adenine, which leads to an enhancement of the fluorescence emission with an increased lifetime.[7] This will be discussed in more depth later on.

[rCMP] /M	τ_1 /ns	τ_2 /ns	τ_3 /ns	A_1	A_2	A_3	$\langle\tau\rangle$/ns
0[a]	6.17	2.49	0.17	0.49	0.09	0.42	3.30
0	6.21	2.74	0.17	0.47	0.09	0.44	3.25
$1x10^{-5}$	6.17	2.74	0.16	0.51	0.07	0.42	3.39
$5x10^{-5}$	6.18	2.74	0.17	0.49	0.07	0.44	3.30
$1x10^{-4}$	6.17	2.74	0.16	0.49	0.07	0.44	3.28
$5x10^{-4}$	6.13	2.74	0.16	0.50	0.07	0.43	3.34
$1x10^{-3}$	6.15	2.74	0.17	0.53	0.08	0.39	3.52
$5x10^{-3}$	5.97	2.74	0.18	0.52	0.07	0.40	3.40
0.01	5.79	2.74	0.18	0.49	0.08	0.43	3.14
0.02	5.54	2.74	0.19	0.40	0.11	0.49	2.60
0.03	5.29	2.74	0.21	0.36	0.13	0.51	2.38
0.04	5.07	2.74	0.21	0.33	0.14	0.53	2.17
0.05	4.87	2.74	0.21	0.30	0.14	0.56	1.97

Table 6.6: Fluorescence lifetimes of pAr as a function of the concentration of rCMP concentration in tris-HCl buffer (20 mM). Values obtained from global analysis of data, with τ_2 kept constant for all spectra. (a) from separate fitting of free pAr decay data.

Carrying out global analysis of data for pAr in the presence of rCMP in the same way as for rAMP yields the values shown in Table 6.6 below. As previously

mentioned, the magnitude of the intermediate lifetime varies substantially with pAr lifetime components presented, so the values from separate fitting of the pAr data is shown for comparison. Similar quality of fit was observed for the rCMP data as for rAMP. In contrast to the results seen for the fluorescence output of pAr in the presence of rAMP, rCMP (Table 6.6) induced a decrease in the longest lifetime component of pAr as well as the average lifetime. The A-factor of the longest lifetime component likewise decreased with concentration of rCMP, while the shortest component and its A-factor increased. Average lifetimes were primarily affected by the shortest and longest lifetime components, given that the intermediate lifetime was shown to be constant across all concentrations. Perhaps predictably based on the CC oligonucleotide results from the previous work,[3] the average lifetime decreases with rCMP concentration. Lifetime values for the highest concentrations of rCMP do not all reach similar values as the CC oligonucleotide reproduced in Table 6.1 previously, although they do tend towards the oligonucleotide values, with the exception of τ_2, which is constant.

In Figure 6.8 to Figure 6.10, with results presented for rCMP in a visual manner once again, the trends mentioned can be more easily spotted in detail upon inspection. As for the rAMP results, a change was seen between 1 and 5 mM concentration of rCMP, albeit with a steady decrease, rather than an increase in the magnitude of the longest lifetime component. Lifetimes for the shortest component remained relatively constant, while the lifetime of the intermediate component was fixed across all decay curves. The population of the two shortest lifetime components A_2 and A_3 showed mirror inverse trends to the population of the longest lifetime component A_1. Such observations support complex formation at these concentrations of the type found for 2AP in Chapter 4. The results in Table 6.6 and Figure 6.9 similarly suggest a ground state (static quenching) interaction between pAr and rCMP. Examining the data at lower concentrations of rCMP (<5 mM), there is not much change observed for the lifetimes, although the populations did vary.

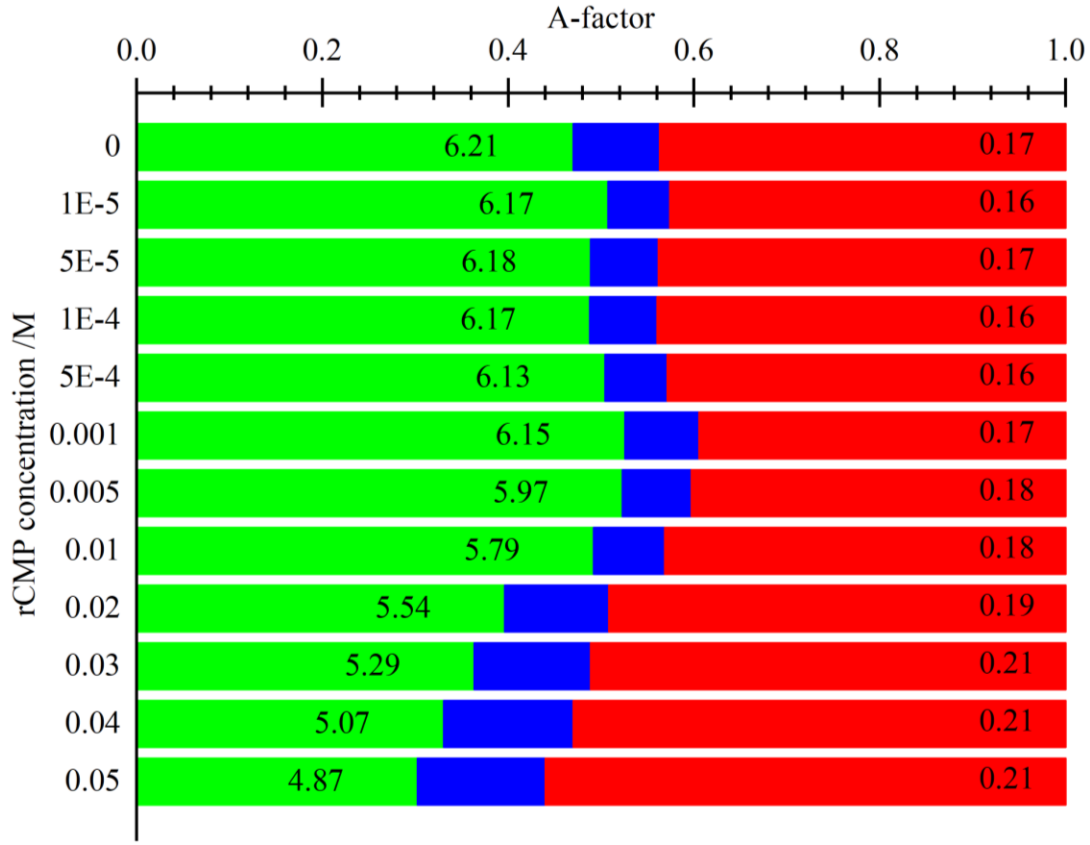

Figure 6.8: Graphical representation of time-resolved fluorescence measurements presented in Table 6.3 of pAr as a function of rCMP concentration. Lifetime data shown: τ_1 (green); τ_2 (blue); τ_3 (red). Lifetime and A-factor values were obtained from global analysis across all concentrations, the intermediate component τ_2 (2.74 ns) was kept constant for all decay curves.

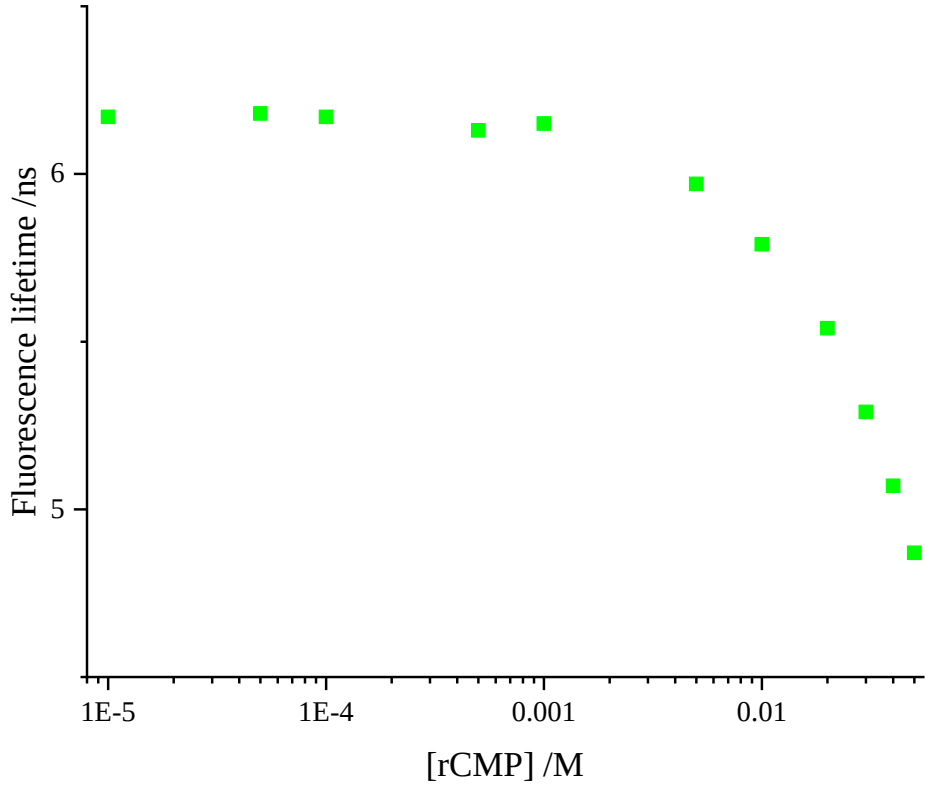

Figure 6.9: Fluorescence lifetime of longest component τ_1 for pArr in tris-HCl buffer (20 mM) as a function of rCMP concentration.

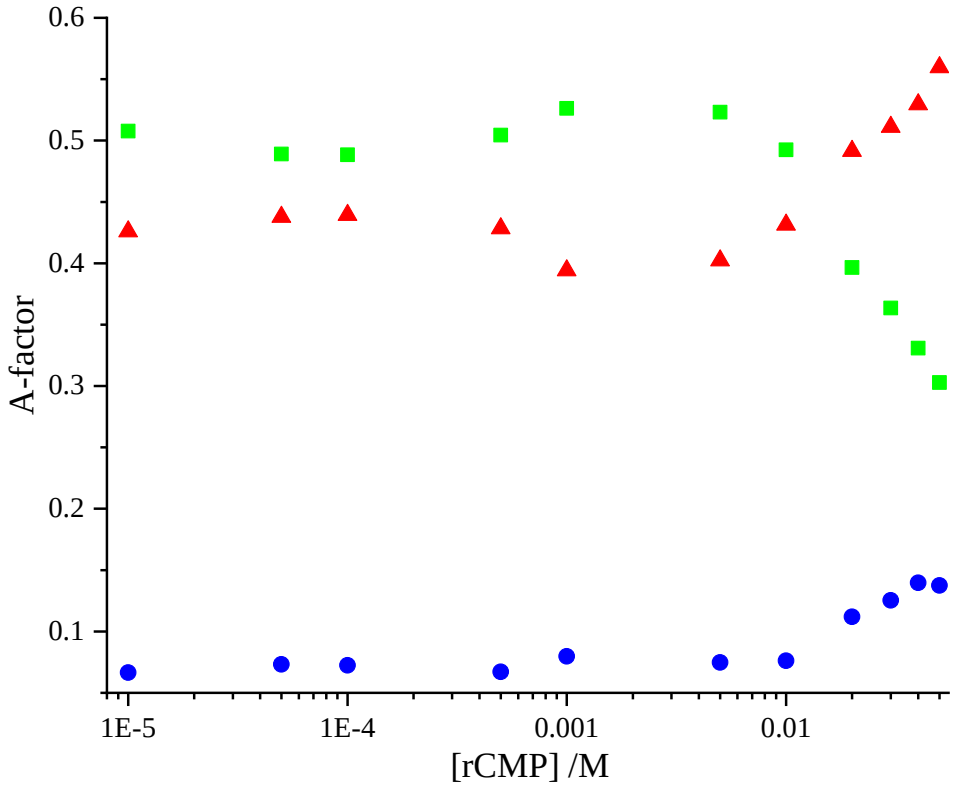

Figure 6.10: Pre-exponential factors (A-factors) of pArr fluorescence lifetime components as a function of rCMP concentration. A-factors shown: A_1 (green squares); A_2 (blue circles); A_3 (red triangles).

Based on the two datasets presented here and the previous work on pA-containing oligonucleotides, it could reasonably be predicted that for pAr in the presence of rGMP (Table 6.7), the longest lifetime component increases, while the average lifetime decreases. Indeed, the longest lifetime obtained for pAr does increase with rGMP concentration and tends towards a similar value, however, the average lifetime increases in tandem. This discrepancy may be due in part to the intermediate lifetime component reported here, which has over twice the magnitude reported for the previously reported oligonucleotide work. However, as before, the trend of the magnitudes of the longest and shortest lifetime components proceed in the expected direction based on lifetime data for free pAr and pA-substituted oligonucleotides. Only the intermediate lifetime component and the average lifetime are inconsistent with the previous oligonucleotide study. In essence, the value presented in Table 6.7 represents the average value of the intermediate lifetime, although it is relevant that fitting the decay curves separately didn't show a consistent change in this value with rGMP concentration, shown in . Results from fitting the pAr decay curve separately is shown for comparison.

[rGMP] /M	τ_1 /ns	τ_2 /ns	τ_3 /ns	A_1	A_2	A_3	$\langle\tau\rangle$/ns
0[a]	6.45	4.58	0.21	0.51	0.21	0.28	4.32
0	6.30	4.47	0.20	0.56	0.14	0.30	4.22
$1x10^{-5}$	6.30	4.47	0.20	0.56	0.14	0.30	4.21
$5x10^{-5}$	6.37	4.47	0.18	0.52	0.16	0.32	4.06
$1x10^{-4}$	6.39	4.47	0.21	0.52	0.18	0.30	4.20
$5x10^{-4}$	6.48	4.47	0.21	0.51	0.19	0.30	4.23
$1x10^{-3}$	6.45	4.47	0.20	0.50	0.16	0.34	4.03
$5x10^{-3}$	6.76	4.47	0.24	0.51	0.16	0.33	4.23
0.01	6.84	4.47	0.28	0.62	0.11	0.28	4.76
0.02	7.10	4.47	0.32	0.63	0.10	0.27	5.03
0.03	7.25	4.47	0.35	0.63	0.10	0.27	5.13
0.04	7.34	4.47	0.37	0.64	0.09	0.27	5.22
0.05	7.43	4.47	0.39	0.64	0.09	0.27	5.26

Table 6.7: Fluorescence lifetimes of pAr as a function of the concentration of rGMP concentration in tris-HCl buffer (20 mM). Values obtained from global analysis of data, with τ_2 kept constant for all spectra. (a) from separate fitting of free pAr decay data.

Illustrating the time-resolved data for pAr in the presence of rGMP graphically as before in Figure 6.11 to Figure 6.13, the shortest lifetime component steadily increases but the proportion steadily decreases with respect to the concentration of rGMP. In contrast, the lifetime and A-factor of the longest component increases concomitantly with the decreases in the A-factors of the short components. As for rAMP, a substantial discontinuity appears, albeit between 5 and 10 mM concentration of rGMP, again suggesting formation of a complex. Similar to the results from rAMP, it appears that ESPT is the dominant interaction, inducing an increased fluorescence lifetime due to tautomerisation as a result of proton transfer leading to a more stable, longer lived excited state.[7]

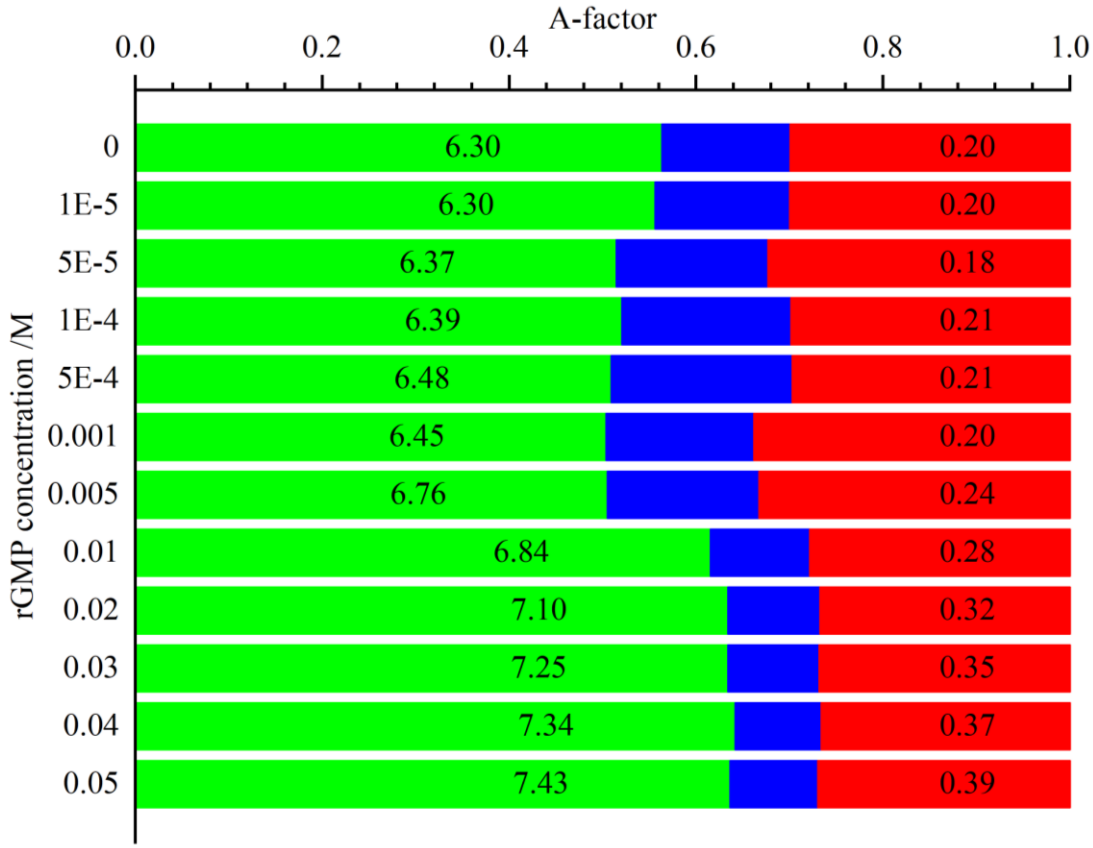

Figure 6.11: Graphical representation of time-resolved fluorescence measurements presented in Table 6.4 of pAr as a function of rGMP concentration. Lifetime data shown: τ_1 (green); τ_2 (blue); τ_3 (red). Lifetime and A-factor values were obtained from global analysis across all concentrations, the intermediate component τ_2 (4.47 ns) was kept constant for all decay curves.

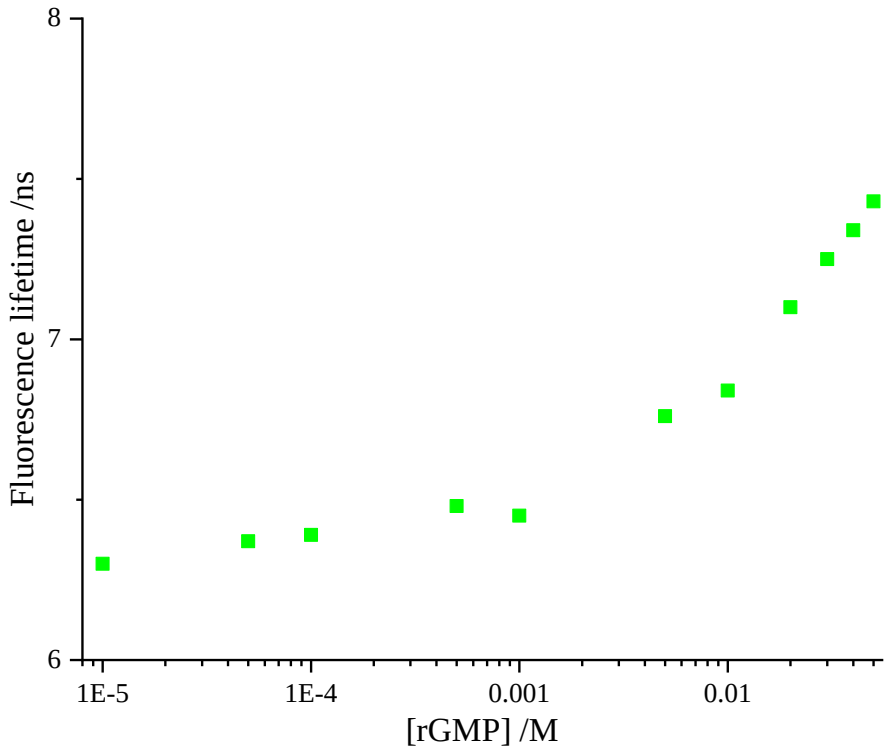

Figure 6.12: Fluorescence lifetime of longest component τ_1 for pAr in tris-HCl buffer (20 mM) as a function of rGMP concentration.

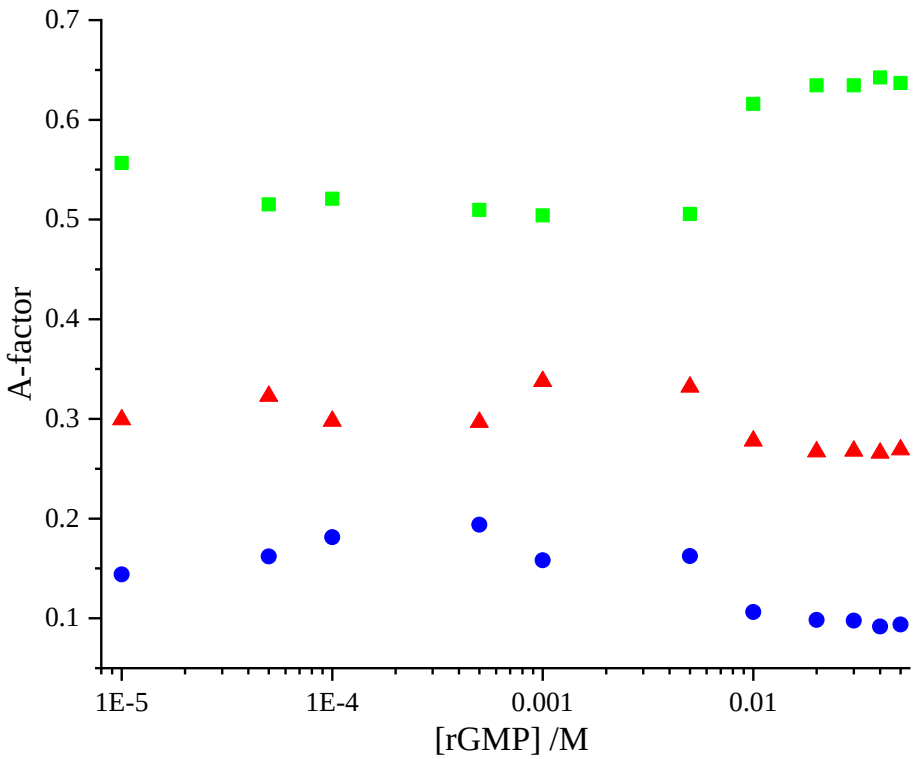

Figure 6.13: Pre-exponential factors (A-factors) of pAr fluorescence lifetime components as a function of rGMP concentration. A-factors shown: A_1 (green squares); A_2 (blue circles); A_3 (red triangles).

Fluorescence lifetimes for pAr in the presence of dTMP are shown in Table 6.8, using global fitting for concentrations of dTMP up to 5 mM inclusive with τ_2 linked, while decay curves were fitted separately at higher concentrations. Results from separate of pAr decay data is also shown for comparison. The data for dTMP are treated differently to the previous data sets due to the trend observed when every decay curve is fitted separately, which is shown in . Values for the intermediate lifetime component up to and including dTMP concentrations of 5 mM did not vary consistently, or by significant proportions.

[dTMP] /M	τ_1 /ns	τ_2 /ns	τ_3 /ns	A_1	A_2	A_3	$<\tau>$/ns
0[a]	6.14	2.68	0.15	0.49	0.06	0.45	3.24
0[b]	6.37	3.85	0.15	0.41	0.12	0.47	3.17
$1x10^{-5}$ [b]	6.29	3.85	0.16	0.46	0.10	0.44	3.35
$5x10^{-5}$ [b]	6.24	3.85	0.16	0.50	0.10	0.40	3.56
$1x10^{-4}$ [b]	6.22	3.85	0.15	0.48	0.08	0.44	3.37
$5x10^{-4}$ [b]	6.17	3.85	0.15	0.50	0.08	0.42	3.48
$1x10^{-3}$ [b]	6.17	3.85	0.15	0.50	0.09	0.41	3.47
$5x10^{-3}$ [b]	5.94	3.85	0.15	0.47	0.09	0.44	3.19
0.01[a]	5.46	0.76	0.10	0.48	0.04	0.48	2.70
0.02 [a]	5.02	1.26	0.09	0.36	0.04	0.60	1.93
0.03 [a]	4.68	2.04	0.10	0.32	0.04	0.64	1.64
0.04 [a]	4.26	0.52	0.07	0.24	0.06	0.70	1.09
0.05 [a]	3.98	0.44	0.06	0.20	0.06	0.74	0.87

Table 6.8: Fluorescence lifetimes of pAr as a function of the concentration of dTMP concentration in tris-HCl buffer (20 mM). Values obtained from (a) separate fitting of free pAr decay data (b) global analysis of data, with τ_2 linked.

Once again, based on the TT oligonucleotide data from previous work,[3] a decrease in magnitude with the concentration of dTMP across all lifetime components is expected, as well as substantial increases in the population of the shortest lifetime as a proportion of the total emitting population. With one caveat, this is indeed what was seen in the fluorescence lifetime data for pAr in the presence dTMP shown in Table 6.8 above. Examining the magnitudes of the lifetimes and A-factors for the highest concentration of dTMP shows a high level of consistency with the previous oligonucleotide work. At lower dTMP concentrations, however, the proportion of the

longest lifetime component increased slightly before reaching a maximum and then decreasing (the caveat mentioned earlier).

As before, these same lifetime values are represented visually for easier inspection of any emergent trends in the data. It appears that dTMP only causes minor changes in the fluorescence decay of pAr, until a concentration of 5 mM for dTMP was reached, after which the longest lifetime component decreased sharply both in magnitude and proportion, with a corresponding increase in the proportion of the shortest lifetime component and a steady decrease in the proportion of the intermediate component to 4 %. Both the intermediate and shortest lifetime component decrease with increasing concentration of dTMP. As for rCMP, dTMP also seems to form fluorescence quenching dimers with pAr above a threshold concentration of dTMP. These results for dTMP all suggest some sort of ground state interaction taking place, resulting in static quenching being observed. Only the intermediate lifetime behaves in a somewhat inexplicable fashion, which may be a result of not controlling the temperature of the sample during the experiment, the low population of the intermediate component, or some combination thereof, as described earlier. Even the intermediate component, however, shows distinct behaviour above 5 mM dTMP compared to that below 5 mM, which can be seen in the separately fitted data in as well.

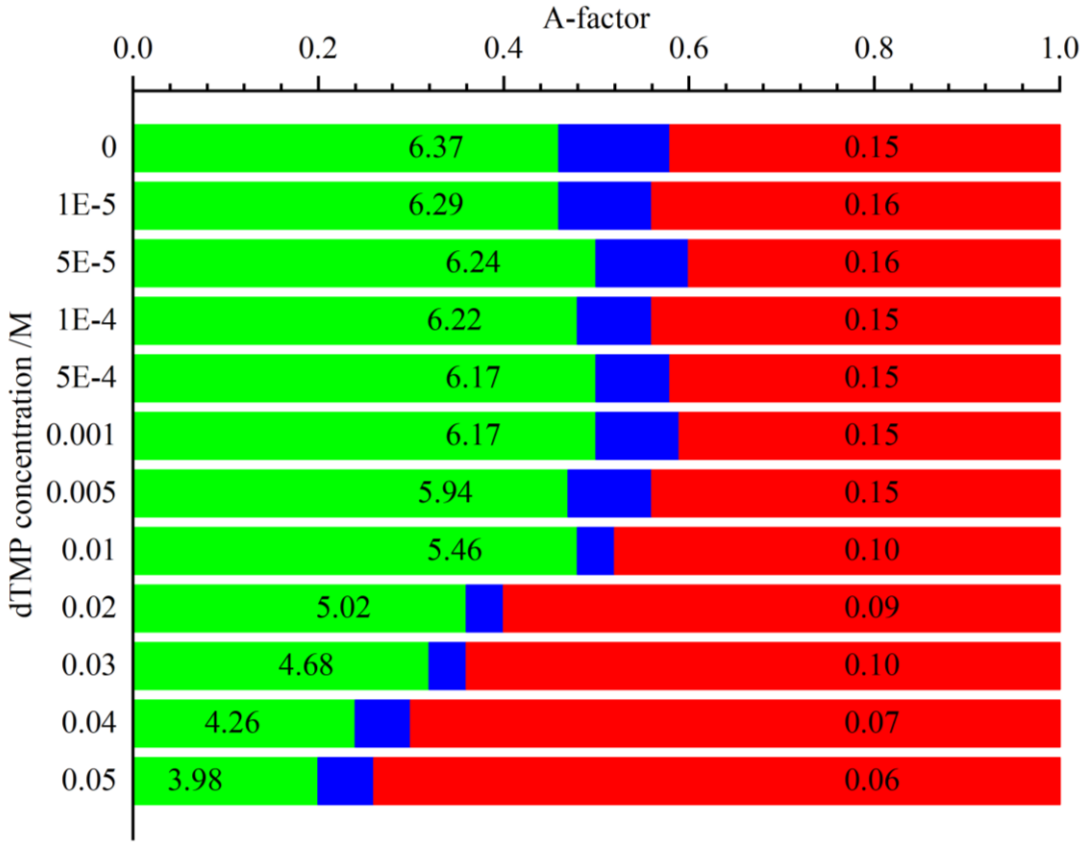

Figure 6.14: Graphical representation of time-resolved fluorescence measurements presented in Table 6.5 of pAr as a function of dTMP concentration. Lifetime data shown: τ_1 (green); τ_2 (blue); τ_3 (red). Lifetime and A-factor values were obtained from global analysis across all concentrations, the intermediate component τ_2 (3.85 ns) was kept constant below at dTMP concentrations 5 mM and below.

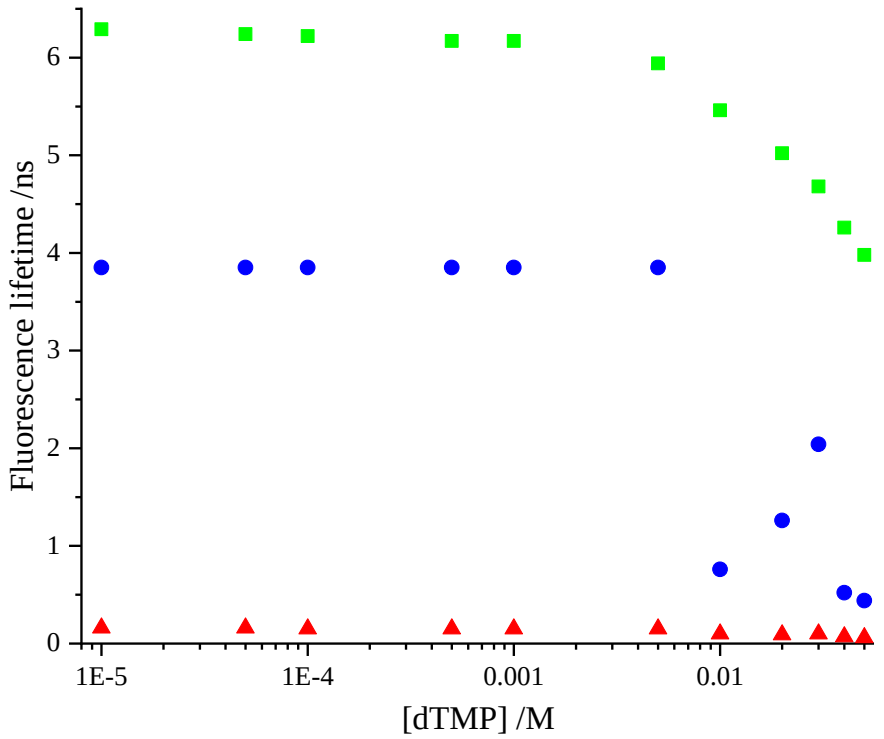

Figure 6.15: Fluorescence lifetime components for pAr in tris-HCl buffer (20 mM) as a function of dTMP concentration. Data shown: τ_1 (green squares); τ_2 (blue circles); τ_3 (red triangles).

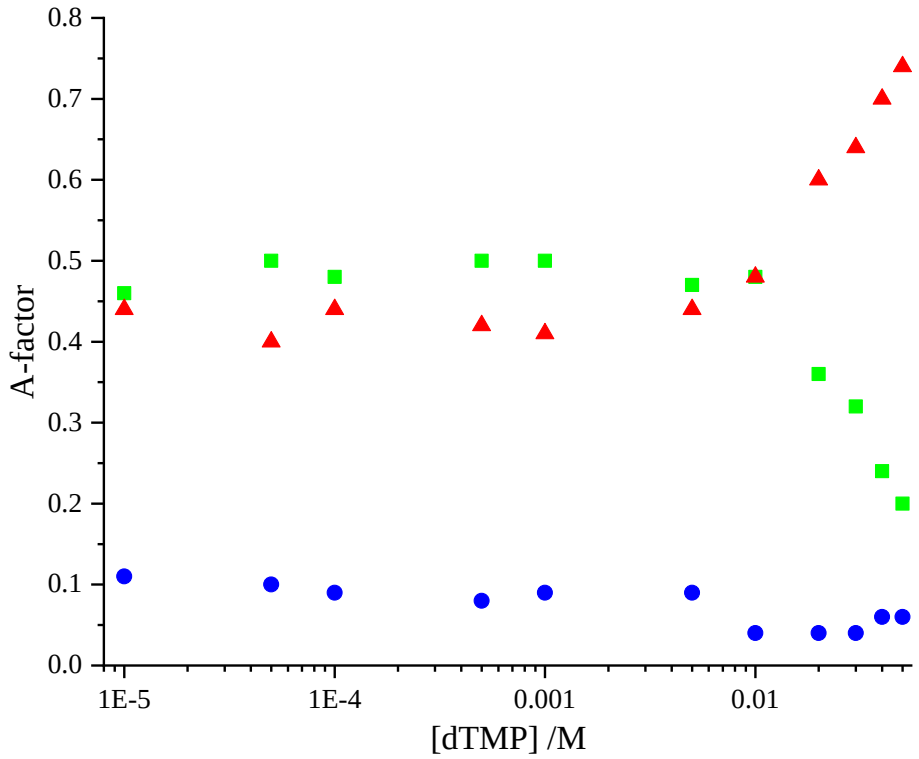

Figure 6.16: Pre-exponential factors (A-factors) of pAr fluorescence lifetime components as a function of dTMP concentration. A-factors shown: A_1 (green squares); A_2 (blue circles); A_3 (red triangles).

Qualitatively, it appears that the time-resolved fluorescence data recorded for pAr in the presence of rAMP, rCMP, rGMP and dTMP show largely equivalent

behaviour to relevant pA-containing oligonucleotides, based on the trends of their lifetime components and A-factors, as well as the average lifetimes. In some cases, the magnitudes of the fluorescence lifetimes obtained also closely match the lifetime components for previous work on pA-containing oligonucleotides. For the purines, it appears that a different process dominates, leading to fluorescence enhancement, possibly due to increased tautomerisation, which stabilises the excited state. In contrast, although there are signs that a similar process occurs between pAr and the pyrimidines as well, by far the dominant effect appears to be charge transfer, which reduces the fluorescence lifetime and quenches the fluorescence emission of pAr in a similar fashion to 2AP discussed elsewhere in this thesis.

6.4 Discussion

As already mentioned earlier, the complex photophysical behaviour of pAr in the presence of the natural DNA bases prevents a detailed quantitative characterisation, in a similar fashion to that demonstrated with 2AP in Chapter 4, of the effect of the bases on the fluorescence of pAr. However, it is possible to reach qualitative conclusions. For the most part, the lifetime components and A-factors of pAr, as well as the resulting average lifetimes, presented in this work show an overall trend with increasing base concentration between the relevant values for free pAr and the corresponding oligonucleotide (AA, CC, GG, or TT). A key difference between the study of free pAr in solution presented here and the previous oligonucleotide work is the presence of the sugar-phosphate backbone, which constrains the possible geometries adopted by pA and the natural bases, affecting interactions between adjacent bases, in particular base stacking interactions. This suggests an explanation for the discrepancies between the behaviour observed for pAr in solution and oligonucleotides containing pA. Observations from the solution-phase data presented in this work will be discussed first, followed by a comparison with the previous work using oligonucleotides.

In general, there appears to be a distinction between time-resolved fluorescence emission of pAr above and below a threshold concentration of the natural bases, the exact concentration of which varied slightly with the identity of the base but occurred around 1-5 mM. In addition, the form of this different photophysical behaviour exhibited by pAr was found to either be an increase in the average lifetime for purine bases or a decrease of the same for pyrimidine bases. Purine bases caused an increase

in the average fluorescence lifetime of pAr, while pyrimidines prompted a steep decrease in the average fluorescence lifetime of pAr. A decrease in the lifetime of pAr with increased pyrimidine base concentration is seemingly trivial to explain, in the terms of static (ground state interactions within a dimer structure) quenching, set out in Chapter 4. Dynamic quenching in the form of collisional interactions does not fit any of the data in the previous section, for the simple reason that a linear decrease in the lifetime across the entire concentration range would be expected. This makes it unlikely that dynamic quenching is a factor in the observed behaviour. Static quenching as described earlier, in contrast, is consistent with the pAr data for rCMP and dTMP, where the longest lifetime component of pAr decreased with base concentration above 5 mM, and the proportion of the total emitting population represented by the two shortest lifetime components ($A_2 + A_3$) increased with base concentration at the expense of the longest lifetime component.

Additionally, as noted throughout this chapter, the fact that multiple lifetime components were observed for pAr in the absence of any natural bases signifies that such a simplistic model on its own can't be justified, although possibly the increased population share of the shorter components could be attributed to ground state interactions between pAr and the pyrimidines. It is likely significant that there are three possible tautomers for pAr, and that three lifetime components were observed in the data presented here, as mentioned previously. From extensive prior studies of 2AP reviewed by Jones *et al*,[4] as well as some of the work in Chapter 4, it is known that tautomers exist as separate excited species and appear as separate lifetime components, and there is no obvious reason why the same principle should not apply to pAr.

The purine bases seem to increase the average lifetime of pAr. In addition, the longest and shortest lifetime components τ_1 and τ_3 increased with purine base concentration, while the intermediate component τ_2 was constant. Simultaneously, the proportion of the two shortest lifetime components out of the total emitting population ($A_2 + A_3$) decreased with increasing purine base concentration, while the proportion of the longest lifetime (A_1) increased. If static quenching, as previously described, was the primary driver of the observed trends, typically the opposite behaviour would be expected, i.e. the proportion of the shortest lifetime components should increase at the expense of the longest component population, as observed in the case of rCMP and dTMP. It could be that the lifetime and A-factor of a given component are negatively

correlated in the fitting algorithm to achieve a similar or better quality of fit, but that does not appear to be the case here, as consistent trends were observed which appear logical based on the current understanding of the system. If the observed changes were a result of the fitting process, they would most likely appear to be random. Therefore, the discussion will proceed on the assumption that all the trends observed in the results section are real and not merely an artefact of the fitting algorithm used.

One observation that remained constant across all the bases was the existence of a threshold concentration, above which there were changes in the trends of some of the lifetime components, around 5 mM. This suggests that not only does base stacking occur between pA and the natural bases, but that it affects the observed fluorescence output and the threshold concentration is of a similar order as that observed for 2AP in Chapter 4. It is therefore clear that the pyrimidines interact with pAr in a similar fashion to the interactions between 2AP and the natural bases, including the ground state interactions that lead to static quenching. In contrast, while it is clear that pAr forms ground state complexes with both rAMP and rGMP, it is equally clear that the fluorescence lifetime increases. Likewise, given that the longest lifetime component τ_1 also increases, this obviously cannot be explained by collisional quenching, although does not necessarily rule out collisional interactions playing some role. Evidently rAMP and rGMP interact with pAr in a distinct manner to rCMP and dTMP, which may be due to the extended fused aromatic ring system of the pA moiety leading to different preferred base stacking geometries for the purine and pyrimidine bases. There is some precedent for formation of complexes or aggregation enhancing fluorescence emission, in the form of aggregation-induced emission (AIE),[8] but this usually is due to rotational freedom around one or more bonds that is inhibited by aggregation, which leads to enhanced emission intensity. No such process can explain the current observations because of the planar, rigid aromatic nature of the pA fluorophore moiety.

Another possibility is ESPT, particularly given the existence of three distinct tautomers of pAr. Proton transfer by pAr in the excited state may increase the proportion of the more stable excited state tautomers, most likely represented by the component with the longest fluorescence lifetime in the data represented here. This fits particularly well with the data for the pyrimidine bases rAMP and rGMP, where both the proportion and magnitude of the longest lifetime component increased with base

concentration. Even in the case of rCMP and dTMP, at low concentrations the population of the longest lifetime increased initially before reaching a maximum. Based on these results, it appears that while ESPT was the dominant process in the presence of rAMP and rGMP, it also occurred when rCMP and dTMP were present but was overshadowed by another process, likely electron transfer, resulting in overall quenching of the fluorescence emission. It has been shown in previous work by Nagle and Morowitz[9] that the rate of proton transfer can be substantially increased when mediated by hydrogen bonded networks explicitly linked to comformation in the context of proteins. The rate of tautomerisation is therefore likely dependent on the relative orientation and position of the bases and pAr, suggesting that the pyrimidines and purines interact with pAr differently, with substantially different geometries during proton transfer. From the results presented earlier, it appears that rAMP and rGMP adopt positions relative to pAr in a complex which is more conducive to proton transfer, increasing the proportion and lifetime of the longest component, and/or reducing the likelihood of electron transfer, which decreases the A-factor and lifetime of the longest component. For rCMP and dTMP, at low concentrations a similar process seems to take place, however at higher concentrations it seems that electron transfer is the dominant process, shortening the average fluorescence lifetime.

Differences in the effect of the formation of complexes between purine or pyrimidine bases and pAr may be a consequence of the extended size of pAr, which allows for a larger variety of relative conformations for the pAr-NMP dimer that increase the probability of proton transfer, in contrast to 2AP. Using the assumption that ESPT results in enhanced fluorescence emission and longer lifetimes, while electron transfer results in reduced emission and shorter lifetimes, the results for rAMP and rGMP point to these bases favouring ESPT more than the pyrimidine bases, which could be a result of the change in size and shape between purine and pyrimidine bases. Given that tautomerisation in pAr occurs via movement of a proton from one nitrogen to another, it is logical to assume that proton transfer (ESPT) between pAr and the complexed natural base will depend on the tautomer of the pA moiety. There were signs that ESPT is still relevant for rCMP and dTMP, but that it is not the dominant interaction. This will be discussed in the context of rAMP and rGMP, where signs of ESPT are less ambiguous. It is likely, particularly given the fluorescence lifetime data shown earlier, that complexes involving specific tautomers of pAr have a different

fluorescence lifetime to the uncomplexed tautomer. However, the difference is likely not sufficient to resolve the uncomplexed and complexed lifetimes separately with the current data. In addition, that would result in 5 or 6 different lifetime components. Even considering that the lifetime of the intermediate component in almost all cases does not seem vary still leaves at least five separate components, which would not be feasible for the data presented in this chapter.

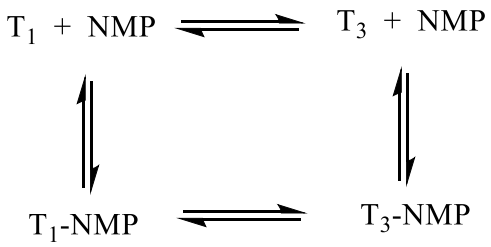

Figure 6.17: Equilibria between pAr tautomers and complexes of pAr tautomers formed with the monophosphate nucleotides. T_1 and T_3 refer to the tautomer species represented by lifetime components τ_1 and τ_3, respectively.

The model shown in Figure 6.17 may help to explain the results presented in this chapter. If, as assumed just now, T_1 and T_1-NMP combined are represented by the longest lifetime component, while T_3 and T_3-NMP combined are represented by the shortest lifetime component, then the population of the longest lifetime component (T_1 + T_1-NMP) will be dependent on the position of the new equilibrium between T_1-NMP and T_3-NMP. In addition, the relevance of this equilibrium between the different possible dimers will increase as the total population of the dimer species increases. A similar argument applies to the shortest lifetime component. For the purine bases (rAMP & rGMP) when complexed with pAr, the population of the longest component (A_1) increased with concentration of purine base, while the population of the remaining components (A_2 & A_3) decreased. It appears that the model in Figure 6.17 is not complete for these purine-pAr systems and that the dimer T_2-NMP (which was included in the intermediate lifetime component) was also in dynamic equilibrium with the other tautomeric dimers. This suggests that the equilibrium favours formation of the dimer T_1-NMP that is part of the lifetime component with the longest lifetime τ_1, at the expense of the other tautomers (Figure 6.7 & Figure 6.13). In contrast, for complexes between the pyrimidine bases (rCMP & dTMP) and pAr, the equilibrium shifted towards the T_3-NMP dimer at the expense of the T_1-NMP dimer (Figure 6.10 & Figure 6.16), while the T_2-NMP dimer population (A_2) hardly changed. It appears that the change in the population of the various lifetime components was a

consequence of the new equilibria between the dimer species, given that the changes were only observed above a threshold concentration of the NMP species. Not only was this concentration of a similar magnitude (1-5 mM) across all the natural bases, but was consistent with the equivalent concentration for another FBA, 2AP, shown in Chapter 4. This threshold concentration being similar regardless of base identity is also a sign that the position of the equilibrium between free pAr and the dimer for a given concentration of NMP was the same regardless of the natural base identity and therefore was not a factor in the differing effects observed of the bases upon the fluorescence of pAr.

It has already been noted that, in a similar fashion to the population of each species, the fluorescence lifetimes themselves for different components is likely a result of the combination between the relevant free pAr tautomer and the dimerised species, which may explain the changes observed. As before, there is a qualitative distinction between the effect on pAr fluorescence lifetimes due to purine and pyrimidine bases. In the case of purine bases, both rAMP and rGMP show increases in the longest lifetime component τ_1, but only above the threshold concentration mentioned earlier. This observation indicates that the increase in lifetime is due to the formation of dimers between rAMP or rGMP and the tautomers of pAr, specifically the T_1-NMP dimer. It appears from the results presented earlier that rAMP and rGMP form a complex with pAr that results in a species with a longer fluorescence lifetime, at least for the T_1 tautomer. The observed changes are simply the fluorescence lifetime components tending towards the natural lifetimes for the dimers as a result of the relative increase in the total dimer population. A plausible mechanism for the increased lifetime of the T_1-NMP dimer may be ESPT, which possibly also explains the changes in relative populations of the different lifetime components in the presence of rAMP or rGMP, given that the tautomers of pAr are merely the result of an exchanged proton. In the case of the pyrimidine bases rCMP and dTMP, both showed sharp decreases in the longest lifetime component τ_1 above the threshold concentration, which is characteristic of electron transfer within the dimer T_1-NMP. That does not rule out proton transfer, whether in the excited state or not, but it does not induce enhanced fluorescence for pAr dimers containing pyrimidine bases as it does for purine bases. There were anomalous results for the intermediate lifetime component τ_2 for pAr-dTMP, which may be a result of the relevant free pAr tautomer T_2 and the

corresponding dimer T_2-NMP having significantly different fluorescence lifetimes, which was not the case for the other natural bases. As before, it is likely that the observed changes in lifetime values are merely a result of the increase in population of the pAr dimers relative to the corresponding free pAr tautomer, tending towards the natural values of the individual tautomers. Such a finding strongly suggests that purine and pyrimidine interact differently with pAr, likely as a result of the relevant dimers adopting a different structure, in turn due to the different size and shape of purine and pyrimidine bases.

It is important to note the level of agreement between the lifetimes measured for pA in equivalent oligonucleotides and those measured for free pAr in the presence of the nucleotide monophosphates in solution, with the exception of rCMP. Likewise, the proportion of the combined shortest lifetime components, 30-40 % for the pyrimidines and 70-80 % for the purines, presents a similar qualitative trend seen for the previous oligonucleotide reports,[3, 6] with ≥95 % for the pyrimidines. A guanine oligonucleotide (GG) had a relatively high proportion of the shortest lifetime components, at 71 %, but this is still lower than the previously reported pyrimidine results, while the equivalent proportion was 31 % for adenine. This further supports the previous observation that the purines have distinct base stacking interactions with pAr compared to the pyrimidines. Although the magnitudes differ, this can potentially be explained by the structure being more well-defined with the sugar-phosphate backbone, which may hold the adjacent bases in a different relative position than would otherwise be the case. As stated in the previous paragraph, the relative rates of proton transfer may depend on the relative positions of the two bases, which will be different in oligonucleotides due to the restrictions imposed by the sugar-phosphate backbone.

Returning to the fluorescence lifetimes of the oligonucleotides mentioned in the introduction,[3, 6] it can be seen that the behaviour of the various components when different bases are adjacent to pAr was consistent with the results reported in this work. In particular, there is very good agreement between the fluorescence lifetime of the shortest component for the pAr-NMP complexes and the relevant oligonucleotides (Table 6.1). In contrast, there is somewhat less agreement between the data presented here for the pAr-NMP complexes and the previous oligonucleotide work[3, 6] for the fluorescence lifetimes of the intermediate and longest component. For reasons

mentioned earlier, the non-radiative decay rate and hence the fluorescence lifetime of these pAr tautomers represented by the intermediate and longest lifetime component appear to be highly sensitive to the conformation of the natural bases within the formed dimer. In an oligonucleotide, the conformation of adjacent bases will be constrained by the sugar-phosphate backbone, which isn't present in the dimers seen in the systems examined in this work. Therefore, it is highly likely that the conformation of pAr-NMP dimers will be different to the relative conformation of adjacent bases in oligonucleotide strands, so the fluorescence lifetimes are likely to be different as well. The conformation of pA-containing dinucleotide strands as a proxy for oligonucleotides will be examined further in the next chapter.

6.5 Conclusions

Time-resolved fluorescence measurements presented in this work show that solution-phase measurements of free pAr in the presence of the natural DNA bases can be used to partially predict and explain the photophysical behaviour of pA-containing oligonucleotides. This work extends the principle first mooted previously in Chapter 4 that with careful consideration of the relevant fluorescence spectral data, a reasonable estimate of the behaviour of a novel fluorescent base analogue in oligonucleotides, even one as complex as pA, can be obtained. In this way, it was found that even in solution without a sugar-phosphate backbone linking pA to an adjacent natural base, the qualitatively distinct effects of the purine bases compared to the pyrimidine bases on pA were reproduced in the solution-phase measurements presented earlier. The observed changes in the fluorescence emission of pAr were found to be due solely to the formation of dimers between the NMP and the tautomers of pAr, based on the observation that no significant changes were observed below a certain threshold concentration of approximately 1-5 mM. Collisional interactions between pAr and NMP could and likely did occur, but they were found to not result in consistent changes to the fluorescence lifetime, in contrast to the findings for 2AP. Adenine and guanine were found to increase the average fluorescence lifetime, while cytosine and thymidine were found to decrease the average lifetime, which in all cases was consistent with the respective oligonucleotide. When considering the behaviour of individual lifetime components, it became clear the purine bases facilitated ESPT for pAr, while electron transfer was the dominant effect on fluorescence emission of pAr in the presence of the pyrimidine bases, based on their impact on the photophysical

behaviour of pAr in solution. This was also found to be consistent with the time-resolved fluorescence output of the corresponding pA-containing oligonucleotides from previous work.[3, 6]

In summary, the work presented in this chapter showed that the concept of solution-phase fluorescence measurements used in the context of the very well-known and extensively used fluorescent base analogue 2AP extends to more novel and complex fluorescent base analogues such as pA. This study also provides further confirmation that the behaviour of fluorescent base analogues in oligonucleotides can be reproduced in solution with a surprising level of detail and accuracy.

6.6 References

1. M. Bood, A. F. Fuchtbauer, M. S. Wranne, J. J. Ro, S. Sarangamath, A. H. El-Sagheer, D. L. M. Rupert, R. S. Fisher, S. W. Magennis, A. C. Jones, F. Hook, T. Brown, B. H. Kim, A. Dahlen, L. M. Wilhelmsson and M. Grøtli, *Chemical Science*, 2018, **9**, 3494-3502.
2. R. S. Fisher, D. Nobis, A. F. Füchtbauer, M. Bood, M. Grøtli, L. M. Wilhelmsson, A. C. Jones and S. W. Magennis, *Physical Chemistry Chemical Physics*, 2018, **20**, 28487-28498.
3. R. S. Fisher, University of Edinburgh, 2018.
4. A. C. Jones and R. K. Neely, *Q Rev Biophys*, 2015, **48**, 244-279.
5. O. J. G. Somsen, v. A. Hoek and v. H. Amerongen, *Chemical Physics Letters*, 2005, **402**, 61-65.
6. R. S. Fisher, unpublished work.
7. P. Zhou and K. Han, *Accounts of Chemical Research*, 2018, **51**, 1681-1690.
8. Y. Hong, J. W. Y. Lam and B. Z. Tang, *Chemical Society Reviews*, 2011, **40**, 5361-5388.
9. J. F. Nagle and H. J. Morowitz, *P Natl Acad Sci USA*, 1978, **75**, 298-302.

Chapter 7 Computational Investigation of pA-containing Dinucleotides Structure and Conformation

"Nature will tell you a direct lie if she can."

Charles Darwin

7.1 Introduction

In this chapter, the effect on DNA conformation of substitution of pA into single-strand dinucleotides (deoxydinucleoside monophosphates) will be examined. Up to this point in this thesis, the effect of substitution of fluorescent base analogues (FBAs) on DNA structure has been alluded to but not properly and systematically examined. This is an important consideration because, if the purpose is to get an idea of how DNA behaves in its natural environment, anything other than relatively minor changes to the structure caused by substitution of a particular FBA renders that FBA practically useless as a fluorescent probe. However, there are some caveats, particularly what is meant by relatively minor changes, which will be discussed in a moment. It is nevertheless important to be able to examine the structural impact of introducing pA into DNA, which will be achieved using geometry optimisation *via* DFT calculations of dinucleotide model systems.

In order to answer the central question of this chapter, which is whether substitution of pA into DNA results in a natural conformation, first a standard definition of what constitutes a natural DNA structure needs to be found. The specifics of how DNA structure is usually classified was presented in Chapter 2, the essentials of which will be repeated here. DNA structure can be divided up into two or three main components, as shown in Figure 7.1: the bases adenine, guanine, thymine, and cytosine; and the deoxyriboside sugar linking the bases to phosphate groups, which in turn link the sugars attached to individual bases together. For most of the remainder of this chapter, the sugar and phosphate groups will be considered as a combined unit and referred to as the sugar-phosphate backbone. This backbone runs along the outside of the DNA structure and is one factor that contributes to the double helical shape of DNA, the others being base-stacking interactions between adjacent bases and base-pairing interactions between neighbouring DNA bases across from each other on opposite strands. Arrangements of base position and orientation relative to adjacent bases is strongly influenced by backbone conformation, which can be quantified using

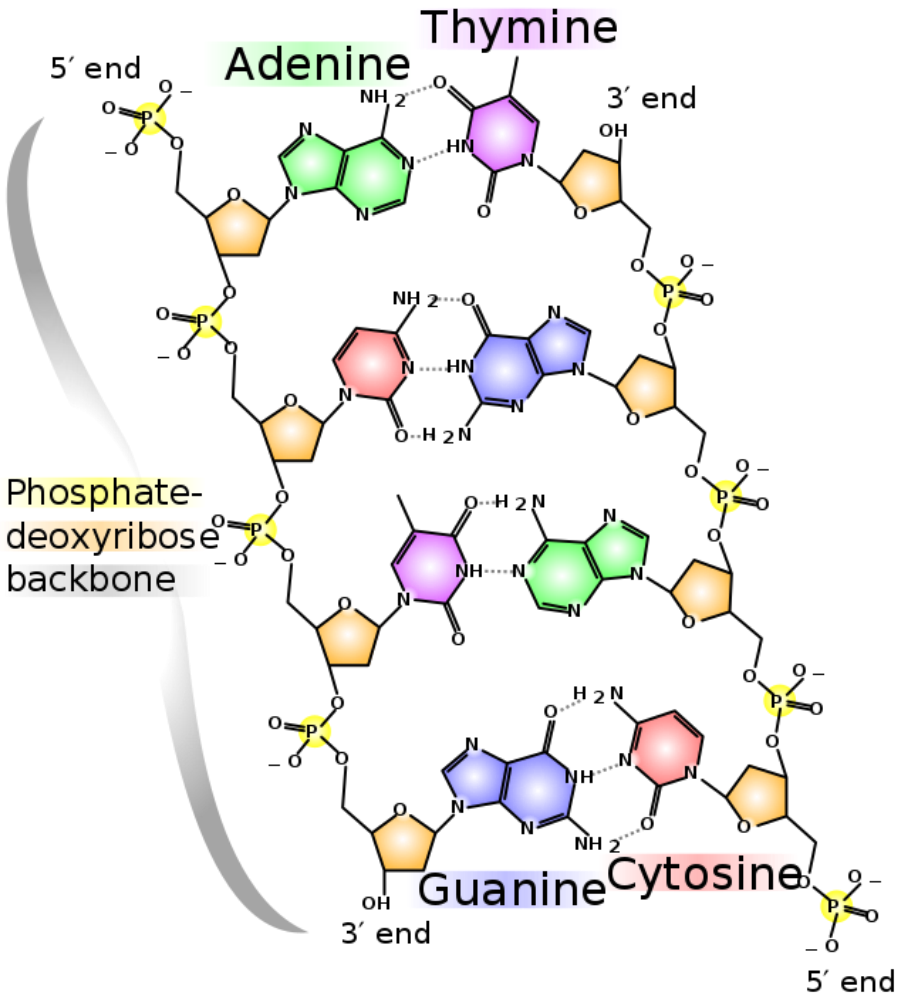

Figure 7.1: Chemical structure of double-stranded DNA, image reproduced from Wikimedia Commons (creator Madeleine Price Ball)

torsional backbone parameters, a series of either bond or dihedral angles first defined by Dickerson *et al*.[1] Similarly, base-step parameters define relative angles and displacements of adjacent bases along certain axes, which are again defined by Dickerson *et al*.[2] In combination, the base-step and backbone torsional parameters form a set of measurements which can be used to quantitatively compare the conformation of different DNA sequences in a uniform manner.

Now that it has been established DNA conformation can be defined in a specific way, it remains to define what a standard DNA conformation looks like in the system described in the previous paragraph. Each base plus the corresponding sugar and phosphate groups amounts to around 30-50 atoms. In three dimensions, that results in a large number of degrees of freedom even for a single nucleotide, such that even short strands of DNA could reasonably be expected to have an extremely large number of conformational states. However, in reality there are a significant number of constraints that reduce the actual number of degrees of freedom. First, the bases themselves are aromatic systems which adopt a rigid, planar structure, inhibiting the independent movement of atoms in the aromatic ring moieties. Substituents attached to the aromatic rings have more freedom, but even their degrees of freedom are somewhat reduced. Second, the sugars are closed furanose rings limited to half-boat conformations, again limiting the number of degrees of freedom. Third, the relative positions of adjacent bases is inextricably linked with the backbone conformation, further restricting the possible conformational space as change in one leads inexorably to change in the other. To illustrate this point, imagine changing the conformation of the sugar ring, assuming that the bond angles involving the bond between the sugar and the base remain constant, which will cause the base as a whole to be translated in space. Fourth, adjacent bases experience interactions through their π-electron clouds that lower the energy of the structure, which require bases to satisfy a narrow range of positions and orientations. Finally, in double-stranded DNA complementary bases form hydrogen bonds, further restricting movement, although this last point does not affect the current work, as only single-stranded dinucleotides were studied. Taken all together, this results in the observation that only three main types of natural DNA are commonly observed. Of these, Z-form DNA is only seen for sequences rich in guanine, while the A-form occurs most often for RNA. By far the most common is B-form DNA, which is therefore the conformation that will be assumed to represent

natural DNA in the present study. These different conformations have different defining characteristics, Z-DNA has a left-handed helix in contrast to A- and B-DNA. A-form and B-form DNA are primarily distinguished by the number of bases per helical turn, 11 and 10 per turn for A- and B-DNA, respectively.

α /°	β /°	γ /°	δ /°	ε /°	ζ /°	χ /°
275-325	125-200	25-75	100-150	150-250	~225-300	~200-300

Table 7.1: Typical values of torsional backbone parameters for B-form DNA.[3]

Shift /Å	Slide /Å	Rise /Å	Tilt /°	Roll /°	Twist /°
~0	~0	~3.4	~0	0-25	34-36

Table 7.2: Typical values of base-step parameters for B-form DNA.[1]

All of the commonly observed DNA conformations, A-DNA, B-DNA and Z-DNA, can therefore be defined in terms of characteristic backbone torsional and base-step parameters mentioned earlier.[1, 3] Typical values for B-DNA are shown in Table 7.2 and Table 7.1 above. Particularly relevant due to their distinct range of values for B-form compared to A-form (Z-form DNA is trivial to identify by inspection because of its opposite handedness) are the rise and twist (the rotation mentioned earlier) from the base-step parameters, as well as the δ and χ values for the backbone, which are ~2.9 Å, 34-36 °, 100-150 ° and 200-300 °, respectively. Diagrams with illustrations of the base step and sugar-phosphate backbone parameters are shown in Figure 7.2 and Figure 7.3, respectively. It does need to be borne in mind by the reader that despite the statements in the previous paragraph about the restrictions that limit the possible conformations of DNA to three main types, there is still a large degree of conformational flexibility inherent in the DNA structure. Therefore, the three main DNA conformations are more like families of conformations rather than rigid, exact structures. Likewise, the typical structural parameters for each 'family' is probably best represented as a range, rather than a single value, although an average value will at times be quoted here. This is also related to the comment at the beginning of this chapter about the definition of relatively minor changes. To illustrate this point and to establish an estimate of reasonable values for B-DNA, the structural parameters for each adjacent stacked base pair of the B-DNA dodecamer crystal structure 4C64 taken from the PDB online is presented in Table 7.3 and Table 7.4 below.[4] It is noticeable that there is a non-negligible variation in structural parameters across adjacent base pairs along the structure, which is presented as a range in the final row. One final

parameter to consider is the sugar pucker, which is usually defined by the atom in the sugar ring that 'sticks out' of the plane defined by the other four atoms in the five-membered ring. This nonplanar atom is characterised as being *endo* or *exo*, where *endo* signifies that it is displaced to the same side of the ring as the C5' atom, and *exo* on the opposite side of the ring. For B-DNA, this is typically C2'-endo, but Table 7.3 shows that even for 'ideal' B-DNA structures (defined here as a Dickerson-Drew dodecamer) other sugar puckering conformations exist, particularly C1'-exo and C4'-exo as well as O4'-exo at the 3' terminus.

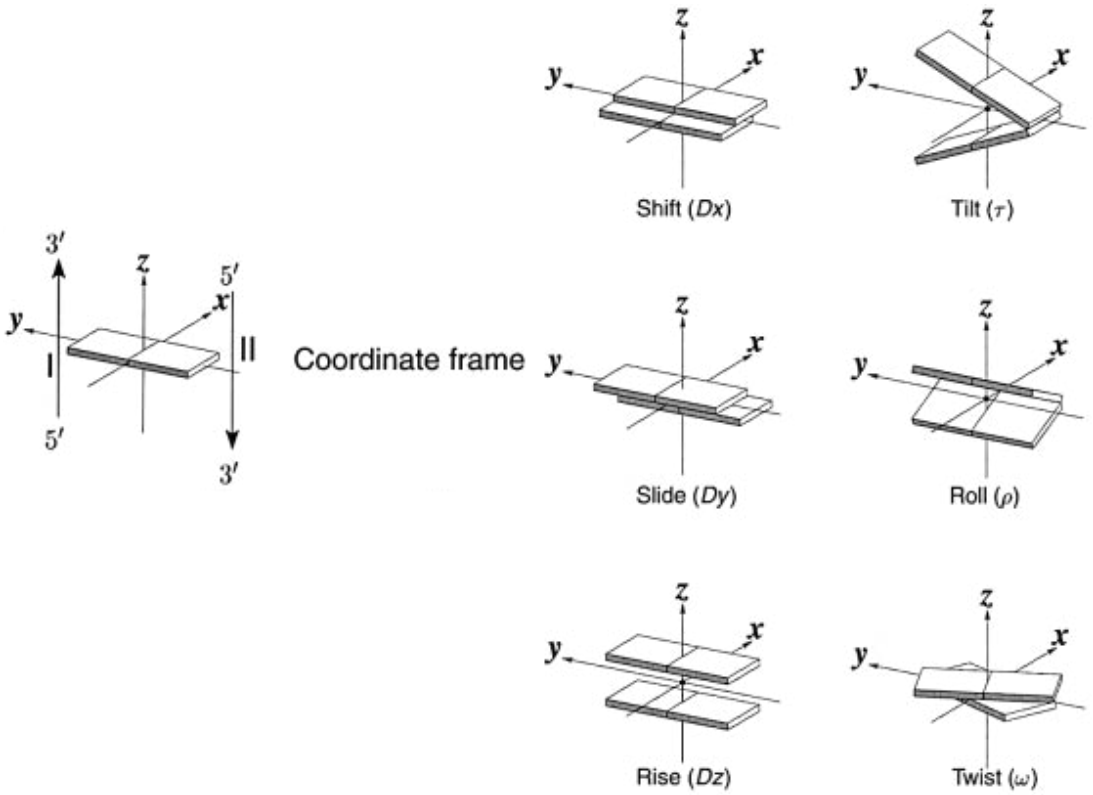

Figure 7.2: Illustration of base-step parameters in double-stranded DNA. Adapted from the published model used in the 3DNA software developed by Lu and Olson.[5-7]

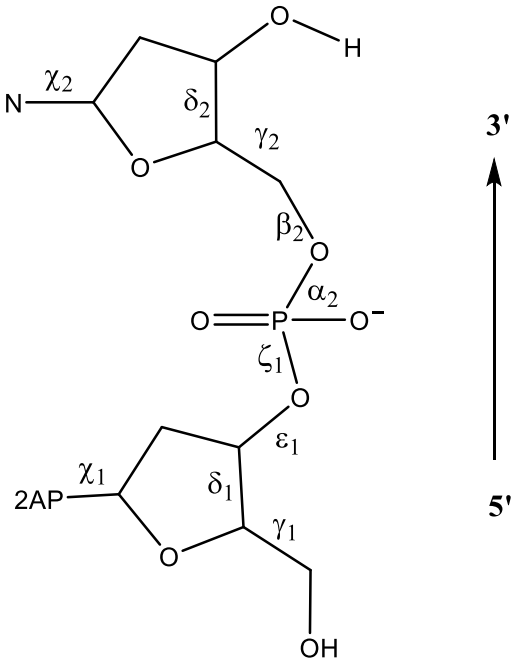

Figure 7.3: Structure of 2AP-containing dinucleotides with labelled dihedral angles in sugar-phosphate backbone. N represents any natural DNA base (A, C, G, T). 5' and 3' represent termini of the strand, based on their relative position around the sugar ring.

Comparing the values in Table 7.3 with Table 7.1, the average value for each of the backbone parameters falls quite neatly in the centre of the corresponding range typical for B-DNA. The range of values in Table 7.3 are also less than or equal to the range of typical values in Table 7.1 above. Similarly, the average values in Table 7.4 are quite close to the ideal values for base-step parameters in B-DNA presented in Table 7.2 above. It should be noted that terminal phosphate groups were excluded from the dinucleotides examined in this work, which is some dihedral angles are only presented for one or other of the nucleotides. This can clearly be seen clearly in Figure 7.3, by comparing β_1 with the corresponding dihedral angle for the 5' base. Similarly, ε & ζ can only be defined for the 5' base, and α for the 3' base, in the dinucleotides discussed in the results and discussion sections. In addition, negative angles have been added to 360 ° to make them directly comparable with the values in Table 7.1, the exception being the first value for γ which appears to be an outlier. The data shown here also give an idea of the range of values that constitute an acceptable range in order to be able to classify a particular strand of DNA as B-form. It is not surprising that Table 7.1 and Table 7.3 are consistent, given the data in Table 7.1 were accumulated from a large collection of DNA crystal structures,[3] but it is comforting to see that the average values of the base-step parameters in Table 7.4 quite closely match the ideal values in Table 7.2, even if there is a significant variation between individual

	α /°	β /°	γ /°	δ /°	ε /°	ζ /°	χ /°	sugar pucker
1 C	-	-	-69.1	144.3	190.0	258.1	258.5	C2'-endo
2 G	290.0	186.8	42.0	138.8	188.7	235.8	271.9	C2'-endo
3 C	308.2	147.0	53.2	85.8	187.8	278.4	228.3	C4'-exo
4 G	297.5	176.9	60.7	142.3	174.1	249.2	263.3	C2'-endo
5 A	301.6	173.8	59.8	131.4	176.6	275.3	245.5	C2'-endo
6 A	289.4	186.2	49.8	121.6	173.5	268.6	247.3	C1'-exo
7 T	305.6	171.1	52.6	109.5	179.8	269.3	235.8	C1'-exo
8 T	300.2	173.5	54.4	115.4	168.2	269.6	239.8	C1'-exo
9 C	301.5	184.7	56.2	131.4	200.0	273.2	243.1	C2'-endo
10 G	290.0	169.0	45.0	143.2	258.3	148.9	269.5	C1'-exo
11 C	288.1	146.5	50.8	139.4	197.1	277.0	256.3	C2'-endo
12 G	283.5	176.7	38.9	101.1	-	-	258.4	O4'-exo
Mean	296.0	172.0	41.2	123.6	190.4	254.9	251.5	
Range	24.7	40.3	129.8	57.4	90.1	129.5	43.6	

Table 7.3: Structural parameters for the sugar-phosphate backbone in a typical double-stranded DNA dodecamer (PDB code 4C64). Values shown for one strand only.

	Shift /Å	Slide /Å	Rise /Å	Tilt /°	Roll /°	Twist /°
C/G	0.06	0.16	3.45	0.90	11.26	33.18
G/C	1.06	0.59	3.30	2.63	-3.91	42.53
C/G	-0.26	0.89	3.03	10.06	10.40	25.97
G/A	0.49	0.06	3.33	1.13	3.38	39.39
A/A	0.55	-0.34	3.32	1.44	2.60	36.03
A/T	0.38	-0.63	3.23	3.17	-2.26	31.38
T/T	0.36	-0.47	3.08	6.04	-0.39	34.58
T/C	0.36	-0.43	3.51	-0.88	-1.98	39.60
C/G	0.65	0.70	3.09	7.30	3.40	27.89
G/C	-0.79	0.75	3.36	1.99	-12.28	42.90
C/G	0.50	0.44	3.33	3.56	10.30	30.57
Mean	0.31	0.16	3.27	3.40	1.86	34.91
Range	1.44	1.52	0.48	10.94	23.54	16.93

Table 7.4: Base-step parameters in a typical double-stranded DNA dodecamer (PDB code 4C64). Values shown for one strand only, calculated from structural files using the 3DNA software package.[5, 6, 8]

values (which is itself useful information). This is relevant because the ideal base-step parameters in Table 7.1 are based on what B-DNA is expected to look like. However, this only connects ideal B-DNA structural parameters with experimentally measured crystal structures, and this chapter is focused on B-DNA structures derived from theoretical calculations, and whether B-DNA structures can even be obtained this way in reality.

	α /°	β /°	γ /°	δ /°	ε /°	ζ /°	χ /°	sugar pucker
A/A 1	-	-	50.7	145.8	184.9	275.3	249.2	C3'-exo
A/A 2	294.5	170.4	52.5	126.3	-	-	239.9	C1'-exo
A/C 1	-	-	50.2	145.2	185.6	275.2	249.3	C3'-exo
A/C 2	295.3	169.1	55.1	115.0	-	-	233.6	C1'-exo
A/G 1	-	-	50.4	145.8	185.8	275.7	248.5	C3'-exo
A/G 2	294.2	170.2	51.8	127.8	-	-	242.2	C1'-exo
A/T 1	-	-	51.0	146.7	186.0	277.4	249.4	C2'-endo
A/T 2	294.9	167.6	54.8	105.6	-	-	228.2	O4'-endo
Mean	294.7	169.3	52.1	132.3	185.6	275.9	242.5	
Range	1.1	2.8	4.9	41.1	1.1	2.2	21.2	

Table 7.5: Structural parameters for sugar-phosphate backbone of adenine-containing dinucleotides. Data reproduced from reference [9]. Values for 5' nucleotide presented in top row, and for 3' nucleotide in bottom row for each nucleotide.

	Shift /Å	Slide /Å	Rise /Å	Tilt /°	Roll /°	Twist /°
A/A	1.32	-0.30	3.13	2.03	1.30	35.92
A/C	1.03	-0.44	2.96	3.89	4.08	34.20
A/G	1.28	-0.31	3.06	3.35	1.29	34.26
A/T	1.37	-0.64	2.88	5.08	3.17	33.00
Mean	1.25	-0.42	3.01	3.59	2.46	34.35
Range	0.34	0.34	0.25	3.05	2.79	2.92

Table 7.6: Base-step parameters for adenine-containing dinucleotides. Data reproduced from reference [9].

The methodology in this chapter is based on earlier work by Smith *et al*[9] which reported the structures of adenine-containing dinucleotides obtained from DFT calculations with a PCM to account for solvation in water implicitly, using initial structures obtained from the 4C64 crystal structure. Backbone and base-step parameters presented in that previous work are reproduced in Table 7.6 and Table 7.5

below. Underlying the approach by Smith and co-workers, emulated in the current work, is the basic premise that a DNA sequence, even one containing non-canonical bases, will return a B-DNA structure from geometry optimisations if the sequence exists in B-DNA form in reality. This is, however, dependent on the starting structure being relatively close to a B-DNA-like conformation. Bearing in mind the earlier statements about conformational flexibility within B-DNA structures, the authors in the previous work[9] showed that B-DNA structures are obtained from calculations for the dinucleotide species studied, based on their results reproduced in Table 7.6 earlier. These findings suggest that dinucleotides are appropriate models of longer DNA strands, at least for the purposes of the work presented in this chapter.

Once again, the values reported in the previous work seem to be consistent with expected structural parameters for B-DNA. Furthermore, the values of parameters highlighted as unique to B-DNA (the rise and twist between adjacent bases as well as the backbone parameters δ and χ) are consistent with B-DNA, with average values of 3.01 Å, 34.35 °, 132.3 ° and 242.5 °, respectively. This showed that a B-DNA structure can be reproduced from theoretical DFT calculations for a dinucleotide, where a B-form conformation is known for that particular sequence, provided that a suitable starting structure is chosen. While theoretical calculations do not by themselves prove that a B-form structure exists in truth, and DFT in particular has weaknesses with regards to DNA base stacking because it does not explicitly account for dispersion, the functional employed in the previous work (M06-2X) is one of a few that allows for dispersion implicitly and has been shown to be accurate for calculations involving DNA.[10] The previous work shows that at the very least, calculations can be used to show that a mutated FBA does not undergo 'normal' base-stacking in a B-DNA type structure. On a qualitative level, DFT often produces a similar accuracy to *ab initio* methods such as MP2 for noticeably less computational effort, and use of higher levels of theory is not feasible for systems on the scale of a dinucleotide due to the exponential increase in computational power required.

Smith and colleagues continue, in the same report, with an investigation of 2AP-containing dinucleotides, by mutating adenine to 2AP in each of the geometry optimised canonical dinucleotides and performing the same process using DFT calculations. Their results for 2AP-containing dinucleotides are reproduced in Table 7.7 and Table 7.8, showing that even for systems containing non-canonical bases, the

existence of B-DNA structures can be demonstrated using DFT calculations. On its own, data from theoretical structure calculations is not definitive positive proof that a particular DNA sequence exists in B-DNA form in solution, but it does support that conclusion. Other empirical data can be used to further support the assignment of B-DNA-like conformation, such as CD[11, 12] and NMR[13, 14] measurements.

	α /°	β /°	γ /°	δ /°	ε /°	ζ /°	χ /°	sugar pucker
2AP/A 1	-	-	50.2	146.0	183.9	273.8	250.6	C3'-exo
2AP/A 2	293.0	174.0	50.4	132.3	-	-	245.5	C1'-exo
2AP/C 1	-	-	50.3	145.6	186.3	275.6	250.3	C2'-endo
2AP/C 2	294.7	166.7	55.6	103.6	-	-	227.3	O4'-endo
2AP/G 1	-	-	49.6	144.8	186.0	274.2	250.0	C3'-exo
2AP/G 2	293.6	172.2	50.1	132.7	-	-	249.2	C1'-exo
2AP/T 1	-	-	49.8	144.7	185.1	274.7	250.0	C3'-exo
2AP/T 2	295.9	168.7	54.9	116.9	-	-	237.9	C1'-exo
Mean	294.3	170.4	51.4	133.3	185.3	274.6	245.1	
Range	2.9	7.3	6.0	42.4	2.4	1.8	23.3	

Table 7.7: Structural parameters for sugar-phosphate backbone of 2AP-containing dinucleotides. Data reproduced from reference [9]. Values for 5' nucleotide presented in top row, and for 3' nucleotide in bottom row for each nucleotide.

	Shift /Å	Slide /Å	Rise /Å	Tilt /°	Roll /°	Twist /°
2AP/A	0.84	-0.27	3.17	0.74	2.06	33.24
2AP/C	1.15	-0.39	3.06	2.53	-0.01	34.38
2AP/G	0.72	-0.20	3.05	4.28	-0.73	30.12
2AP/T	0.91	-0.30	2.91	5.59	-0.44	31.66
Mean	0.91	-0.29	3.05	3.29	0.22	32.35
Range	0.43	0.19	0.26	4.85	2.79	4.26

Table 7.8: Base-step parameters for 2AP-containing dinucleotides. Data reproduced from reference [9].

In the remainder of this chapter, results for 2AP-containing dinucleotides will be presented to show that the methodology presented by Smith *et al*[9] is reproducible, and results obtained under a similar process for pA-containing dinucleotides will be presented to show that it works for another non-canonical base. A further objective is to show that the more novel FBA pA doesn't perturb the DNA structure significantly and thereby complement work in other chapters of this thesis.

7.2 Methods

Geometry optimised structures of dinucleotides were obtained from DFT calculations with the functional M06-2X and the basis set 6-31+G*, implemented in Gaussian 16 on the Eddie computing cluster with Intel Xeon processors. Optimisation convergence criteria were tightened (opt=tight) to reduce the energy change allowed before the structure was accepted as optimised, ensuring a more precise energy minimum was found. An ultrafine integration grid was also used for the same reason. A polarisable continuum model was used to implicitly include solvation by water. Frequency calculations were performed on the final optimised structures to ensure that a true energy minimum was found, from the absence of imaginary frequencies.

Dinucleotides containing only the canonical bases with adenine at the 5' terminus were obtained from a Dickerson-Drew dodecamer crystal structure (4C64) downloaded from the PDB and mutated appropriately, so that all four possible combinations were prepared as initial structures for geometry optimisation. Dinucleotides containing 2AP and pA were obtained from the relevant optimised structure by mutation. All dinucleotides were prepared with an overall negative charge, due to the removal of one hydrogen from the phosphate group linking the two sugars. Any other phosphate groups were removed, in order to limit the size of the system.

Optimised dinucleotide geometries were extracted from Gaussian output files and saved as cartesian coordinate files in the Avogadro molecule viewer software package. These coordinate files were converted to the PDB standard file format for DNA structures using Babel in a Linux Ubuntu virtual machine. 2AP and pA had to be mutated back to adenine and the new structure saved separately, in order for the Babel software to recognise the structure as a proper DNA sequence. The PDB file format was required in order to use the open source 3DNA software,[5, 6, 8] also run in Linux, to calculate the dinucleotide base-step and sugar-phosphate backbone parameters reported in this work.

7.3 Results

7.3.1 Adenine- and 2AP-containing dinucleotides

Structural parameters for adenine- and 2AP-containing dinucleotides from DFT calculations in the current work are shown in Table 7.9 and Table 7.10, in order to establish that the previous work by Smith and colleagues could be reproduced here.[9] The structures shown in Figure 7.4 demonstrate visually that corresponding dinucleotides containing 2AP and adenine stack in a similar way, suggesting that 2AP does not significantly perturb DNA conformation, which is consistent with the findings of the authors of the previous work. It can also appears that there is a preference for stacking of the six-membered rings over stacking between the five-membered rings or mixed 5/6-membered ring stacking.

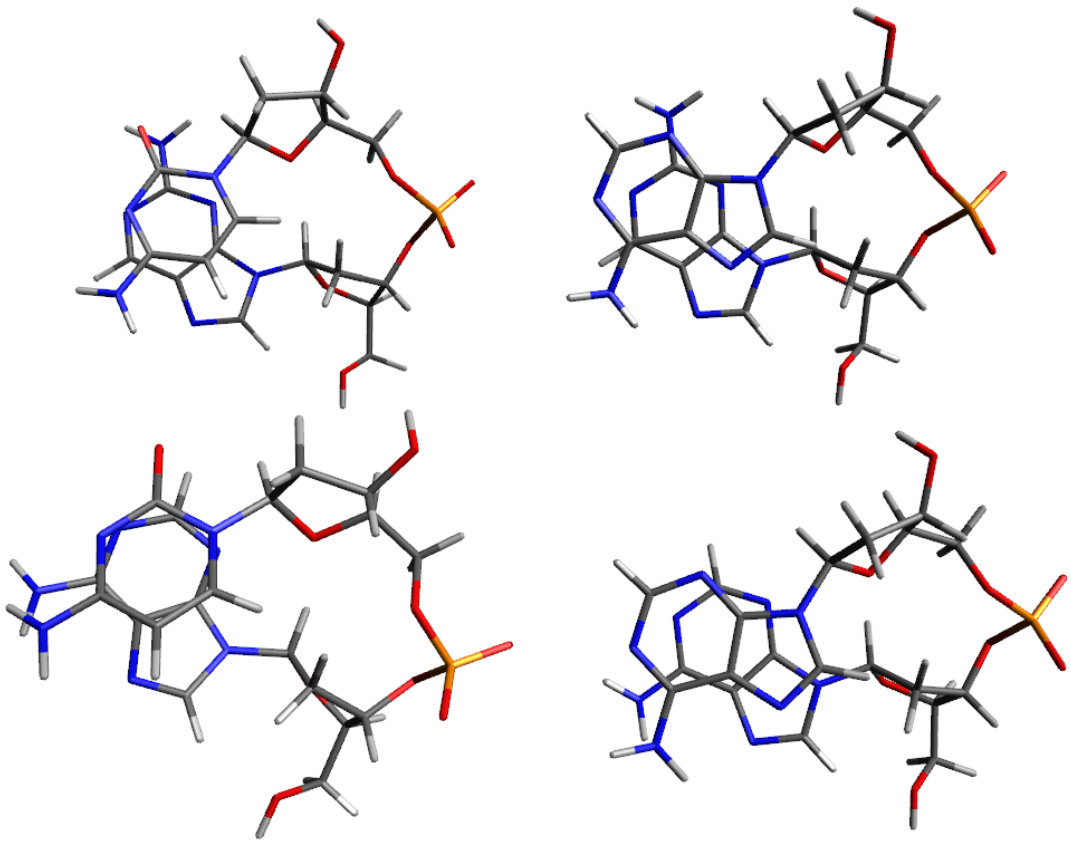

Figure 7.4: Examples of adenine- and 2AP-containing dinucleotide structures obtained from DFT calculations using the functional and basis set M06-2X/6-31+G*. Clockwise from top left: 2AP/C, 2AP/A, A/A, A/C.

Looking at the deoxyriboside puckering, almost all the dinucleotides listed in Table 7.9 have an O4'-endo sugar ring conformation at the 5' base and a C2'-endo sugar ring conformation for the remaining base. Likewise, the average structural

parameters shown in Table 7.9 are consistent with those reported by Smith *et al* in Table 7.5 and Table 7.7, taking into account the variation shown in the final row of each table. In particular, the δ and χ values previously mentioned as being especially unique to B-DNA are reasonably consistent with the previous work, although the average δ value is closer to the average shown for the dodecamer structure (Table 7.3) than for the optimised structures reported previously. This difference may be due to the tighter optimisation criteria mentioned in the methods, which would have led to a more precise energy minimum. In this aspect, it is not surprising that the geometries obtained here more closely match the ideal B-DNA conformation.

	α /°	β /°	γ /°	δ /°	ε /°	ζ /°	χ /°	sugar pucker
A/A 1	-	-	51.1	146.7	186.0	276.6	249.2	C2’-endo
A/A 2	294.7	167.0	55.6	100.4	-	-	229.2	O4’-endo
A/C 1	-	-	50.6	145.5	185.2	275.0	251.1	C3’-exo
A/C 2	292.5	166.7	53.6	76.8	-	-	216.8	C4’-exo
A/G 1	-	-	50.8	146.6	187.2	276.4	250.1	C2’-endo
A/G 2	293.8	165.8	54.9	91.5	-	-	226.8	O4’-endo
A/T 1	-	-	51.3	146.8	186.0	277.4	249.5	C2’-endo
A/T 2	294.5	166.7	55.3	91.2	-	-	223.5	O4’-endo
2AP/A 1	-	-	50.7	146.3	186.6	276.0	248.5	C2’-endo
2AP/A 2	294.2	166.9	55.3	100.8	-	-	229.3	O4’-endo
2AP/C 1	-	-	51.1	146.0	185.3	276.1	249.8	C2’-endo
2AP/C 2	293.7	165.6	55.1	78.5	-	-	215.1	O4’-endo
2AP/G 1	-	-	50.0	145.3	187.4	275.7	249.3	C3’-exo
2AP/G 2	294.1	167.0	54.1	101.6	-	-	233.3	O4’-endo
2AP/T 1	-	-	50.4	146.0	186.6	276.2	251.3	C2’-endo
2AP/T 2	293.8	166.5	54.8	92.1	-	-	228.3	O4’-endo
Mean	293.9	166.5	52.8	118.9	186.3	276.2	237.6	
Range	2.2	1.4	5.6	70	2.2	2.4	36.2	

Table 7.9: Structural parameters of sugar-phosphate backbone for adenine- and 2AP-containing dinucleotides optimised using DFT functional M06-2X/6-31+G*. Initial structures were obtained from Dickerson-Drew dodecamer (PDB code 4C64) in the case of adenine-containing dinucleotides, and from appropriate mutations of the relevant optimised adenine-containing dinucleotide for 2AP-containing dinucleotides. Values calculated from structural files using the 3DNA software package.[5, 6, 8] Values for 5’ nucleotide presented in top row, and for 3’ nucleotide in bottom row for each nucleotide.

Base-step parameters for the same dinucleotides structures are also shown in Table 7.10, where the average values across all dinucleotides are similar both to those shown in the previous work and those seen in the dodecamer oligonucleotide 4C64. This includes the rise and twist values characteristic of B-form structure. From these base-step parameters and the sugar-phosphate backbone structure discussed earlier, it seems reasonable to state that the structures obtained here from calculations have a B-DNA-type conformation, which is consistent with the previous report. Therefore the current approach using theoretical calculations on dinucleotides as a model for longer DNA strands is not only feasible, as established by the previous report, but reproducible in the current work.

	Shift /Å	Slide /Å	Rise /Å	Tilt /°	Roll /°	Twist /°
A/A	1.54	-0.38	3.11	2.45	0.53	36.85
A/C	1.29	-0.49	3.00	3.28	0.89	36.19
A/G	1.45	-0.40	3.05	3.66	-0.89	35.38
A/T	1.45	-0.66	2.91	4.67	2.39	33.63
2AP/A	1.31	-0.38	3.13	1.91	-0.77	35.09
2AP/C	1.55	-0.49	3.14	1.62	-1.90	37.41
2AP/G	0.99	-0.36	3.05	4.04	-2.38	31.68
2AP/T	1.15	-0.41	2.98	4.33	-1.02	32.39
Mean	1.34	-0.45	3.05	3.25	-0.39	34.83
Range	0.56	0.30	0.23	3.05	4.77	5.73

Table 7.10: Base-step parameters for adenine- and 2AP-containing dinucleotides optimised using DFT functional M06-2X/6-31+G*. Initial structures were obtained from Dickerson-Drew dodecamer (PDB code 4C64) in the case of adenine-containing dinucleotides, and from appropriate mutations of the relevant optimised adenine-containing dinucleotide for 2AP-containing dinucleotides. Values calculated from structural files using the 3DNA software package.[5, 6, 8]

7.3.2 pA-containing dinucleotides

Figure 7.5 shows optimised geometries of pA-containing dinucleotide structures obtained from DFT calculations. It can be seen that, as for canonical and 2AP-containing dinucleotides, base stacking is observed, but the nature of the stacking between pA and the natural bases is dependent on the ordering of the two bases and the identity of the adjacent natural base. When pA is substituted at the 5' terminus (right-hand column in Figure 7.4), base stacking occurs as seen previously, with the natural base positioned over the 'adenine-like' moiety. In contrast, when pA is

substituted at the 3’ terminus (left-hand column in Figure 7.4), the nature of base stacking changes noticeably, particularly for stacking between pA and the pyrimidines. This suggests that in dinucleotides at least, the extended aromatic system of pA allows additional modes of base-stacking to occur that are not available for canonical adenine, or even for smaller FBAs such as 2AP. It is still possible that in longer oligonucleotide strands, the presence of two adjacent bases to either side of pA will induce ‘competition’ between stacking with adjacent bases, limiting the population of ‘alternatively’ stacked pA bases. Additionally, the dependence on sequence context suggests that base-stacking between pA and adjacent bases is affected by the face of pA stacked with the adjacent base. This has been demonstrated in previous work by Mourik & Hogan[15] where twist angles of dimers are shown to be significantly affected by the facial conformation of adjacent bases. In dinucleotides, this effect is likely tempered by the constraints imposed from the presence of the sugar-phosphate backbone, so the final conformation is a combination of both the backbone and the stacking preference of different faces.

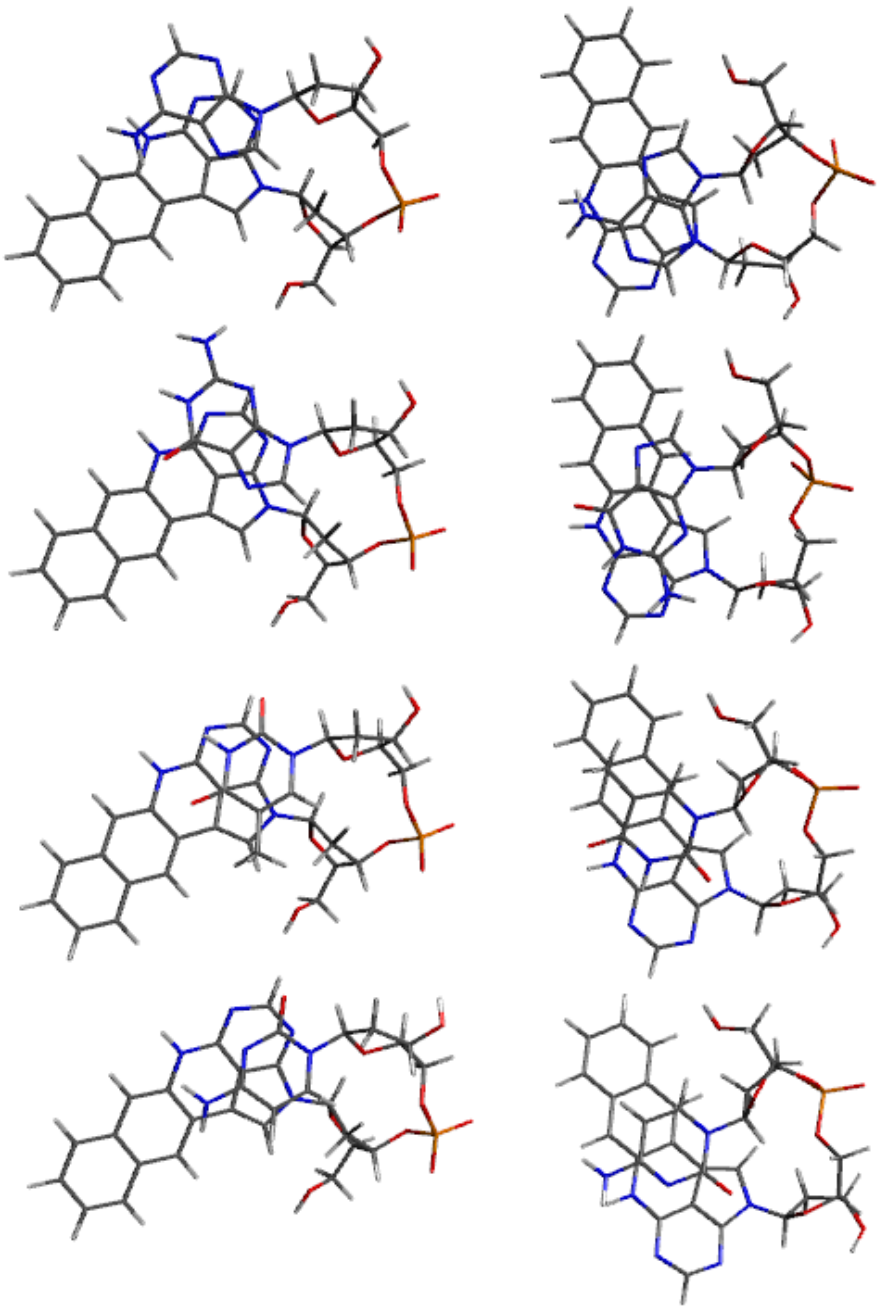

Figure 7.5: Dinucleotides containing pA at the 3’ position (left) and at the 5’ position (right), with the remaining base (from top to bottom) adenine, guanine, thymine and cytosine. Structures were obtained from geometry optimisations using DFT functional M06-2X/6-31+G*.

	α /°	β /°	γ /°	δ /°	ε /°	ζ /°	χ /°	sugar-pucker
A/pA 1	-	-	50.2	146.8	188.4	276.8	248.9	C3'-exo
A/pA 2	292.1	167.2	53.8	99.1	-	-	232.1	O4'-endo
C/pA 1	-	-	51.2	144.3	174.1	260.5	244.6	C2'-endo
C/pA 2	291.4	200.9	50.2	143.9	-	-	266.2	C3'-exo
G/pA 1	-	-	51.4	146.9	167.9	265.1	248.3	C2'-endo
G/pA 2	291.4	208.2	49.6	143.2	-	-	262.6	C3'-exo
T/pA 1	-	-	50.8	144.6	173.6	260.2	248.3	C2'-endo
T/pA 2	291.4	199	51.1	142.9	-	-	264.9	C3'-exo
pA/A 1	-	-	50.6	146.0	186.2	276.9	247.8	C2'-endo
pA/A 2	295	165.9	56.0	92.5	-	-	222.2	O4'-endo
pA/C 1		-	50.4	144.9	185.7	275.8	247.3	C2'-endo
pA/C 2	293.1	166.2	54.3	75.8	-	-	213.8	C4'-exo
pA/G 1	-	-	50.4	145.3	186.5	276.5	246.7	C2'-endo
pA/G 2	295.7	165.7	56.2	92.4	-	-	223.3	O4'-endo
pA/T 1	-	-	50.1	145.1	186.8	276.8	247.8	C2'-endo
pA/T 2	294.3	166.6	55.1	92.0	-	-	224.3	O4'-endo
Mean	293.1	180.0	52.8	118.9	181.2	271.1	243.1	
Range	4.3	42.5	5.6	70	20.5	16.7	52.4	

Table 7.11: Structural parameters of the sugar-phosphate backbone for pA-containing dinucleotides obtained from geometry optimisations using DFT (M06-2X/6-31+G*). Starting structures were obtained by mutating the relevant adenine-containing dinucleotides themselves obtained from previous calculations. Data for each base in the dinucleotides is shown on separate rows in order from the 5' terminus to the 3' terminus. Values calculated from structural files using the 3DNA software package.[5, 6, 8]

Visual inspection of the optimised pA-dinucleotide sequences in Figure 7.5 shows that there is still a preference for stacking between six-membered rings, as noted previously for 2AP-containing dinucleotides, but not in every case. There is a greater variety of stacking arrangements here, likely as a result of pA's extended ring system. Comparing the sugar-phosphate backbone parameters in Table 7.11 of the dinucleotides shown in Figure 7.5, the sugar puckering shows almost perfect correlation with B-form DNA, with O4'-endo for the sugar at the 5' terminus and C2'-endo for the remaining sugar. Only A/pA shows a different sugar conformation (C3'-exo) at the 3' terminus, while C/pA, G/pA, T/pA, and pA/C have sugars at the 5' terminus with a C4'-exo pucker. Values for backbone angles (Table 7.11) measured are again similar to those obtained for equivalent 2AP dinucleotides, with the exception being β & ε angles that are larger for dinucleotides with pA at the 3' terminus. More pertinently, these average backbone structural parameters are closer in magnitude to those for the Dickerson-Drew dodecamer in Table 7.3, suggesting that generally pA-containing dinucleotides adopt a B-DNA-type conformation. However, it seems that dinucleotides with pA at the 5' terminus are more 'well-behaved' than those with pA at the 3' terminus.

	Shift /Å	Slide /Å	Rise /Å	Tilt /°	Roll /°	Twist /°
A/pA	1.35	-0.31	3.10	2.98	1.09	35.97
C/pA	-0.21	0.03	2.69	8.93	-2.02	37.47
G/pA	-0.48	-0.40	3.08	4.28	1.70	35.70
T/pA	-0.05	0.03	2.57	10.59	-3.47	39.73
pA/A	1.68	-0.51	3.15	1.63	-0.64	36.78
pA/C	1.55	-0.67	3.18	0.76	-1.20	37.90
pA/G	1.55	-0.58	3.05	4.24	-2.84	34.74
pA/T	1.30	-0.61	2.95	4.36	-0.03	33.29
Mean	0.84	-0.38	2.97	4.72	-0.93	36.45
Range	2.16	0.70	0.61	9.83	5.17	6.44

Table 7.12: Base-step parameters for pA-containing dinucleotides obtained from geometry optimisations using DFT (M06-2X/6-31+G*). Starting structures were obtained by mutating the relevant adenine-containing dinucleotides themselves obtained from previous calculations. Data for each base in the dinucleotides is shown on separate rows in order from the 5' terminus to the 3' terminus. Values calculated from structural files using the 3DNA software package.[5, 6, 8]

As for the sugar-phosphate backbone structure, the base-step parameters for pA-containing dinucleotides in Table 7.12 are consistent both with 'ideal' B-DNA

base-step parameters in Table 7.2 and the previously shown example in Table 7.4 of a known B-form DNA structure. There does seem to be a distinction between dinucleotides with pA 3' or 5', particularly in the shift and slide parameters, as seen for the backbone torsional parameters. When pA is at the 5'-terminus, the base-step parameters are consistent with a B-form conformation and show little variation, regardless of the identity of the base at the 3'-terminus. However, distinct behaviour was observed for purine or pyrimidine bases when pA was 3'. B-form conformations were still observed, but there was greater variation in the structural parameters obtained for each sequence. These geometries showed different relative horizontal translation (shift/slide parameters) between the two bases, as well as greater variation in the twist parameter, depending on the identity of the 5'-positioned natural base. Given that the twist represents rotation of one base relative to the adjacent 5' base, along the z-axis parallel to the sugar-phosphate backbone, the altered relative horizontal translation and twist parameters may be directly related. In combination, the base-step and backbone torsional parameters suggest that pA-containing dinucleotides in solution have a conformation consistent with B-form, and that there is some distinct behaviour depending on whether pA is at the 3' or 5' terminus, particularly regarding horizontal translation (shift/slide) between adjacent bases, the β & ε backbone torsional parameters, and the sugar pucker of the pA nucleotide.

7.4 Discussion

In some senses, a major question posed in this chapter has largely been answered: can pA-substituted dinucleotide strands obtained from structure calculations adopt a similar conformation to natural DNA? The answer would seem to be yes, based on the results presented earlier. This is strongly supported by CD measurements of pA-containing oligonucleotides in solution which are indicative of a B-form structure,[16] with only minor differences reported between equivalent canonical and substituted oligonucleotides. Melting temperatures of double-stranded pA-substituted oligonucleotides were also reported to show minimal changes compared to the equivalent unsubstituted oligonucleotide.[16, 17] Having showed that the computational approach taken by Smith *et al*[9] can be extended to pA, it suggests that this approach is generally applicable to FBAs, given the complexity of the behaviour seen previously for pA.[16, 17] It does need to be stressed that the work presented earlier only proves that pA-containing dinucleotides can form B-DNA-like structures, not

that they do. However, this method 'predicts' B-DNA structure for natural base only and 2AP-containing dinucleotides, so a similar prediction for pA-substituted dinucleotides is encouraging. Further evidence from computation would require an extensive search of the conformational space. A previous attempt[18] to do so for 2AP-containing dinucleotides showed a large and complicated conformational space, which did not yield easily interpreted results (this study was only published as a thesis appendix). It is questionable how feasible this approach would be for an even more complex FBA like pA.

There are more findings that can be extracted from these data. The extended aromatic system of pA makes it likely that alternative stacking arrangements will be present that are not available to canonical DNA bases, or even smaller FBAs such as 2AP. As stated earlier, it appears that pA dinucleotides behave in a distinct manner when substituted at the 5' terminus compared to substitution at the 3' terminus. Furthermore, there is a noticeable difference in horizontal translation of adjacent bases for pA at the 3' terminus, which can also be seen by inspection of the optimised structures in Figure 7.5 shown earlier. Dinucleotides C/pA, T/pA in particular show a distinct stacking structure between the two adjacent bases, with the canonical base interacting with the extended part of pA, rather than the adenine-like moiety. To a lesser extent, G/pA also shows deviation from the expected stacking behaviour. Yet there does not appear to be any significant difference in the remaining base-step and backbone torsional parameters, with the exception of β & ε.

Given that both β & ε in the suite of backbone torsional parameters, as well as the sugar pucker, are significantly different where the alternative stacking arrangement is observed, it seems feasible that these changes are all inter-related. Before continuing, the angles denoted β & ε, both of which relate to the bonds between sugar and phosphate groups, should be looked at in more detail. Both β & ε represent dihedral angles encompassing bonds connecting the sugar and phosphate groups, as can be seen in Figure 7.3 earlier. These two dihedral angles in combination, which likely affect the relative position of adjacent bases more than the other backbone parameters, are likely to be strongly correlated with horizontal translation of adjacent bases in an oligonucleotide structure. This correlation implies that the sugar-phosphate backbone constrains the possible stacking arrangements of adjacent nucleotides, which is borne out by the β & ε values for C/pA, G/pA and T/pA. In these three

sequences, reduced β and increased ε results in an increased twist angle. In addition, puckering of the sugar in the pA nucleotide in the same dinucleotides (C3'-exo) was different to that in other dinucleotides at the 3' terminus (O4'-endo). Taken together, although the extended size of the pA analogue allows additional base stacking arrangements, the sugar-phosphate backbone still plays an important role in determining which stacking arrangement is adopted.

It is also instructive to consider the implications thrown up by the fact that pA is capable of multiple stacking arrangements, and moreover that the largest deviations from the expected stacking behaviour occur for C/pA and T/pA, as well as for G/pA to a smaller extent. Although A/pA does stack in the traditional manner between the adenine-like moiety of pA, it also has sugar-phosphate backbone conformation within the expected range of B-DNA, providing further confirmation that the sugar-phosphate backbone is important to observed base-stacking. However, it may be that adenine has significant preference for stacking with the adenine-like part of pA, providing evidence for the logical inference that observed base-stacking is determined by the combined effects of backbone conformation and π-stacking between adjacent bases. In general, the distinct stacking behaviour seen for pA at the 5' or 3' terminus is further confirmation of the importance of the backbone in constraining the possible base-stacking geometries. It should be noted that a different face of pA will interact with the adjacent natural base for 5'- or 3'-positioned pA, and a previous literature report by Mourik and Hogan[15] showed that stacking of adenine dimers depends on whether the bases are arranged 'face-to-face' or 'face-to-back'. Regardless, the main conformational effect reported by the authors is in the twist angle of the two bases, and the difference in energy was small. It is therefore likely that in dinucleotide system where the bases are not completely free to rotate to the otherwise most favourable arrangement, the effect of differential interactions between distinct faces is negligible.

The work discussed in this chapter is highly relevant to previous work, both in the previous chapter of this thesis and other literature sources.[16, 17] In Chapter 6, the proposed explanation for the measured solution phase fluorescence of pAr in the presence of the natural bases was excited state proton transfer involving the tautomers of pAr. It was shown in the previous chapter that the observed fluorescence of pAr was only affected by the natural bases through a static quenching process, i.e. due to formation of a dimer. There is no immediately obvious reason to assume that different

excited state processes occur for pA in a dinucleotide than for pA-natural base dimers in solution. It is also reasonable to assume that the efficiency of ESPT will depend on the relative orientation and position of the two bases. Therefore the altered structure for corresponding 5' or 3' pA dinucleotides shown earlier suggests that decay of the excited state is indirectly affected by the dinucleotide conformation. Given the already shown suitability of dinucleotides as a model for larger oligonucleotide sequences, it seems appropriate that the impact of sequence context and conformation on the fluorescence emission of pAr would also apply to oligonucleotides. This can be seen in fluorescence quantum yield measurements[16] of sequences denoted AG (adenine 5' relative to pA) and GA (guanine 5' relative to pA) in the work by Bood *et al* with quantum yields of 24 % and 42 %, respectively. These are only two examples in the previous published work, but this sequence context effect was also seen for the other reported sequences.

7.5 Conclusions

In this chapter, it was shown that DFT calculations can successfully be used not only to predict conformation of DNA, but also to draw deeper inferences about the conformational behaviour of pA-containing oligonucleotides. Calculations on 2AP-containing dinucleotides were used to show that the approach taken in previous work[9] is reproducible and that a B-DNA type structure was reliably obtained from calculations on systems known to form B-DNA structures in solution. Using this approach for the novel fluorescent base analogue pA, it was found that a B-form DNA structure exists for pA-containing dinucleotides, based solely on helical parameters.

However, some key differences were seen between dinucleotides containing adenine or guanine, and those containing cytosine or thymine. Examining the ball-and-stick structural representations of geometry-optimised pA-containing dinucleotides in Figure 7.5, it was seen that natural bases at the 5'-position stacked in a similar fashion to that seen for structures shown in the introduction. Where the natural base was attached to the 3'-position, in contrast, it was found that cytosine and thymine did not interact with the same part of the pA moiety, although adenine and guanine were still found to stack with pA in the canonical way. This marked a clear distinction between the way purines and pyrimidines interact with adjacent pA, which in concert with the sugar-phosphate backbone, particularly dihedral angles involving

the bridging phosphate group, gave rise to the observed distinct behaviour of the pyrimidine-pA dinucleotides.

In summary, it was found that using the system of classification of dinucleotide structures described here, pA-containing dinucleotides formed structures consistent with a B-form type DNA conformation. In addition, stacking behaviour between adjacent bases was shown to be dependent not just on base identity, but on which face (3' or 5') the adjacent base was positioned. Further work that could be carried out would be to perform calculations on equivalent systems without the sugar-phosphate backbone, as this would provide an indication of the impact on conformation solely from base-stacking without the constraint of the backbone. It is likely that a greater variety of stacking arrangements will be seen, due to the absence of the extra structural constraints imposed by the sugar–phosphate backbone. Existing differences due to sequence context discussed earlier may be amplified. A related effect can be seen in the previous work on adenine and 2AP by Mourik and Hogan.[15] Another interesting line of research would be to look at the effect of different tautomers on the obtained geometry, particularly for pA-natural base dimers which have less structural constraints. This may admittedly have negligible impact and be computationally expensive as well as time-consuming, however it may not be necessary for every sequence context discussed in this chapter.

7.6 References

1. R. E. Dickerson, *Nucleic Acids*, International Union of Crystallography, 2006.
2. R. E. Dickerson, *Nucleic Acids Research*, 1989, **17**, 1797-1803.
3. J. Sponer, A. Mladek, J. E. Sponer, D. Svozil, M. Zgarbova, P. Banas, P. Jurecka and M. Otyepka, *Physical Chemistry Chemical Physics*, 2012, **14**, 15257-15277.
4. L. Lercher, M. A. McDonough, A. H. El-Sagheer, A. Thalhammer, S. Kriaucionis, T. Brown and C. J. Schofield, *Chemical communications (Cambridge, England)*, 2014, **50**, 1794-1796.
5. X. J. Lu and W. K. Olson, *Nucleic Acids Research*, 2003, **31**, 5108-5121.
6. X.-J. Lu and W. K. Olson, *Nat. Protocols*, 2008, **3**, 1213-1227.
7. W. K. Olson, M. Bansal, S. K. Burley, R. E. Dickerson, M. Gerstein, S. C. Harvey, U. Heinemann, X. J. Lu, S. Neidle, Z. Shakked, H. Sklenar, M. Suzuki, C. S. Tung, E. Westhof, C. Wolberger and H. M. Berman, *Journal of Molecular Biology*, 2001, **313**, 229-237.
8. G. Zheng, X.-J. Lu and W. K. Olson, *Nucleic Acids Research*, 2009, **37**, W240-W246.
9. D. A. Smith, L. F. Holroyd, T. van Mourik and A. C. Jones, *Phys Chem Chem Phys*, 2016, **18**, 14691-14700.
10. T. A. Zubatiuk, O. V. Shishkin, L. Gorb, D. M. Hovorun and J. Leszczynski, *Physical Chemistry Chemical Physics*, 2013, **15**, 18155-18166.
11. W. C. Johnson JR. and I. Tinoco JR., *Biopolymers*, 1969, **7**, 727-749.
12. C. R. Cantor, M. M. Warshaw and H. Shapiro, *Biopolymers*, 1970, **9**, 1059-1077.
13. D. M. Cheng and R. H. Sarma, *Journal of the American Chemical Society*, 1977, **99**, 7333-7348.
14. F. S. Ezra, C.-H. Lee, N. S. Kondo, S. S. Danyluk and R. H. Sarma, *Biochemistry*, 1977, **16**, 1977-1987.
15. T. van Mourik and S. W. L. Hogan, *Structural Chemistry*, 2016, **27**, 145-158.
16. M. Bood, A. F. Fuchtbauer, M. S. Wranne, J. J. Ro, S. Sarangamath, A. H. El-Sagheer, D. L. M. Rupert, R. S. Fisher, S. W. Magennis, A. C. Jones, F. Hook, T. Brown, B. H. Kim, A. Dahlen, L. M. Wilhelmsson and M. Grøtli, *Chemical Science*, 2018, **9**, 3494-3502.
17. R. S. Fisher, University of Edinburgh, 2018.
18. L. Holroyd, University of St. Andrews, 2015.

Chapter 8 Conclusions

Throughout this thesis, different aspects of the effect of DNA bases on the fluorescence of the fluorescent base analogues (FBAs) 2AP and pA have been examined. In Chapters 4 and 6, it was shown that the effect of free DNA bases in solution on the fluorescence emission of both 2AP and pA bore striking similarity to that seen in dinucleotides or oligonucleotides. This suggests that the interactions between FBAs and DNA bases is due in large part to intermolecular, through-space interactions such as base-stacking. The similar effect of the presence of DNA bases on the fluorescence emission of 2AP and pA, even in the absence of the sugar-phosphate backbone, indicates a minor role for the backbone.

Of course, the backbone can't be neglected completely. A more detailed examination of the results in Chapter 4 shows that the fluorescence lifetimes of 2AP are qualitatively different to those in di- or oligonucleotides,[1] with at most three lifetime components, while 2AP-containing oligonucleotides have four lifetime components. Given that these 2AP lifetime components are widely accepted to represent different conformational states, clearly the extra structural constraints imposed by the presence of the backbone leads to extra conformational states of DNA, which in turn can be seen in the fluorescence decay. In Chapter 6, meanwhile, the fluorescence emission of free pA in solution was shown to generally exhibit similar behaviour in the presence of DNA bases as that previously reported[2, 3] for pA-containing oligonucleotides.

The limitations just mentioned notwithstanding, the approach shown in Chapters 4 and 6 has potential for simple testing of the feasibility of a novel FBA as a probe of DNA conformation. In the case of 2AP, static and dynamic quenching were successfully resolved independently and shown to be consistent with overall quenching in dinucleotides. Similarly, pA was shown to have consistent behaviour in free solution and in oligonucleotides. In addition, quenching or enhancement of pA fluorescence was found to proceed only *via* formation of a complex. These findings suggest strongly that not only is it not necessary to go to the expense of oligonucleotide incorporation in order to be able to predict the behaviour of a novel FBA, but that information can be obtained about the interactions, whether quenching or some other process, affecting fluorescence emission.

However, pA-containing oligonucleotides show a strong dependence on sequence context, such that an oligonucleotide with a given base 5' or 3' to pA exhibits different fluorescence emission behaviour. This phenomenon was not observed for free pA in solution, which is not an unreasonable outcome. A possible explanation for the observed behaviour of pA-containing oligonucleotides was presented in Chapter 7. DFT calculations on dinucleotide structures were used to show that the ordering of the two bases (i.e. whether pA is 5' or 3') noticeably changes the DNA conformation obtained. The observed structural differences correlate surprising well with previously reported fluorescence quantum yields of pA-containing oligonucleotides.[2] These optimised structures presented in Chapter 7 provide further confirmation that DFT calculation can predict much of the behaviour observed experimentally, even for extended systems like pA with complex behaviour. Hitherto, this has only been demonstrated for 2AP.[4]

Finally, in Chapter 5, it was shown that the efficiency of energy transfer from the natural bases to 2AP in 2AP-containing dinucleotides is linearly dependent on temperature over the temperature range 5-25 °C. Previously, energy transfer efficiency was only measured at room temperature (~20 °C) or 77 K using dinucleotides[5] as in this thesis, or at 5 °C using 2AP-containing oligonucleotides.[6] The results presented in this thesis provided clearer evidence that the conformation and dynamics of DNA, which is temperature-dependent, affected the excited state processes between 2AP and the adjacent natural bases, whether a phase change occurred or not.

In summary, the work presented in this thesis provides clear signs that initial testing of novel FBAs need not require expensive and time-consuming oligonucleotide incorporation. Simple, careful measurements of the fluorescence of novel FBAs in solution with free natural DNA bases is sufficient to predict behaviour of the same FBAs incorporated into oligonucleotides with reasonable reliability, and produce a list of candidates worthy of further investigation. DFT calculations can also be used to determine the likely effect of incorporation on DNA structure, at a minimum. Furthermore, many studies of the photophysical processes of FBAs in DNA rely on FBA-containing oligonucleotides, which has drawbacks, such as greater expense and increased uncertainty over linking observed behaviour to base identity. Reasons for using oligonucleotides rather than dinucleotides as a model for DNA may vary for different studies, but it is likely that there are some common justifications, such as

dinucleotides being a poor model for DNA structure. The work in Chapters 5 and 7 provide evidence to the contrary. Optimised dinucleotide geometries in Chapter 7 show that dinucleotides containing either 2AP or pA maintain B-DNA-like conformations, while energy transfer shown in Chapter 5 is highly dependent on interactions between adjacent bases and would likely be undetectable in a non-B-form conformation. This thesis therefore shows that the fluorescence behaviour of a FBA in DNA can be predicted using astoundingly simple models, that even measurements without a recognisable DNA structure at all can provide surprisingly useful and unforeseen findings.

8.1 Future Work

Several lines of further study from this thesis are possible. Similar calculations to those discussed in Chapter 7 on other recent examples of FBAs, such as the 6-azauridines,[7] could provide information about the effect of larger base analogues on DNA structure. Given that finding fluorescent molecules with longer wavelengths often means looking at larger molecules, these would be useful results to have. Looking at optimised structures of trinucleotides with pA sandwiched between two bases could also help to give more insight into the effect of base ordering on DNA conformation.

It would also be interesting to see if dimers of 2AP and natural bases in solution also undergo energy transfer, as this would demonstrate that many of the photophysical properties of FBAs observed in DNA can be replicated to some extent in bulk solution. It has been shown computationally[4] that 2AP-natural base dimers in solution still base stack, but their relative orientations are different than in DNA. Furthermore, all of the principles should in theory apply equally to RNA, which would be an interesting application for FBAs discussed in this thesis and elsewhere, given the much larger set of possible RNA structures.

In general, it would be interesting to apply the methods discussed in this thesis to other FBAs, which may help to provide systematic understanding of the relationship between the structure of a FBA and its fluorescence properties in DNA. This would undoubtedly be useful to researchers in the field, whether the desired outcome is a new fluorescent probe or label, with improved properties such as increased fluorescence brightness or longer emission/excitation wavelengths.

8.2 References

1. A. C. Jones and R. K. Neely, *Q Rev Biophys*, 2015, **48**, 244-279.
2. M. Bood, A. F. Fuchtbauer, M. S. Wranne, J. J. Ro, S. Sarangamath, A. H. El-Sagheer, D. L. M. Rupert, R. S. Fisher, S. W. Magennis, A. C. Jones, F. Hook, T. Brown, B. H. Kim, A. Dahlen, L. M. Wilhelmsson and M. Grøtli, *Chemical Science*, 2018, **9**, 3494-3502.
3. R. S. Fisher, University of Edinburgh, 2018.
4. D. A. Smith, L. F. Holroyd, T. van Mourik and A. C. Jones, *Phys Chem Chem Phys*, 2016, **18**, 14691-14700.
5. G. McKenzie, University of Edinburgh, 2017.
6. T. M. Nordlund, *Photochemistry and Photobiology*, 2007, **83**, 625-636.
7. R. W. Sinkeldam, P. A. Hopkins and Y. Tor, *ChemPhysChem*, 2012, **13**, 3350-3356.

Appendices

Appendix I

2AP Fluorescence lifetime data

Fluorescence lifetimes of 2AP in the presence of nucleoside monophosphates in phosphate buffer (100 mM). A-factors corrected for scattered light.

[rGMP] /M	τ_1 /ns	τ_2 /ns	τ_3 /ns	A_1	A_2	A_3	$\langle\tau\rangle$ /ns
0	5.66	-	-	1	-	-	5.66
$1x10^{-5}$	5.60	-	-	1	-	-	5.60
$5x10^{-5}$	5.62	-	-	1	-	-	5.62
$1x10^{-4}$	5.58	-	-	1	-	-	5.58
$5x10^{-4}$	5.57	1.95	0.03	0.98	0.02	0	5.50
$1x10^{-3}$	5.55	1.95	0.03	0.97	0.03	0	5.44
$5x10^{-3}$	5.24	1.95	0.03	0.97	0.03	0	5.14
0.01	4.89	1.95	0.03	0.90	0.04	0.07	4.48
0.02	4.40	1.95	0.03	0.86	0.05	0.10	3.88
0.03	4.06	1.95	0.03	0.55	0.03	0.41	2.30
0.04	3.84	1.95	0.03	0.37	0.02	0.61	1.48
0.05	3.70	1.95	0.03	0.30	0.02	0.68	1.17

[rCMP] /M	τ_1 /ns	τ_2 /ns	τ_3 /ns	A_1	A_2	A_3	$<\tau>$ /ns
0	5.81	-	-	1	-	-	5.81
$1x10^{-5}$	5.75	-	-	1	-	-	5.75
$5x10^{-5}$	5.72	-	-	1	-	-	5.72
$1x10^{-4}$	5.70	-	-	1	-	-	5.70
$5x10^{-4}$	5.67	-	-	1	-	-	5.67
$1x10^{-3}$	5.65	0.62	0.05	0.98	0.02	0	5.55
$5x10^{-3}$	5.39	0.62	0.05	0.76	0.21	0.03	4.22
0.01	5.11	0.62	0.05	0.96	0.04	0	4.93
0.02	4.63	0.62	0.05	0.90	0.05	0.05	4.20
0.03	4.26	0.62	0.05	0.86	0.06	0.08	3.70
0.04	3.92	0.62	0.05	0.83	0.07	0.10	3.30
0.05	3.66	0.62	0.05	0.76	0.08	0.16	2.84

[rIMP] /M	τ_1 /ns	τ_2 /ns	τ_3 /ns	A_1	A_2	A_3	$<\tau>$ /ns
0	5.62	-	-	1	-	-	5.62
$1x10^{-5}$	5.55	-	-	1	-	-	5.55
$5x10^{-5}$	5.55	-	-	1	-	-	5.55
$1x10^{-4}$	5.55	-	-	1	-	-	5.55
$5x10^{-4}$	5.55	-	-	1	-	-	5.55
$1x10^{-3}$	5.57	2.61	0.09	0.97	0.03	0	5.48
$5x10^{-3}$	5.39	2.61	0.09	0.96	0.04	0	5.28
0.01	5.17	2.61	0.09	0.95	0.05	0	5.04
0.02	4.84	2.61	0.09	0.89	0.06	0.05	4.47
0.03	4.58	2.61	0.09	0.85	0.08	0.07	4.11
0.04	4.38	2.61	0.09	0.81	0.11	0.08	3.84
0.05	4.18	2.61	0.09	0.75	0.13	0.11	3.48

Separate fitting (not global analysis) of 2AP-rGMP decay data.

[rGMP] /M	τ_1 /ns	τ_2 /ns	τ_3 /ns	A_1	A_2	A_3	$<\tau>$ /ns
0	5.67	-	-	1	-	-	5.67
$1x10^{-5}$	5.60	-	-	1	-	-	5.60
$5x10^{-5}$	5.62	-	-	1	-	-	5.62
$1x10^{-4}$	5.58	-	-	1	-	-	5.58
$5x10^{-4}$	5.54	-	-	1	-	-	5.54
$1x10^{-3}$	5.52	-	-	1	-	-	5.52
$5x10^{-3}$	5.24	1.82	-	0.94	0.06	-	5.12
0.01	4.89	1.76	-	0.96	0.04	-	4.76
0.02	4.41	2.36	0.06	0.76	0.05	0.19	3.49
0.03	4.04	1.61	0.05	0.48	0.02	0.50	1.98
0.04	3.82	1.72	0.034	0.18	0.01	0.81	0.72
0.05	3.67	0.92	0.03	0.10	0.00	0.90	0.39

Fluorescence lifetimes of 2AP in the presence of dTMP in tris-HCl (20 mM). A-factors corrected for scattered light. Decays fitted separately, not globally.

[dTMP] /M	τ_1 /ns	τ_2 /ns	τ_3 /ns	A_1	A_2	A_3	$<\tau>$ /ns
0	11.95	-	-	1	-	-	11.95
$1x10^{-5}$	11.91	-	-	1	-	-	11.91
$5x10^{-5}$	11.87	-	-	1	-	-	11.87
$1x10^{-4}$	11.83	-	-	1	-	-	11.83
$5x10^{-4}$	11.72	-	-	1	-	-	11.72
$1x10^{-3}$	11.57	-	-	1	-	-	11.57
$5x10^{-3}$	10.82	6.82	-	0.89	0.11	-	10.40
0.01	9.63	6.03	0.25	0.88	0.09	0.04	8.98
0.02	7.92	4.51	0.10	0.83	0.08	0.09	6.92
0.03	6.65	2.93	0.10	0.84	0.05	0.11	5.74
0.04	5.76	2.10	0.09	0.80	0.05	0.16	4.70
0.05	5.09	1.56	0.07	0.74	0.05	0.22	3.83

Fluorescence lifetimes of 2AP in the presence of riboside bases in tris-HCl buffer (20 mM). A-factors corrected for scattered light.

[rA] /M	τ_1 /ns	τ_2 /ns	τ_3 /ns	A_1	A_2	A_3	$\langle\tau\rangle$ /ns
0	10.41	-	-	1	-	-	10.41
$3x10^{-6}$	10.43	-	-	1	-	-	10.43
$1x10^{-5}$	10.39	-	-	1	-	-	10.39
$3x10^{-5}$	10.38	-	-	1	-	-	10.38
$1x10^{-4}$	10.36	-	-	1	-	-	10.36
$3x10^{-4}$	10.32	-	-	1	-	-	10.32
$1x10^{-3}$	10.10	1.89	0.11	0.98	0.02	0	9.94
$3x10^{-3}$	9.82	1.89	0.11	0.97	0.03	0.00	9.58
$6x10^{-3}$	9.29	1.89	0.11	0.95	0.04	0.01	8.90
$9x10^{-3}$	8.87	1.89	0.11	0.93	0.05	0.02	8.35
0.012	8.47	1.89	0.11	0.90	0.05	0.04	7.72
0.014	8.16	1.89	0.11	0.88	0.06	0.06	7.30

[rC] /M	τ_1 /ns	τ_2 /ns	τ_3 /ns	A_1	A_2	A_3	$\langle\tau\rangle$ /ns
0	10.52	-	-	1	-	-	10.52
$4x10^{-5}$	10.47	-	-	1	-	-	10.47
$2x10^{-4}$	10.42	-	-	1	-	-	10.42
$4x10^{-4}$	10.36	-	-	1	-	-	10.36
$2x10^{-3}$	9.91	0.51	0.09	0.89	0.05	0.07	8.85
$4x10^{-3}$	9.52	0.51	0.09	0.84	0.08	0.08	8.04
0.02	7.33	0.51	0.09	0.56	0.28	0.17	4.26
0.04	5.76	0.51	0.09	0.39	0.39	0.22	2.47
0.08	4.13	0.51	0.09	0.23	0.47	0.30	1.22
0.12	3.26	0.51	0.09	0.16	0.48	0.36	0.80
0.16	2.71	0.51	0.09	0.12	0.48	0.40	0.61
0.20	2.36	0.51	0.09	0.09	0.47	0.44	0.49

Static Quenching

Plots of $1/A_1$ from 2AP (100 mM phosphate buffer) in the presence of nucleoside monophosphates, using corrected A-factors. Red points have been excluded from fit.

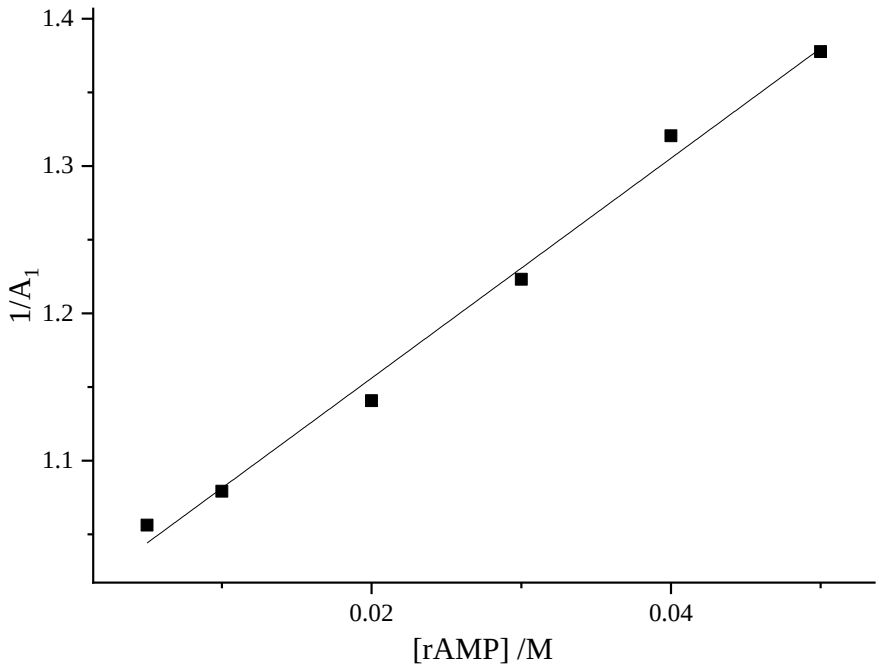

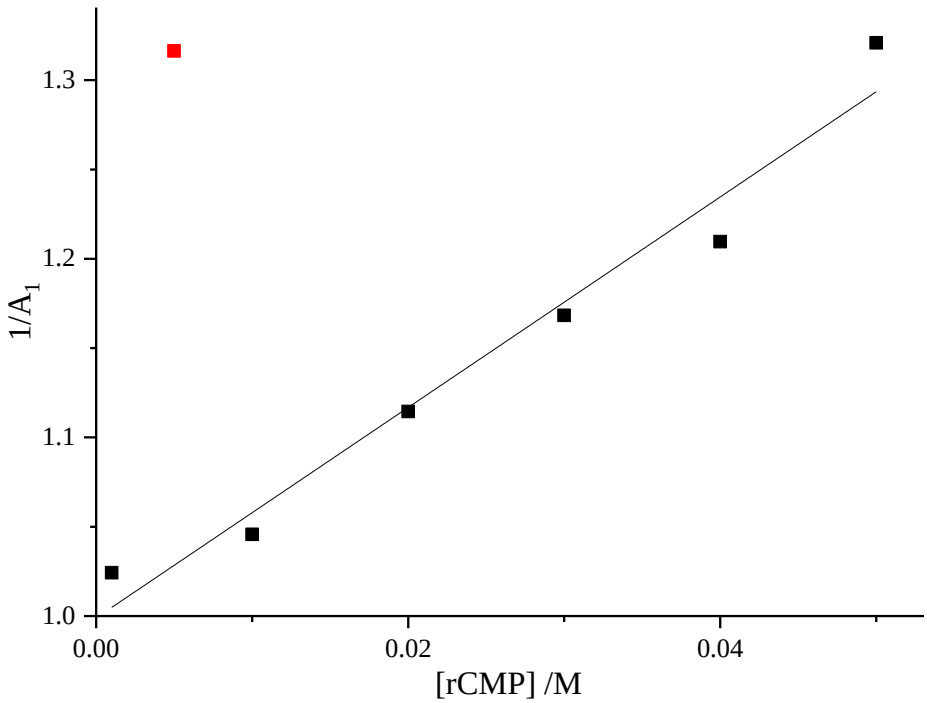

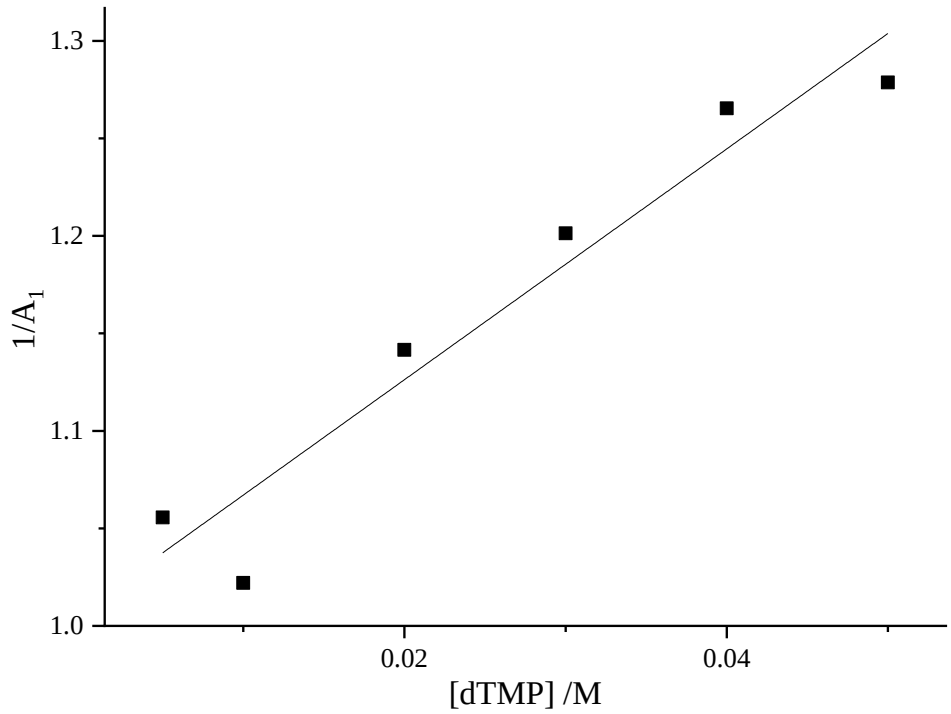
1.3
1.2
1.1
1.0
1/A1
0.02
0.04
[dTMP] /M

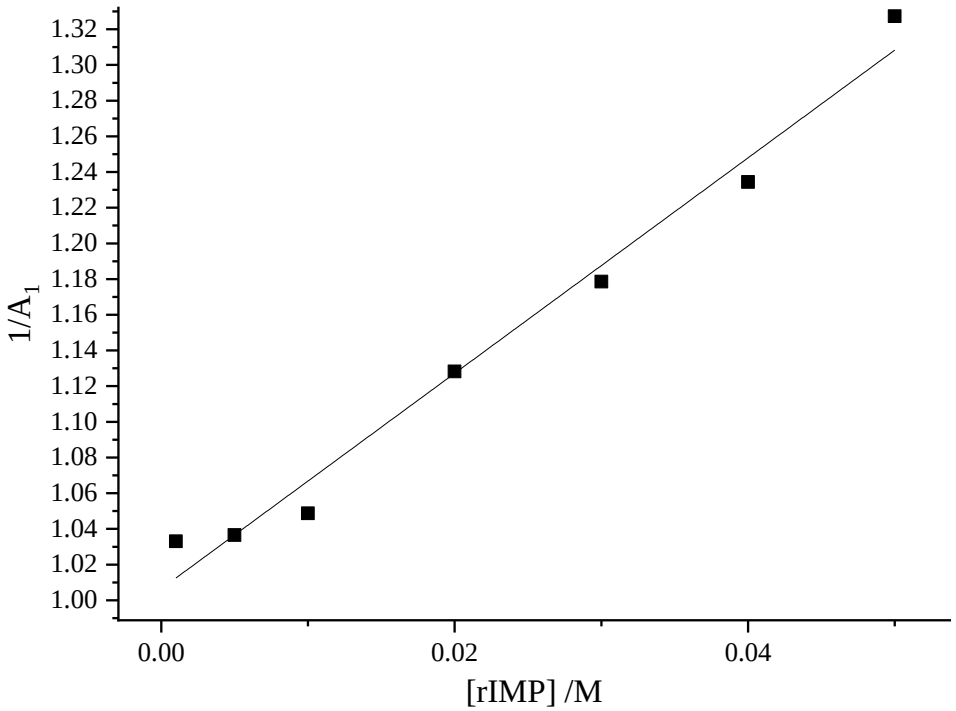
1.32
1.30
1.28
1.26
1.24
1.22
1.20
1.18
1.16
1.14
1.12
1.10
1.08
1.06
1.04
1.02
1.00
1/A1
0.00
0.02
0.04
[rIMP] /M

Appendix II

2AP-containing dinucleotide time-resolved fluorescence data

Emission at 360 nm for 2AP/A

Excitation wavelength /nm	260		310	
Temperature /°C	τ_i /ns	A_i	τ_i /ns	A_i
5	10.18	0.06	10.07	0.11
	3.07	0.09	2.93	0.14
	0.91	0.54	0.74	0.36
	0.29	0.31	0.18	0.39
10	10.07	0.06	9.97	0.10
	2.96	0.09	2.84	0.15
	0.86	0.53	0.72	0.34
	0.29	0.31	0.16	0.41
15	9.80	0.06	9.77	0.10
	2.66	0.11	2.60	0.16
	0.78	0.56	0.67	0.34
	0.24	0.27	0.15	0.40
20	9.63	0.06	9.65	0.10
	2.65	0.10	2.59	0.16
	0.76	0.56	0.78	0.31
	0.22	0.28	0.18	0.42
25	9.43	0.06	9.44	0.09
	2.49	0.11	2.34	0.17
	0.74	0.54	0.64	0.33
	0.24	0.29	0.12	0.41

Emission at 360 nm for 2AP/G

Excitation wavelength /nm	260		310	
Temperature /°C	τ_i /ns	A_i	τ_i /ns	A_i
5	10.47	0.09	10.14	0.09
	2.48	0.06	2.54	0.15
	0.49	0.05	0.45	0.12
	0.06	0.80	0.07	0.64
10	10.34	0.08	9.97	0.08
	2.33	0.06	2.31	0.16
	0.48	0.06	0.45	0.11
	0.05	0.80	0.07	0.65
15	10.13	0.09	9.76	0.06
	2.12	0.08	2.10	0.14
	0.45	0.05	0.43	0.08
	0.05	0.78	0.06	0.71
20	9.94	0.10	9.56	0.06
	1.92	0.08	1.90	0.15
	0.42	0.06	0.36	0.09
	0.05	0.78	0.05	0.70
25	9.72	0.10	9.34	0.05
	1.79	0.09	1.73	0.15
	0.42	0.06	0.35	0.08
	0.05	0.74	0.05	0.71

Emission at 360 nm for 2AP/T

Excitation wavelength /nm	260		310	
Temperature /°C	τ_i /ns	A_i	τ_i /ns	A_i
5	9.35	0.02	9.09	0.02
	3.36	0.13	3.40	0.25
	0.48	0.09	0.46	0.14
	0.06	0.77	0.07	0.59
10	9.55	0.02	9.54	0.02
	3.08	0.14	3.12	0.29
	0.47	0.09	0.46	0.13
	0.06	0.75	0.08	0.55
15	9.49	0.02	9.41	0.02
	2.80	0.15	2.83	0.29
	0.42	0.09	0.45	0.13
	0.05	0.74	0.07	0.56
20	9.54	0.02	9.40	0.02
	2.54	0.16	2.54	0.31
	0.39	0.09	0.40	0.12
	0.05	0.73	0.07	0.55
25	9.52	0.02	9.44	0.02
	2.31	0.20	2.32	0.32
	0.40	0.08	0.40	0.11
	0.06	0.70	0.07	0.55

Emission at 400 nm for 2AP/A

Excitation wavelength /nm	260		310	
Temperature /°C	τ_i /ns	A_i	τ_i /ns	A_i
5	10.18	0.07	10.07	0.12
	3.07	0.09	2.93	0.15
	0.91	0.55	0.74	0.36
	0.29	0.29	0.18	0.37
10	10.07	0.07	9.97	0.11
	2.96	0.10	2.84	0.15
	0.86	0.54	0.72	0.36
	0.29	0.29	0.16	0.37
15	9.80	0.07	9.77	0.11
	2.66	0.11	2.60	0.17
	0.78	0.57	0.67	0.36
	0.24	0.26	0.15	0.36
20	9.63	0.07	9.65	0.12
	2.65	0.10	2.59	0.18
	0.76	0.56	0.78	0.33
	0.22	0.27	0.18	0.37
25	9.43	0.07	9.44	0.10
	2.49	0.11	2.34	0.18
	0.74	0.54	0.64	0.33
	0.24	0.28	0.12	0.38

Emission at 400 nm for 2AP/G

Excitation wavelength /nm	260		310	
Temperature /°C	τ_i /ns	A_i	τ_i /ns	A_i
5	10.47	0.09	10.14	0.09
	2.48	0.06	2.54	0.16
	0.49	0.07	0.45	0.13
	0.06	0.78	0.07	0.62
10	10.34	0.09	9.97	0.08
	2.33	0.06	2.31	0.12
	0.48	0.06	0.45	0.17
	0.05	0.78	0.07	0.63
15	10.13	0.10	9.76	0.08
	2.12	0.08	2.10	0.18
	0.45	0.08	0.43	0.13
	0.05	0.75	0.06	0.61
20	9.94	0.09	9.56	0.07
	1.92	0.08	1.90	0.19
	0.42	0.07	0.36	0.13
	0.05	0.76	0.05	0.61
25	9.72	0.11	9.34	0.07
	1.79	0.10	1.73	0.20
	0.42	0.08	0.35	0.12
	0.05	0.72	0.05	0.61

Emission at 400 nm for 2AP/T

Excitation wavelength /nm	260		310	
Temperature /°C	τ_i /ns	A_i	τ_i /ns	A_i
5	9.35	0.02	9.09	0.03
	3.36	0.14	3.40	0.28
	0.48	0.10	0.46	0.16
	0.06	0.75	0.07	0.54
10	9.55	0.02	9.54	0.03
	3.08	0.15	3.12	0.30
	0.47	0.10	0.46	0.14
	0.06	0.73	0.08	0.53
15	9.49	0.02	9.41	0.02
	2.80	0.17	2.83	0.32
	0.42	0.10	0.45	0.14
	0.05	0.72	0.07	0.52
20	9.54	0.01	9.40	0.02
	2.54	0.18	2.54	0.34
	0.39	0.10	0.40	0.13
	0.05	0.70	0.07	0.51
25	9.52	0.02	9.44	0.02
	2.31	0.23	2.32	0.36
	0.40	0.10	0.40	0.13
	0.06	0.65	0.07	0.48

2AP-containing dinucleotide energy transfer efficiency

Based on emission at 360 nm, allowing for energy transfer across all lifetime components.

Temperature /°C	2AP/A /%	2AP/G /%	2AP/T /%
5	30	9	23
10	27	8	22
15	24	4	18
20	23	4	17
25	19	3	9

Based on emission at 400 nm, allowing for energy transfer across all lifetime components.

Temperature /°C	2AP/A /%	2AP/G /%	2AP/T /%
5	30	8	25
10	27	8	22
15	25	6	19
20	24	6	18
25	19	5	11

Appendix III

pAr fluorescence lifetimes

Separately fitted pAr fluorescence decay data as a function of NMP.

[rAMP] /M	τ_1 /ns	τ_2 /ns	τ_3 /ns	A_1	A_2	A_3	$<\tau>$/ns
0	6.15	3.53	0.17	0.58	0.06	0.36	3.84
$1x10^{-5}$	6.17	4.22	0.16	0.56	0.08	0.36	3.85
$5x10^{-5}$	6.21	4.53	0.17	0.56	0.10	0.34	3.99
$1x10^{-4}$	6.23	4.32	0.18	0.56	0.10	0.34	3.98
$5x10^{-4}$	6.23	4.06	0.18	0.59	0.08	0.33	4.06
$1x10^{-3}$	6.30	4.42	0.18	0.58	0.10	0.32	4.22
$5x10^{-3}$	6.49	3.88	0.23	0.65	0.06	0.29	4.52
0.01	6.68	4.27	0.25	0.63	0.09	0.28	4.66
0.02	6.83	3.97	0.26	0.65	0.06	0.29	4.75
0.03	6.93	3.21	0.28	0.67	0.05	0.28	4.88
0.04	7.10	4.45	0.31	0.64	0.08	0.28	4.99
0.05	7.09	3.57	0.32	0.66	0.06	0.28	4.95

[rCMP] /M	τ_1 /ns	τ_2 /ns	τ_3 /ns	A_1	A_2	A_3	$<\tau>$/ns
0	6.17	2.49	0.17	0.49	0.09	0.42	3.32
$1x10^{-5}$	6.23	3.27	0.16	0.50	0.08	0.42	3.44
$5x10^{-5}$	6.20	2.95	0.18	0.50	0.08	0.42	3.41
$1x10^{-4}$	6.18	2.82	0.17	0.51	0.08	0.41	3.45
$5x10^{-4}$	6.09	2.25	0.16	0.53	0.06	0.41	3.43
$1x10^{-3}$	6.17	2.95	0.20	0.56	0.09	0.35	3.79
$5x10^{-3}$	6.08	3.52	0.20	0.51	0.11	0.38	3.56
0.01	5.91	3.56	0.21	0.48	0.12	0.40	3.35
0.02	5.75	3.54	0.25	0.38	0.19	0.43	2.97
0.03	5.57	3.50	0.24	0.31	0.22	0.47	2.61
0.04	5.45	3.56	0.27	0.25	0.26	0.49	2.42
0.05	5.03	3.19	0.25	0.28	0.20	0.52	2.18

[rGMP] /M	τ_1 /ns	τ_2 /ns	τ_3 /ns	A_1	A_2	A_3	$<\tau>$/ns
0	6.45	4.58	0.21	0.51	0.21	0.28	4.31
$1x10^{-5}$	6.46	4.94	0.20	0.46	0.24	0.30	4.22
$5x10^{-5}$	6.32	4.24	0.18	0.55	0.13	0.32	3.98
$1x10^{-4}$	6.59	4.93	0.21	0.41	0.29	0.30	4.19
$5x10^{-4}$	6.52	4.60	0.22	0.49	0.22	0.29	4.27
$1x10^{-3}$	6.43	4.41	0.20	0.51	0.15	0.34	4.01
$5x10^{-3}$	6.69	4.13	0.24	0.54	0.13	0.33	4.23
0.01	6.85	4.56	0.27	0.60	0.11	0.29	4.69
0.02	7.08	4.25	0.31	0.64	0.09	0.27	5.00
0.03	7.17	3.44	0.32	0.66	0.07	0.27	5.03
0.04	7.35	4.48	0.35	0.63	0.09	0.28	5.13
0.05	7.43	4.36	0.36	0.63	0.09	0.28	5.17

[dTMP] /M	τ_1 /ns	τ_2 /ns	τ_3 /ns	A_1	A_2	A_3	$<\tau>$/ns
0	6.14	2.68	0.15	0.49	0.06	0.45	3.24
$1x10^{-5}$	6.09	2.15	0.15	0.52	0.05	0.43	3.34
$5x10^{-5}$	6.18	3.61	0.16	0.52	0.08	0.40	3.57
$1x10^{-4}$	6.17	3.40	0.14	0.50	0.06	0.44	3.35
$5x10^{-4}$	6.08	2.93	0.14	0.54	0.04	0.42	3.46
$1x10^{-3}$	6.13	3.79	0.15	0.51	0.08	0.41	3.49
$5x10^{-3}$	5.91	3.65	0.14	0.48	0.08	0.44	3.19
0.01	5.46	0.76	0.11	0.48	0.04	0.48	2.70
0.02	5.02	1.26	0.09	0.36	0.04	0.60	1.91
0.03	4.68	2.04	0.10	0.32	0.04	0.64	1.64
0.04	4.26	0.52	0.07	0.24	0.06	0.70	1.10
0.05	3.98	0.44	0.06	0.20	0.06	0.74	0.87